TNO Built Environment and Geosciences

Nederlandse Organisatie voor
toegepast-natuurwetenschappelijk
onderzoek / Netherlands Organisation
for Applied Scientific Research

The Netherlands

www.tno.nl

T
F

TNO report

2008-U-R1071/B

Bergermeer Seismicity Study

Date	6 November 2008
Author(s)	Mevr. Dr. A.G. Muntendam-Bos Mevr. Drs. B.B.T. Wassing Drs. C.R. Geel Ir. M. Louh Mevr. Dr. K. van Thienen-Visser
Copy no.	
No. of copies	55
Number of pages	95
Number of appendices	1
Customer	TAQA Energy BV
Projectname	TAQA Bergermeer Seismicity
Projectnumber	034.82130

Contents

List of Figures **4**

List of Tables **7**

Summary **9**

Samenvatting **11**

1 Introduction **13**

2 Background **14**
2.1 General 14
2.2 Seismic Hazard 16
2.2.1 Magnitude versus fault area and slip displacement 16
2.2.2 Temperature change and pore pressure change 20

3 Geological Model **22**
3.1 Introduction 22
3.2 Geology of the BGM field 22
3.2.1 Sedimentary geology 22
3.2.2 Structural Geology 22
3.3 Preparation of the static model for Geomechanics 24
3.4 Determination of formation thicknesses for subsidence modelling 27

4 Subsidence Modelling **31**
4.1 Subsidence Data 31
4.1.1 Levelling data Bergen concession 31
4.1.2 Levelling data Bergermeer 32
4.1.3 Levelling data precision 33
4.2 Subsidence prediction from reservoir compaction 35
4.3 Elasticity parameters 36
4.3.1 Derivation of elasticity parameters 36
4.3.2 Sensitivity of subsidence to subsurface elasticity parameters 36
4.4 Subsidence inversion 37
4.4.1 Procedure 39
4.4.2 Results 40

5 Reservoir Engineering **41**
5.1 Dynamic reservoir model 41
5.1.1 Basic model data and Gas Initially in Place 41
5.1.2 Thermodynamical data 42
5.1.3 Matching the compositional/thermal model to the blackoil BaseModel 43
5.2 Underground Gas Storage 43
5.2.1 Well injection bottom hole temperature (BHT) 44
5.2.2 Cushion gas injection phase 44
5.2.3 Injection/production cycle 45
5.3 Results 46
5.4 Sensitivity analysis 46
5.5 Data transfer to the geomechanical study 49

5.6 Conclusions and recommendations 49
5.6.1 Conclusions 49
5.6.2 Recommendations 49

6 Geomechanical analysis 50
6.1 Introduction 50
6.2 Methodology 50
6.3 Stress and deformation modelling of reservoir depletion and injection/production 51
6.3.1 Background 51
6.3.2 Basic analysis thermo-poro-elasticity and frictional fault theory 52
6.3.3 Direct injection into faultzones 57
6.4 Finite Element Model 57
6.4.1 Material models and geomechanical parameters 58
6.4.2 Calculation scenarios 62
6.4.3 Boundary and initial conditions 62
6.4.4 Modelling reservoir depletion and injection/production 63
6.5 Modelling results 63
6.5.1 Initial stresses 63
6.5.2 Calibration stress-path BGM#8. 66
6.5.3 Stress paths for faults 68
6.6 Conclusions and recommendations of geomechanical analysis 80
6.6.1 Conclusions 81
6.6.2 Recommendations 82

7 Seismic hazard analysis 83

8 Conclusions & Recommendations 86
8.1 Conclusions 86
8.2 Recommendations 87

9 References 88

10 Signature 90

List of Figures

Figure 2.1: The relation between the fault surface area and the seismic moment 18
Figure 2.2: Definition of the fault length, width and depth range (of the fault in the reservoir) used in table 2-2 (left) and a schematic representation of the faults in the Bergermeer field (right)..... 18
Figure 2.3: The relation between the magnitude of a seismic event and the slip displacement for the southwestern (0.96 km^2), internal (1.06 km^2) and northeastern (1.37 km^2) fault of the Bergermeer field. 19
Figure 2.4: The relation between the maximum slip displacement and a change in temperature or a change in pore pressure. 21
Figure 3.1: Well log panel through wells 1,2,5,8A showing reduced porosities near the top and base of the Slochteren Sst. 23
Figure 3.2: 3D view of the Bergermeer Field showing Top Slochteren surface, faults from Horizon's model, and BGM wells. 23
Figure 3.3: Petrel log calculator script to determine Zechstein lithologies. 24
Figure 3.4: Results of the calculated lithologies for the Zechstein. Gross lithologies were grouped into informal units (e.g. the 'Mid-Ze Halite') and correlated. 25
Figure 3.5: Parameters used in the zone building process of the separate Zechstein Petrel model. 25
Figure 3.6: Cross-section through BGM field, composed of Horizon's Petrel model of the Slochteren Sst, a separate Petrel model for the Zechstein, and TAQA's overburden surfaces and faults. 26
Figure 3.7: Isochore map of the Tertiary ……28
Figure 3.8: Isochore map of Holland + Vlieland Formations ……28
Figure 3.9: Isochore map of Keuper + Bunter Formations ……29
Figure 3.10: Isochore map of Main Claystone Formation ……29
Figure 3.11: Isochore map of the Zechstein ……...30
Figure 3.12: Isochore map of the Slochteren Sst ……...30
Figure 4.1: All levelling data locations of the Amoco campaigns of the Bergen Concession (1980, 1981, 1984, 1988, 1992, 1997, 2001, and 2006). 32
Figure 4.2: Total subsidence observed between points measured both in 1972 and 2006. The maximum subsidence estimates at ~10.5 cm and is roughly located northwest of the Bergermeer field. 34
Figure 4.3: Subsidence bowl computed for the Bergermeer-Groet reservoir model based on a compaction coefficient of 3.5 10-5 bar-1 and elasticity profiles using the least values for the parameters (left), the minimum values (middle), and the highest values in the ranges for the elasticity parameters (right). Clearly the implementation of weaker overburden layers (the lowest values) induces a smaller but deeper subsidence bowl, whereas stronger overburden layers (the highest values) induce a wider shallower subsidence bowl compared to the subsidence bowl compute for the mean values of the elasticity parameters (middle figure). ... 38
Figure 5.1: Temperature at some well locations of the Bergermeer field. 42
Figure 5.2: Bottom hole temperature as function of injection rate. 44
Figure 5.3: Temperature distribution at 24th of October for layer 13. Although this is just after the fisrt cushion gas injection period, the lowest temperatures are reached at this date as 1) injection gas temperature is lowest at 20-30°C, as compared to

60-66°C in later phases, and 2) injection rates per well are high as only 6 wells are injecting, while in later phases up to 17 wells are injecting. 47
Figure 5.4: Cross section of the single well model with grid block sizes equal to the full model: length=width=100 m and height=10 m. 48
Figure 5.5: Cross section of the single well model with a small grid block size: length=width=10m and height=10 m. 48
Figure 6.1: Initial state of stress in the subsurface and on the fault plane, resolved by the Mohr circles. 54
Figure 6.2: Stresses in the subsurface and tractions on the fault plane. 54
Figure 6.3: Left: Critical development of the stress path for depletion. Right: Non-critical development of the stress path for injection in a depleted reservoir. 55
Figure 6.4: Stress changes in the reservoir during depletion and *isothermal* injection (friction angle of fault 33°). 56
Figure 6.5: Direct injection into a fault zone: Effect of pore pressure increase on stress state and fault stability. 57
Figure 6.6 Geology and location of cross-section for DIANA model. 59
Figure 6.7: DIANA mesh. Faults are indicated in red and numbered for reference. 60
Figure 6.8: Temperature and pore pressure against time (for element close to injection well). Top figure: complete period of reservoir depletion, cushion gas injection and one cycle of working gas injection and production. Bottom: detailed profile for injection of cushion gas and working gas and production of working gas. 64
Figure 6.9: In-situ vertical effective stresses [MPa] in and around the reservoir – *reference* scenario 1. 65
Figure 6.10: In-situ horizontal effective stresses [MPa] in and around the reservoir – *reference* scenario 1. 65
Figure 6.11: Effective stress ratio K'_0 [-] in and around the reservoir – *reference* scenario 1. 66
Figure 6.12: Effective stress ratio K'_0 [-] in and around the reservoir –scenario 5. 66
Figure 6.13: Location of element 1980 used for comparison of stress data with minifrac test in BGM#8. Faults are presented in red, reservoir rocks in pink. 67
Figure 6.14: Stress-paths during depletion. Stresses at the start and end of depletion are plotted. In the top figure the stress paths for the reference scenario and scenario's 2, 3, 4, 6 and 7 are plotted (no creep). The bottom figure gives the stress path for scenario 5 (creep Zechstein). 69
Figure 6.15: Location of maximum fault slip during depletion on central fault intersecting the reservoir. Stress path of element 160 is presented in figure. Reservoir rocks are indicated in pink colours. 70
Figure 6.16: Stress path on fault4, in fault element 160 halfway the overlap of reservoir rocks. Reference scenario 1. 70
Figure 6.17: Location of maximum fault slip during injection, on central fault intersecting the reservoir. Stress path of element 164 is presented in figure. Reservoir rocks are indicated in pink colours. 71
Figure 6.18: Stress path during injection and production in fault element 164 below the overlap of reservoir rock. Reference scenario 1. 71
Figure 6.19: Relative shear displacement on fault4, reference scenario 1. Distance indicated on vertical axis is measured from the top of the fault. Upper right figure gives location of elements. Reservoir rocks presented in pink colours. 72

Figure 6.20: Relative shear displacement on fault 4 between a) end depletion and end injection and b) end injection and end production. Reference scenario 1. Distance indicated on vertical axis is measured from the top of the fault. 72
Figure 6.21: Relative shear displacement on fault3, reference scenario 1. Upper right figure gives location of elements. Reservoir rocks presented in pink colours..... 73
Figure 6.22: Relative shear displacement on fault 5, reference scenario 1. Upper right figure gives location of elements. Reservoir rocks presented in pink colours..... 73
Figure 6.23: Location of element 5096 on overburden fault 8. Stress path for element is shown in Figure 6.24. 74
Figure 6.24: Stress path on overburden fault 8. Reference scenario 1..... 75
Figure 6.25: Minimum temperatures around injection well during injection (reference scenario 1). 76
Figure 6.26: Maximum thermal strains around injection well during injection (reference scenario 1). 77
Figure 6.27: Applied temperature load (top) and the induced change in the vertical effective stress (middle) and horizontal effective stress (bottom) around injection well predicted by DIANA simulations. Position of injection well is at 500m. Note that the effect of the temperature decrease on horizontal and vertical effective stresses at a distance of more than 150m from the well is very small compared to the effect of the pressure increase due to injection 79
Figure 6.28: Stresses at the end of depletion (red), during insothermal injection up to a pore pressure of 4.6MPa, (green), during nonisothermal injection up to 4.6MPa at a distance of 150m (yellow) and 100m (red) from the injection well. 80
Figure 6.29: Schematic overview of the recommended distances within which the operator should refrain from planning injection wells. Distances depend on whether cold or warm gas is injected. 81

List of Tables

Table 2-1: Overview of occurrence of seismic events and the start of the injection/production cycle for the Alkmaar, Grijpskerk en Norg gas fields. 16
Table 2-2: Fault dimensions of the faults in the Bergermeer field. The fault width is calculated using the fault depth range and the fault dip. 18
Table 2-3: Magnitudes obtained with the slip displacement values by Logan (1997) 19
Table 2-4: Maximum slip lengths and maximum seismic magnitudes for the southwestern, internal and northeastern faults of the Bergermeer field. 20
Table 2-5: Maximum slip lengths and maximum seismic magnitudes for the southwestern, internal and northeastern faults of the Bergermeer field using the more realistic Young's modulus of 18 Gpa. 20
Table 3-1: Minimum, maximum, and average thicknesses for BGM reservoir and overburden. 27
Table 4-1: Correction factors of new NAP reference level with respect to old NAP reference level (correction factor = NNAP – ONAP) 33
Table 4-2: Stochastic error (in mm) for each campaign as utilized in this study. 35
Table 4-3: Total error (in m) for the benchmarks contained in each campaign. 35
Table 4-4: Ranges for the elasticity parameters for the different geological units. 37
Table 4-5: Values obtained for the χ^2, rms error, inferred c_m and $\sigma(c_m)$. 40
Table 5-1: Main reservoir model data. 41
Table 5-2: Gas Initially In Place 42
Table 5-3: Initial temperatures and rock thermal properties. 43
Table 5-4: Composition of initial reservoir gas and injected gas (% mole fraction). 43
Table 5-5: Gas storage and production specifications. 44
Table 5-6: Injection rate schedule for cushion gas injection. 45
Table 5-7: Injection well schedule for cushion gas injection. 45
Table 5-8: Well schedule for injection/production cycle for 2013. 46
Table 5-9: Injection/production cycle schedule for 2013. 46
Table 6-1: Stress values and pore pressures before and after depletion 56
Table 6-2: Defined geomechanical units. 59
Table 6-3: Geomechanical parameters for the geomechanical units. 60
Table 6-4: Calculation scenarios 62
Table 6-5: Maximum relative shear displacement at end depletion (cm) 75
Table 6-6: Maximum relative shear displacement (cm) between end depletion and end injection 75
Table 6-7: Maximum relative shear displacement (cm) between end injection and end production (for first production cycle) 76
Table 6-8: Input parameters for axial symmetric model. 78
Table 6-9: Subsidence and uplift predictions during depletion, injection of cushion gas (CG) and working gas (WG) and production of working gas 78
Table 7-1: Slip displacement (in cm) due to the earthquakes in 1994 and 2001 and total slip displacement (in cm) due to earthquakes compared to the slip displacement modelled with DIANA at 1994, 2001 and 2006 for the different DIANA scenarios. 83
Table 7-2: Slip displacement (in cm) due to the earthquakes in 1994 and 2001 and total slip displacement (in cm) due to earthquakes compared to the slip displacement

modelled with DIANA at 1994, 2001 and 2006 for the overburden faults of scenario 5..... 84
Table 7-3: Mean displacement (δ_{mean}) and maximum displacement (δ_{max}) over the fault width for the 7 scenarios from DIANA and their maximum seismic magnitude for the internal fault in the reservoir..... 84
Table 7-4: Mean displacement (δmean) and maximum displacement (δmax) over the fault width for the overburden faults of scenario 5 from the DIANA modelling and their maximum seismic magnitude..... 85

Summary

The Bergermeer Gas field has a history of induced seismicity during the production of hydrocarbons. In both 1994 and 2001, 2 subsequent seismic events were registered by the KNMI of which the hypocenters were located in the field. Considering tectonic earthquakes, this part of the Netherlands is considered to be a low seismicity area. Thus, the registered events are most likely induced by the pressure changes due to gas production.

In the near future TAQA Energy B.V. wants to utilize the Bergermeer field as a Underground Gas Storage (UGS) facility. Consequently, concerns were raised regarding the risk of induced seismicity originating from the proposed re-pressurization of the Bergermeer field and its operation as an UGS facility. TAQA has contracted TNO Built Environment and Geosciences to independently investigate the seismic hazard associated with underground gas storage.

Seismicity induced by hydrocarbon production originates from two often interacting mechanisms which result in fault reactivation: differential compaction[1] and pore pressure changes. Faults can generally be considered as weak planes or weak zones in the reservoir rocks, and deformations caused by the extraction (or injection) of gas in the reservoir will be largely accommodated on fault planes or within fault zones. Based on the geometry of the fault and the rigidity of the weak zone (fault) to shear (shear modulus), the maximum magnitude feasible for a seismic event on the faults bounding, intersecting, as well as in the vicinity of the Bergemeer field have been derived. Assuming an absolute upper bound of the shear modulus, a maximum magnitude of 3.9 is derived for the central fault of the Bergermeer field. All other faults obtain lower maximum magnitudes due to the limited dimensions of the faults. Therefore, earthquakes with magnitudes exceeding 3.9 are improbable.

The geomechanical behaviour of the reservoir to gas injection and production depends significantly on the pressure and temperature changes. Especially the lateral extension of the temperature response of the reservoir to cold gas injection is crucial for the seismic behaviour of the reservoir during the operation of the UGS facility. Based on operational data provided by TAQA (well schemes, injection/production schedules, history matched reservoir model, etc) the dynamic response of the reservoir was modelled and used as input for the geomechanical analysis. It is shown that the temperature distribution in the field after injection of cold cushion and working gas and one production phase[2] shows a temperature decline localized around the wells. The temperature of the rest of the field remains largely unaffected. The temperature decrease is most evident in the first two years of gas injection. After this period gas needs to be compressed[3], this increases the injection temperature. Subsequent gas production results in warm gas flowing to areas cooled down by the gas injection, heating them again.

[1] The compaction of rocks induces an upward motion of the lower boundary of the reservoir and a downward motion of the upper boundary. In the presence of pressure differences across the fault, the rocks in the reservoir subjected to the largest pressure drop compacts more than the rocks in the reservoir subjected to the lower pressure drop. Hence the motions across the fault of the reservoir boundaries are different, which may lead to slip on the fault.

[2] Working gas is injected in the summer months when demand for gas is relatively low. Subsequently, this working gas is produced in the winter months when the demand for gas is relatively high.

[3] The gas pressed together and at high pressures injected into the reservoir.

In the geomechanical analysis, seven scenarios are defined for modelling, in which Poisson's ratio, stiffness ratio[4] between top seal and reservoir rock, fault shear strength and material behaviour of the Zechstein (rocksalts) are varied. The analysis shows that the injection of gas in the Bergermeer reservoir stabilizes the faults intersecting and bounding the reservoir. The fault movements observed locally on the central fault are an order of magnitude lower than observed during depletion. The localized temperature decline around the injection wells does not affect the stability of the known faults, as long as injection wells are located at a minimum distance of 200m from the faults (uncertainty of the location of the fault due to the limited resolution of the seismics taken into account)[5]. The largest slips observed during injection correspond to seismic magnitudes ranging between 2.4 and 2.7.

The largest subsidence measured since the start of depletion and 2006 above the Groet, Bergen and Bergermeer fields is 10,5 cm. Predicted subsidence values during depletion are overestimated when compared to actual values by 15-25%. Taking into account a correction factor of 15-25%, the predicted uplift during injection is 4.9-6.0 cm. The predicted subsidence during production is 1.6-2.0 cm

[4] One type of rock is more flexibel than an other. This is comparable to the difference between a shelf and a piece of paper: the paper is much more flexible than the shelf.
[5] In case the injected gas is heated a distance of 150 m from the fault should be observed in order to avoid direct injection into the fault zone.

Samenvatting

In het verleden zijn er tijdens de winning van gas uit het Bergermeerveld vier aardbevingen opgetreden. Zowel in 1994 als in 2001 heeft het KNMI twee opeenvolgende aardbevingen geregistreerd. Uit deze registraties blijkt dat de hypocentra van de aardbevingen binnen het gasveld geplaatst kunnen worden. Over het algemeen wordt dit deel van Nederland beschouwd als een gebied met een laag seismisch risico; het gebied kende geen natuurlijke aardbevingen voorafgaand aan de gaswinning. De opgetreden aardbevingen zijn zeer waarschijnlijk het gevolg van drukveranderingen in de ondergrond veroorzaakt door de gaswinning.

TAQA Energy BV wil het Bergermeer gasveld in de toekomst gebruiken voor de ondergrondse opslag van gas. De vraag rijst dan ook of, en hoe, de drukveranderingen in de ondergrond ten gevolge van de ondergrondse gasopslag het risico op aardbevingen beïnvloeden. TAQA Energy BV heeft TNO Bouw en Ondergrond opdracht verleend om onafhankelijk onderzoek te verrichten naar het aardbevingsrisico bij ondergrondse gasopslag.

Aardbevingen tijdens de winning van olie en gas worden veroorzaakt door twee vaak gelijktijdig optredende mechanismen: differentiële compactie van het reservoirgesteente[6] en veranderingen in de poriëndruk in het reservoirgesteente. Beide mechanismen kunnen leiden tot de reactivatie van breuken in en nabij het reservoir. De bestaande breuken in de ondergrond vormen zwaktezones, en de deformaties in de ondergrond veroorzaakt door de gasproductie en injectie zullen zich grotendeels lokaliseren in de breukzones. Op basis van de gegevens over de geometrie en de weerstand van de breuken tegen schuifdeformatie[7], kunnen we de maximaal mogelijke magnitude afleiden voor de breuken in en om het gasreservoir. Uitgaande van een maximale waarde voor de schuifweerstand berekenen we een maximale magnitude van 3.9 voor de centrale breuk in het Bergermeer gasveld. De afmetingen van de andere breuken zijn kleiner; voor deze breuken worden lagere magnitudes afgeleid. Aardbevingen met magnitudes groter dan M=3.9 zijn dus onwaarschijnlijk. Tijdens de gasonttrekking van het veld zijn trillingen met een maximale magnitude van 3.5 opgetreden.

Het geomechanisch gedrag van het reservoirgesteente hangt af van de druk- en temperatuurveranderingen in het reservoir bij de injectie en productie van gas. Met name de laterale verbreiding van de temperatuurveranderingen bij de injectie van koud gas is van belang voor het seismisch gedrag van het reservoir bij ondergrondse gasopslag. Op basis van operationele gegevens van TAQA Energy BV (zoals de configuratie van de boorputten, injectie- en productieschema's, een gekalibreerd reservoir model, etc.) is de dynamische respons van het reservoir gemodelleerd. De resultaten zijn gebruikt als input voor de geomechanische analyse. Aangetoond wordt

[6] Het compacteren van gesteenten in de ondergrond veroorzaakt een opwaartse beweging van de ondergrens van het gesteente en een neerwaartse beweging van de bovenkant van het gesteente. Door optredende drukverschillen aan weerszijden van de breuk wordt het gesteente met de grootste drukdaling compacter dan het gesteente met de lagere drukdaling. De bewegingen aan weerzijden van de breuk zijn daardoor verschillend wat kan leiden tot verschuivingen langs de breuk.

[7] Het laten plaatsvinden van verschuivingen over de breuk. Net als bij het verschuiven van een tafel, moet een bepaalde weerstand van de twee materialen tegen een verschuiving worden overwonnen voordat er beweging optreedt.

dat de temperatuurverlaging in het veld na de injectie van het gas en één productiecyclus[8] beperkt blijft tot het gebied direct rondom de putten. De temperatuur van de rest van het veld wordt nauwelijks beïnvloed. De temperatuurdaling is het grootst tijdens de eerste twee jaar van gasinjectie. Na deze periode wordt het gas gecomprimeerd[9] en neemt de injectietemperatuur van het gas toe. Tijdens de opeenvolgende productie van gas wordt warm gas aangetrokken naar eerder afgekoelde delen van het reservoir en vindt in de gebieden rond de putten opwarming plaats.

In de geomechanische analyse zijn zeven scenarios doorgerekend, waarin de belangrijkste geomechanische eigenschappen (Poisson's ratio van het reservoirgesteente, stijfheidscontrast[10] tussen het reservoirgesteente en de top seal, sterkte van de breuken en kruipgedrag van het zout) worden gevarieerd. Uit de berekeningen blijkt dat de breuken in en grenzend aan het reservoir grotendeels stabiliseren tijdens de injectie van het gas. Dit betekent dat spanningen over de breuk die zijn veroorzaakt door de winning van het gas weer worden opgeheven en de kans op verschuivingen langs de breuken afneemt. Lokaal kunnen tijdens de injectie van het gas wel breukbewegingen optreden, maar deze bewegingen zijn bijna 20 keer kleiner dan de bewegingen tijdens winning van het gas. De lokale temperatuurdaling rondom de putten beïnvloedt de stabiliteit van de breuken niet, zo lang de injectieputten op een minimum afstand van 200 m van de breuken worden geplaatst (hierbij is rekening gehouden met de onzekerheid in de exacte positie van de breuken ten gevolge van de beperkte resolutie van de seismische gegevens)[11]. De grootste breukbeweging tijdens injectie, die in de modellen berekend wordt, komt overeen met een seismische magnitude van 2.4 tot 2.7.

De maximaal gemeten bodemdaling in de periode van het begin van gasonttrekking tot 2006 boven de gasvelden Groet, Bergen en Bergermeer is ongeveer 10,5 cm. De bodemdaling die door de geomechanische modellen voor de gasonttrekking wordt gemodelleerd is 15-25% groter. Rekening houdende met deze correctiefactor van 15-25% voorspellen de modellen een stijging van de bodem met 4,9-6 cm gedurende de injectie. De voorspelde, gecorrigeerde daling tijdens de productie is 1,6-2,0 cm.

[8] Injectie van een hoeveelheid gas die kan worden opgeslagen in de zomer en vervolgens de productie van dit gas in de winter om zo aan de grotere vraag 's winters te voldoen.
[9] Het gas wordt samengeperst en onder grotere druk in het reservoir gepompt.
[10] Het ene gesteente is buigzamer dan een ander gesteente. Dit is te vergelijken met het verschil tussen een plank en een blad papier: een blad papier is minder stijf en dus makkelijker te buigen dan een plank.
[11] Indien het te injecteren gas verwarmt wordt, moet een afstand van 150 m tot de breuk in acht genomen worden om directe injectie in de breukzone te voorkomen.

1 Introduction

This report represents the deliverable prepared according to the terms and conditions agreed between TAQA Energy BV, Den Haag, The Netherlands (the company) and TNO B&O, Utrecht, The Netherlands (the contractor) in the contract ref. 94257/sg (C-10-92), 21.02.2008.

The Bergermeer seismicity study has been carried out by TNO B&O, Business Unit Geo-Energy & Geo-Information, with the objective to provide the required insight in the seismic risks of re-pressurization of the Bergermeer field. This requires a thorough analysis of the geomechanical behaviour of the field, in particular the processes related to pressure variations leading to seismic activity. At a later stage (23.04.2008), the scope was extended with scrutinizing the geomechanical consequences of thermal variations in the reservoir due to cold gas injection on the processes leading to seismic activity.

This report describes the general background of the Bergermeer field and the processes inducing seismicity. This is followed by a description of the geological model of the Bergermeer field, the subsidence modelling, reservoir engineering and geomechanical analysis. The report concludes with the general conclusions and recommendations.

2 Background

2.1 General

Underground gas storage is now widely used as a source of additional capacity during the seasonal peak demand for gas. Storage reservoirs are injected with gas during the low demand summer months and gas is produced during the winter months. Since induced seismicity due to the production of a gas field may occur, the seismic risk associated with seasonal periods of gas re-injection and production of the same gas field has to be addressed. The present study addresses this issue for the TAQA Bergermeer field located in the north-western part of the Netherlands.

The probability that a gas field will display induced seismicity during the depletion phase depends on the pressure drop, fault density and stiffness ratio between the top seal and the reservoir rock (Van Eijs et. al., 2006). Induced seismicity will occur if these parameters exceed a critical value. Furthermore, Grasso and Sornette (1998) reviewed reported cases of induced seismicity and found evidence that both pore pressure changes and mass transfer corresponding to incremental differential stress in the order of 1MPa[12], trigger seismic instabilities in the uppermost crust even in otherwise historically aseismic areas. They propose that the crust is in a self-organized critical state; a significant fraction of the crust is not far from instability and can thus be made unstable by minute perturbations. However, not all perturbations will trigger seismic activity depending on the sign of the perturbation and the direction and the mobilized shear capacity on the fault. Once triggered, stress variations of at least one order of magnitude smaller than the trigger step (around 0.1MPa) are enough to sustain the seismic activity over long periods of time. Therefore a gas reservoir with a history of induced seismicity has a higher probability of new induced events even with small stress variations.

There are two main mechanisms which cause stress changes during the depletion phase; differential compaction and pore pressure changes. Both mechanisms may cause seismicity through fault reactivation. The decrease in pore pressure during depletion leads to stress changes and compaction of the reservoir, which is visible at the surface as subsidence. Due to the arching effect the overburden load above the compacting reservoir is re-distributed to the abutting rock next to the edges of the reservoir. This additional stress may cause rock failure and minor faulting at the edge of the reservoir, as well as at faults separating reservoir compartments. In the reservoir, the horizontal and vertical effective stresses increase due to the reduction of the pore pressure, which in turn increases the chance of fault reactivation. Re-pressurization will stabilize the reservoir if differential compaction is the source of the seismicity since the formation above the reservoir will move upwards due to the increase in pore pressure.

Fault geometry plays an important role for fault reactivation. Roest and Mulders (2000) modelled likely fault geometries and tested which geometries increase the chance of fault reactivation. They found that normal faults with an angle of 20% to 30% with respect to the vertical direction (dip of 60°-70°) are most sensitive to fault reactivation especially if the direction of movement during depletion is similar to the natural

[12] 1 MPa= 10 bar = 9,9 atm

direction of movement on the fault. A limitation of this mechanism is that the horizontal stresses in the reservoir should be low since large horizontal stresses will inhibit fault movement. In the Bergermeer field, the north-eastern bounding normal fault has a strike of 143° and a dip of 68°, the internal normal fault has a strike of 160° and a dip of 53° to 63° and the south-western bounding normal fault has a strike of 160° and a dip of 53° to 62°. The south-western bounding and the internal fault are therefore normal faults with dips at the edge of the critical range. However, the north-eastern bounding fault falls well within the critical range. The modelling of Roest and Mulders (2000) also confirmed the likely occurrence of rock failure and minor faulting at the edge of the reservoir caused by differential compaction.

In the Bergermeer field, four seismic events have taken place; two in 1994 (KNMI, 1994 [1&2]) and two in 2001 (Haak et al., 2001). The focal mechanisms of all four events showed reverse faulting, which is contrary to the natural movement of the bounding and internal faults of the Bergermeer field. The first event in 1994 was, at first, positioned on the north-eastern normal fault at 2.2 km ± 0.5 km in depth. The large distance of the seismic stations which recorded the event introduced large uncertainties in the epicentre determination. Therefore the KNMI (1994 [1]) used a macroseismic epicentre determination which uses reported damage and intensities to locate the epicentre. The second event in 1994 (KNMI, 1994 [2]) was very similar to the first, but the macroseismic epicentre was located more towards the internal normal fault in the Bergermeer field at 2.5 km ± 0.5 km in depth. Since the location of the second fault and the focal mechanism corresponded more to the internal fault, the first event was relocated on this fault as well. The two events in 2001 were also located on the internal normal fault at 2.0 km ± 0.2 km in depth, similar to the events of 1994. One reason for this was that the focal mechanisms showed reverse faulting with a strike of 130° and a dip of 66° which was thought to correspond more to the internal fault.

The accuracy of the location of the epicentre is vitally important to determine whether the seismicity was caused by fault reactivation due to stress changes in the reservoir, The depth of the epicentre can only be obtained accurately if the seismicity is recorded in the direct neighbourhood of the seismic event, preferably above the event. The lateral accuracy depends on the number of (close) seismic stations and the azimuthal coverage of these stations. For the events in the Bergermeer field, the depth was more accurately obtained in 2001 due to the presence of three, relatively close (3 km, 7 km and 8 km), borehole seismometers placed after the two events of 1994. However, for such shallow events, a truly accurate depth determination needs a seismic station directly above the events. The azimuthal coverage of seismic stations that recorded the events is lacking towards the north due to the gap in the seismic stations and lacking in the west due to the limited number of seismic stations in the U.K (at most seven) and the larger distance (larger than 400 km) to the seismic events. For the 1994 seismic events, the uncertainty of the macroseismic hypocenter determination was 0.5 km in lateral direction and 0.5 km in depth, while the uncertainty in the hypocenter for the instrumental determination was, at best, 1 km in lateral direction and 2 km at depth. A relative epicentre determination was used on the second event of 1994, which placed the event at 500m ± 100m in the north-north-westerly direction from the first event of 1994 and on the second event in 2001, which placed the relative epicentre at a distance of 205m ± 50m from the first event in the north-north-westerly direction. Hence the uncertainty in epicentre location can not unambiguously place the events on the internal fault. It remains feasible that the events occurred on one of the bounding faults or even on one of the many listric overburden faults.

Table 2-1: Overview of occurrence of seismic events and the start of the injection/production cycle for the Alkmaar, Grijpskerk en Norg gas fields.

	start injection-production cycle	Seismic Events			
		date	M	date	M
Alkmaar	1996				
Grijpskerk	1996	2-3-1997	1.3		
Norg	1997	2-9-1996	2.1	7-6-1999	1.1

Analogue gas fields that have been depleted and re-injected with natural gas in the Netherlands are Alkmaar (Winningsrapport Alkmaar, 2003), Norg (Winningsrapport Norg, 2003), and Grijpskerk (Winningsrapport Grijpskerk, 2003). Of these gas fields, Alkmaar has never experienced induced seismicity in the sixteen years of depletion or in the period of re-pressurization nor in the subsequent periods of depletion and injection since 1996. Both Grijpskerk and Norg have experienced a small amount of seismicity (see also Table 2-1). The Norg field is the most seismically active, with two registered events in the last ten years (one at September 2nd in 1996 with a magnitude of 2.1 and one at June 7th in 1999 with a magnitude of 1.1), whereas the Grijpskerk field has one registered event in the last six years (at March 2nd in 1997 with a magnitude of 1.3). The Norg gas field was depleted until 1995 and closed until mid 1997. From mid 1997, the field has been re-pressurized and used as a seasonal injection/depletion field. The Grijpskerk field was depleted from 1993 to 1994 and closed for conversion to underground gas storage until 1996. Since then, the Grijpskerk field has been re-pressurized and used for seasonal injection/depletion. Thus, both Grijpskerk and Norg have displayed seismic activity during the period of re-pressurization. The Norg field shows the largest fault density, a key parameter needed for induced seismicity (Van Eijs et al., 2006), with multiple normal faults which are according to Roest and Mulders (2000) the most likely candidates for fault reactivation. The Grijpskerk field has two bounding normal faults and several small internal faults while the Alkmaar field only has one normal bounding fault.

In the modelling of Roest and Mulders (2000) a gas reservoir which is depleted and re-injected on a regular basis did not have an effect on the seismicity. This is consistent with the lack of seismicity observed for the Norg and Grijpskerk fields since the injection/production cycle has been in operation. However, they cannot exclude seismicity due to large injection/depletion rates and large local pressure and temperature differences in the reservoir.

2.2 Seismic Hazard

2.2.1 Magnitude versus fault area and slip displacement

The magnitude (M) of a seismic event is related to the seismic moment through a relation given by Hanks and Kanamori (1979).

$$M = \frac{2}{3}\log(M_0) + 10.7333 \qquad (5)$$

The seismic moment depends on the shear modulus (μ), the average slip displacement on a fault (δ) and the fault area (A).

$$M_0 = \mu \delta A \qquad (6)$$

From these equations the relationship between the fault area and the magnitude of a seismic event can be obtained. This relationship is shown in Figure 2.1 for several slip displacement values mentioned by Logan (1997) and assuming a shear modulus of 18 GPa. This shear modulus corresponds to a Young's modulus of 40 Gpa (using a Poisson's ratio of 0.11) . Even though this Young's modulus is outside the typical range of Rotliegend sandstone (10 Gpa to 30 Gpa), we retain this value as it provides an upper bound of the maximum magnitude feasible for a seismic event. However we will also compute the maximum magnitude of a seismic event with a more realistic Young's modulus for the Rotliegend sandstone of 18 Gpa.

In Figure 2.1, the slip displacement of 8 mm was found by Haak (1994) for the 1994 seismic event in the Bergermeer field assuming a circular slip zone. To obtain an upper bound for the displacement slip on the internal normal fault, Logan (1997) estimated the slip as 10^{-4} times the slip length (e.g. Kanamori and Anderson, 1975), assuming that the slip length corresponds to the smaller source dimension (fault width). This was justified by theoretical solutions that indicate that the magnitude of the slip on a fault is controlled by the smaller of source dimensions (e.g. Scholz, 1990), except for large earthquakes that rupture through the entire lithosphere. The slip displacements of 18 mm was obtained using the fault width of the internal fault at the southern point (180 m; the smallest width, according to Logan (1997)) while the slip displacement of 38 mm was obtained using an average fault width of the internal fault of 380 m (Logan, 1997).

The dimensions of the southwestern bounding normal fault, the internal normal fault and the northeastern bounding normal fault as determined from the geological model (chapter 3) are shown in Table 2-2. Assuming that the entire fault in the reservoir has slipped, the maximum fault areas of these faults are 0.96 km^2, 1.06 km^2 and 1.37 km^2 for the southwestern, internal and northeastern faults, respectively.

Table 2-3 summarizes the seismic magnitudes obtained with Logan's values for the slip displacement and the fault areas as mentioned above. Logan (1997), however, does not take the fault dip into account in his determination of the fault width. The average fault width with the average dip taken into consideration is shown in Table 2-2. These values give a maximum slip displacement of 2.7 cm, 4.5 cm and 2.6 cm for the southwestern, internal and northeastern faults, respectively. The relation between the magnitudes of a seismic event and the slip displacement for the southwestern bounding normal fault (0.96 km^2), the internal normal fault (1.06 km^2) and the northeastern bounding normal fault (1.37 km^2) are shown in figure 2. According to Figure 2.3, the maximum slip displacements correspond to magnitudes of 3.7, 3.9 and 3.8, respectively (Table 2-4).

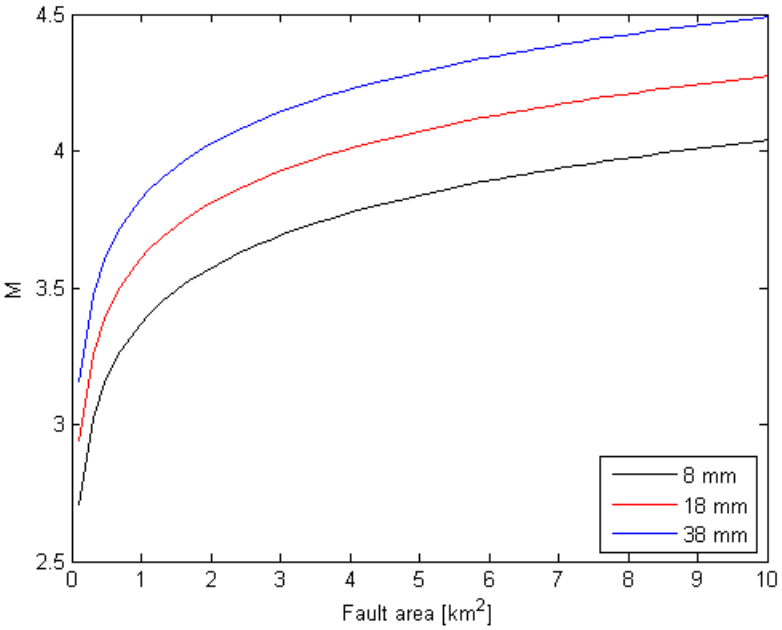

Figure 2.1: The relation between the fault surface area and the seismic moment

Table 2-2: Fault dimensions of the faults in the Bergermeer field. The fault width is calculated using the fault depth range and the fault dip.

	Fault length (km)	fault width (m)	fault depth range (m)	average dip (°)
Southwestern	3.5	274	230	57
Internal	2.5	448	380	58
Northeastern	5.3	258	240	68

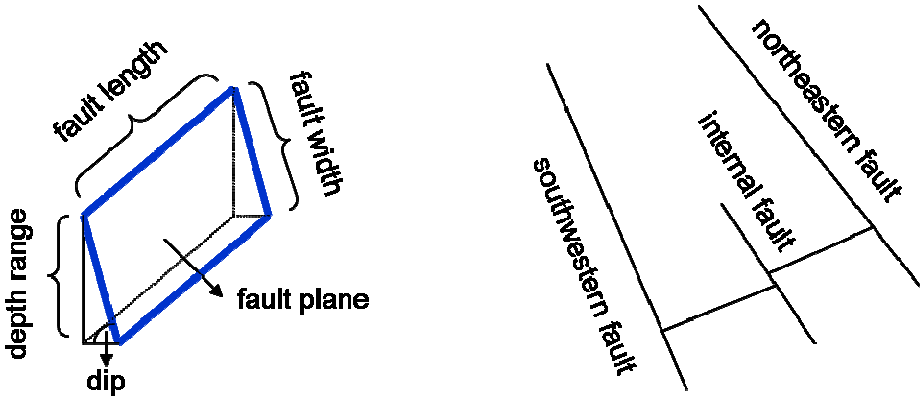

Figure 2.2: Definition of the fault length, width and depth range (of the fault in the reservoir) used in table 2-2 (left) and a schematic representation of the faults in the Bergermeer field (right)

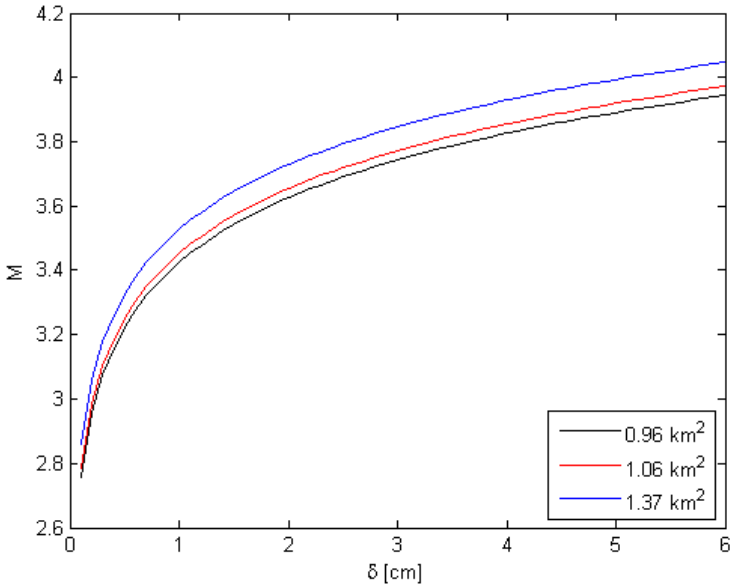

Figure 2.3: The relation between the magnitude of a seismic event and the slip displacement for the southwestern (0.96 km^2), internal (1.06 km^2) and northeastern (1.37 km^2) fault of the Bergermeer field.

Table 2-3: Magnitudes obtained with the slip displacement values by Logan (1997)

	fault area		
δ	0.96 km2	1.06 km2	1.37 km2
8 mm	3.4	3.4	3.5
18 mm	3.6	3.6	3.7
38 mm	3.8	3.8	3.9

The relationship between the local magnitude (M_L) and the seismic moment is given by (Hanks and Kanamori, 1979)

$$M_L = \frac{\log(M_0) - 9.1}{1.5}$$

For small shallow earthquakes in the north of the Netherlands with an average hypocenter depth of 2.3 km, a relation between the local magnitude and the intensity of the event is given by (De Crook et al, 1998)

$$I_0 = -0.51 + 1.70 M_L$$

For the seismic magnitudes given in table 2-4, the intensity is VI. Earthquakes with intensity VI are felt both inside as well as outside of the house. Small objects may fall and some glassware may break. Most buildings will have damage of category 1, some buildings will have damage of category 2. Category 1 gives negligible to slight damage (no structural damage) like hair-line cracks in a few walls, fall of small pieces of plaster and fall of loose stones from upper part of buildings. Category 2 gives moderate damage (slight structural damage) like cracks in walls and fall of fairly large pieces of plaster.

Table 2-4: Maximum slip lengths and maximum seismic magnitudes for the southwestern, internal and northeastern faults of the Bergermeer field.

	maximum slip length (cm)	maximum seismic magnitude	intensity
Southwestern	2.7	3.7	VI
Internal	4.5	3.9	VI
Northeastern	2.6	3.8	VI

Table 2-5: Maximum slip lengths and maximum seismic magnitudes for the southwestern, internal and northeastern faults of the Bergermeer field using the more realistic Young's modulus of 18 Gpa..

	maximum slip length (cm)	maximum seismic magnitude	intensity
Southwestern	2.7	3.5	V
Internal	4.5	3.7	VI
Northeastern	2.6	3.6	VI

Table 2-2 to Table 2-4 and Figure 2.1 and Figure 2.3 have assumed a shear modulus of 18 Gpa which is based on an unrealistic Young's modulus for the Rotliegend sandstone assumed by Logan (1997) of 40 Gpa. If we assume a more realistic Young's modulus of 18 Gpa and a Poisson's ratio of 0.11 we obtain the maximum seismic magnitudes as shown in Table 2-5.

In summary, the maximum possible seismic magnitude is 3.9, which is based on a shear modulus of 18 Gpa (in its turn based on a Young's modulus of 40 Gpa and a Poisson ratio of 0.11) and the dimensions of the internal fault. For a more realistic Young's modulus of 18 Gpa for the Rotliegend sandstone, the maximum possible seismic magnitude is 3.7 for the dimensions of the internal fault (the maximum magnitude recorded so far for the Bergermeer field is 3.5). Larger magnitude earthquakes are improbable due to the limited dimensions of the faults in the reservoir.

2.2.2 Temperature change and pore pressure change

The maximum slip displacement can also be calculated from the strain taking into account pore pressure changes and temperature changes. The strain is given by the change in pore pressure and temperature as (Logan, 1997)

$$\Delta\varepsilon_3 = \frac{-(\zeta\Delta p + K\alpha_s^{'}\Delta T)}{\lambda(1+2R)+2\mu}$$

where Δp is the pore pressure change, ΔT is the temperature change, ζ is assumed to be one, K is the bulk modulus, $\alpha_s^{'}$ is the cubic expansion coefficient, λ is the isothermal Lame constant, μ is the shear modulus and R is the ratio of lateral to vertical strain increment, which is zero if the strain is assumed to be uniaxial. This is a good approximation if the thickness of the reservoir is much less than the areal extent, which is the case for the Bergermeer field. We assume a Poisson's ratio ν of 0.175 and a shear modulus of 18 GPa (typical for the Rotliegend sandstone) and calculate the

isothermal Lame constant λ and the bulk modulus K with these parameters. The slip displacement can be calculated from the strain using

$$\Delta\varepsilon_3 = \frac{\partial u_3}{\partial z}$$

and

$$u_3 = \frac{\partial u_3}{\partial z}\Delta z$$

where Δz is the fault width and $\delta = u_3$ is the slip displacement. For the fault width, we use the fault width of the internal fault (448 m) as this is the largest width of the faults in the Bergermeer field.

Figure 2.4 shows the relation between the maximum slip displacement and a change in temperature or pore pressure. At constant temperature, the effect of depletion (decrease in pore pressure) is a downward (positive) slip displacement along the fault while re-injection (increase in pore pressure) leads to an upward (negative) slip displacement along the fault. An increase in temperature causes an upward slip while a decrease in temperature causes a downward slip.

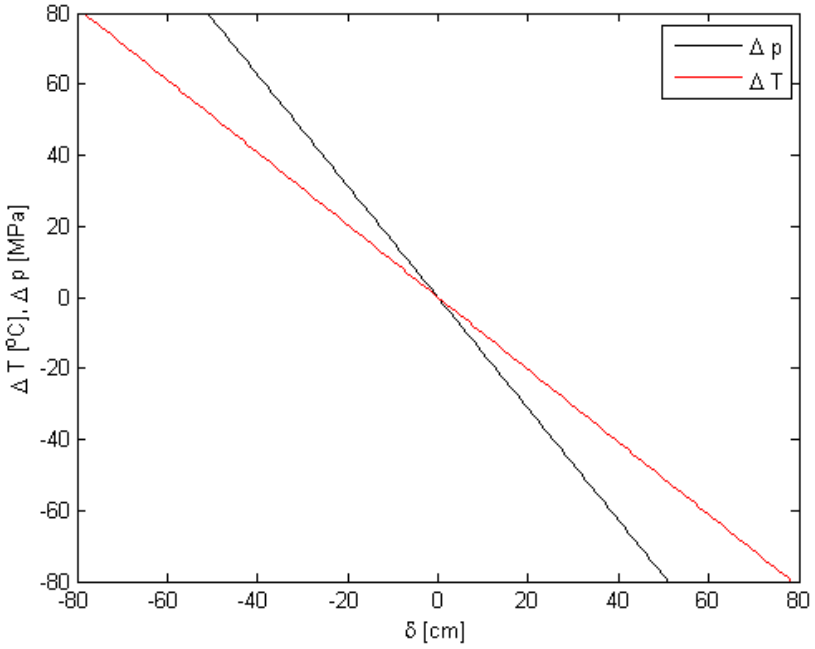

Figure 2.4: The relation between the maximum slip displacement and a change in temperature or a change in pore pressure.

3 Geological Model

3.1 Introduction

The purpose of the static modelling of the Bergermeer UGS site (BGM) was threefold:

1) To provide a static geologic model of the reservoir plus overburden to the geomechanical engineers for further modelling in DIANA;
2) To provide input to the reservoir simulation study;
3) To derive thickness maps of reservoir and overburden formations for subsidence modelling.

An existing Petrel/Eclipse model built by Horizon Energy Partners (hereafter Horizon), who performed a reservoir simulation study in 2006 for the BGM UGS, was reviewed and deemed suitable for TNO's thermal/compositional reservoir simulation. A high-resolution version of the model was used as a basis for further static modeling, in order to include the overburden. DIANA uses 2D cross-sections through the model, which needed to be digitized from Petrel cross-sections.

3.2 Geology of the BGM field

A good description of the sedimentary and structural geology of the Bergermeer Field can be found in Horizon's (2006) report. A brief recapitulation is given below.

3.2.1 Sedimentary geology

The reservoir, the Slochteren Sandstone, is of Permian age and consists of well-sorted, fine-grained aeolian sandstone. Average thickness of the Slochteren Sst in the Bergermeer Field is some 200 m. Porosity is in general high, ranging from 15 to 30% and averaging 23%. Vertically, the best porosities occur in the middle part of the Slochteren Sst (Figure 3.1). It is not entirely clear why the top part has such low porosities. In previous studies it has been attributed to Weissliegend facies although cores showed no facies differences across the Slochteren Sst. The reduced porosity might be attributed to pore filling of anhydrite, siderite, and quartz cement.

A number of thin low-porosity streaks occur throughout the reservoir.

3.2.2 Structural Geology

The Bergermeer Field lies on a narrow NW-SE trending horst block. The adjacent Groet Field lies on the same horst and is separated from the Bergermeer Field by a low-relief saddle. The BGM Field consists of two main fault blocks: a high main block and a lower south block (Figure 3.2). An internal fault separates the two fault blocks. Although this fault shows a clear tip point on 3D seismic, Horizon (2006) concluded from their reservoir simulation studies that the two fault blocks were not in pressure communication and hence, that the internal fault was longer than could be mapped from seismic and, more importantly, should be completely sealing.

The top and side seal of the BGM Field is provided by the evaporites of the Zechstein. The Zechstein directly above the BGM Field is quite thin (down to 100 m) due to fault gaps and salt flow.

A number of listric faults occur in the overburden. These were mapped out by Wim van Soest (TAQA) and made available to TNO.

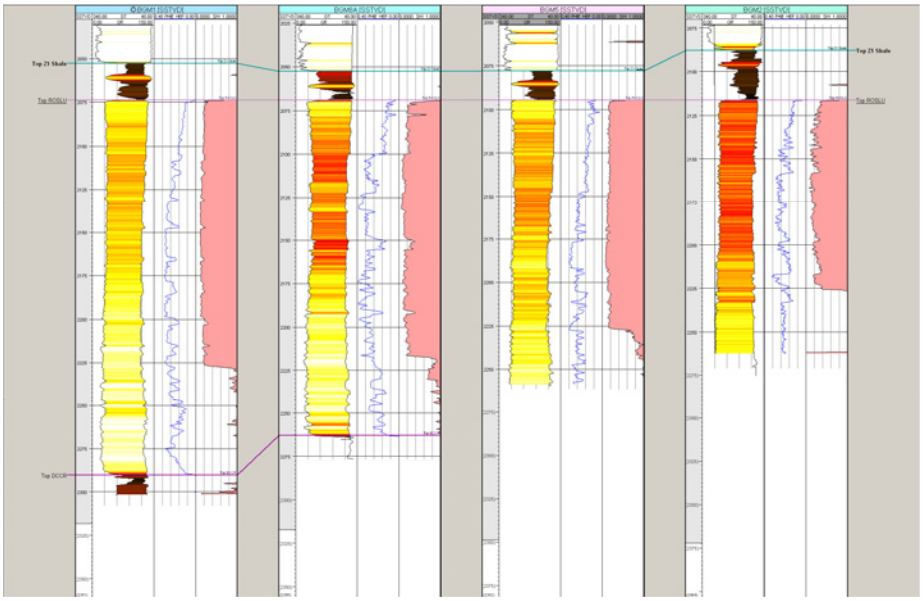

Figure 3.1: Well log panel through wells 1,2,5,8A showing reduced porosities near the top and base of the Slochteren Sst.

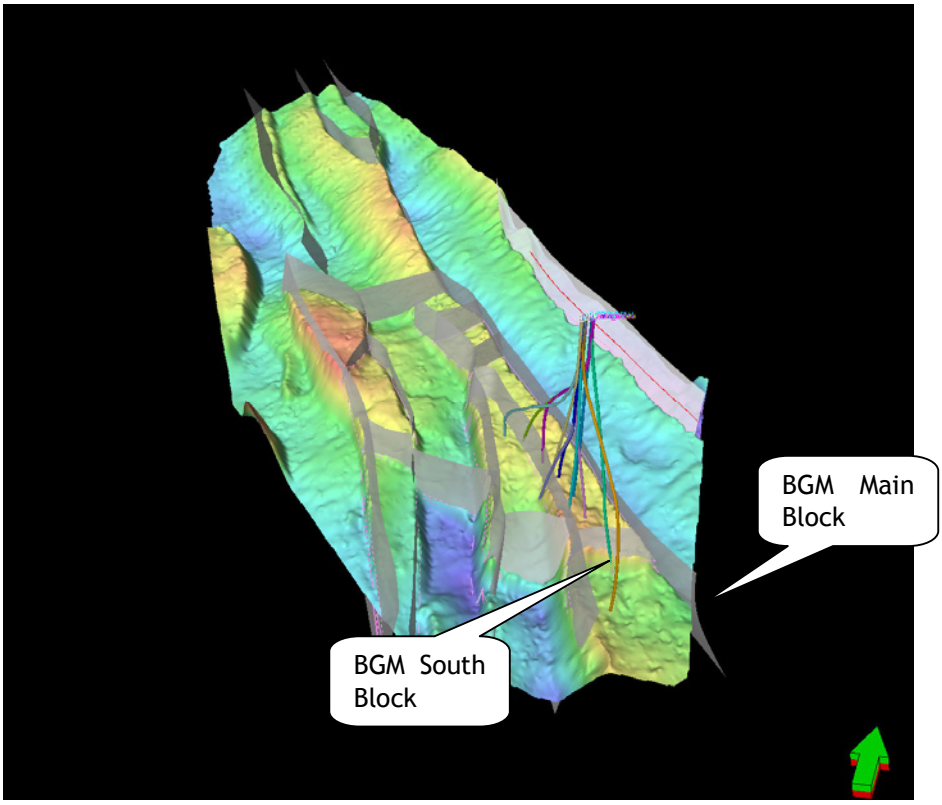

Figure 3.2: 3D view of the Bergermeer Field showing Top Slochteren surface, faults from Horizon's model, and BGM wells.

3.3 Preparation of the static model for Geomechanics

For the geomechanical modeling a hybrid model was built in Petrel, consisting of Horizon's Petrel reservoir model (Slochteren Sst only), plus a non-faulted overburden model, on which the overburden faults (exported from JS) are superimposed. Section 3.4 discusses the overburden surfaces in more detail. In addition, a separate Zechstein model was built in order to fine-tune the geomechanical behaviour of reservoir plus cap rock.
Bulk Zechstein lithologies were determined for the BGM wells using simple cutoffs on the gamma-ray and sonic logs (Figure 3.3). Using this approach, the following lithologies could be resolved with a great degree of confidence: shale, limestone, dolomite, halite, and anhydrite. Figure 3.4 shows the results for a number of wells.

After determining Zechstein lithologies for all BGM wells, the Zechstein was subdivided into six units with a more or less homogeneous lithology, from a geomechanical point of view. Occasionally they correspond with formal stratigraphic units, like ZeZ3C.
From top to bottom, these are (Figure 3.4, Figure 3.5): 'Halite', 'Dolomite', 'Middle Anhydrite', 'Mid-Ze Halite', 'L Anhydrite', and 'Z1 Shale'.
Well tops were picked for these informal units and subsequently used in the 'Make Zones' process to build a separate Petrel model for the Zechstein (see Figure 3.5). This model contained no faults, but used the faulted Top Slochteren Sst from Horizon's model as lowermost horizon.

A series of cross-sections was made in Petrel for further use in DIANA (Figure 3.6). Each cross-section was composed of
1) Horizon's Petrel model of the Slochteren Sst;
2) TNO's Petrel model of the Zechstein
3) Overburden horizons and faults based on TAQA's seismic interpretation.

Figure 3.3: Petrel log calculator script to determine Zechstein lithologies.

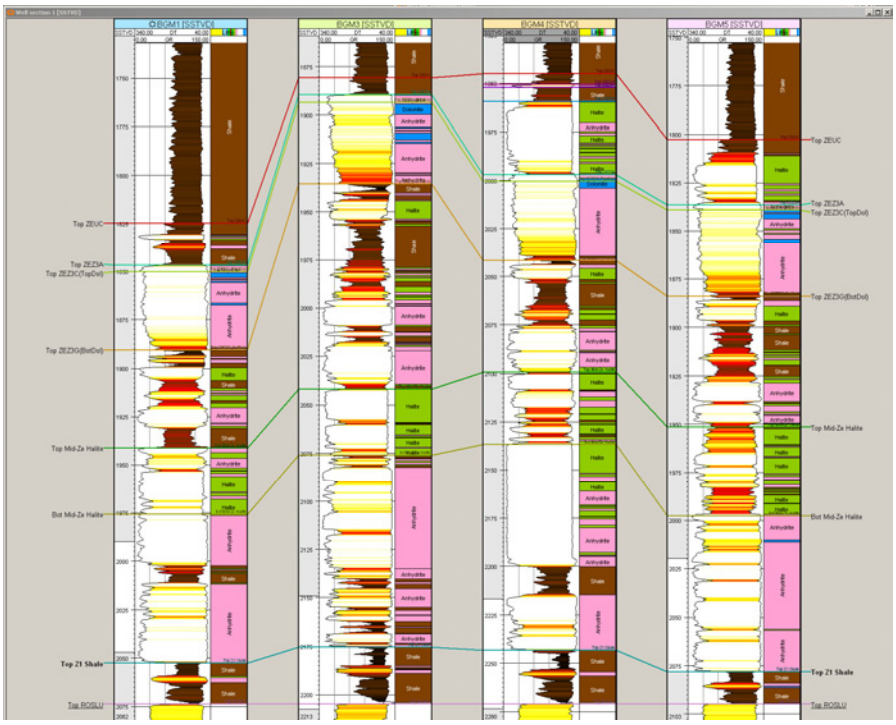

Figure 3.4: Results of the calculated lithologies for the Zechstein. Gross lithologies were grouped into informal units (e.g. the 'Mid-Ze Halite') and correlated.

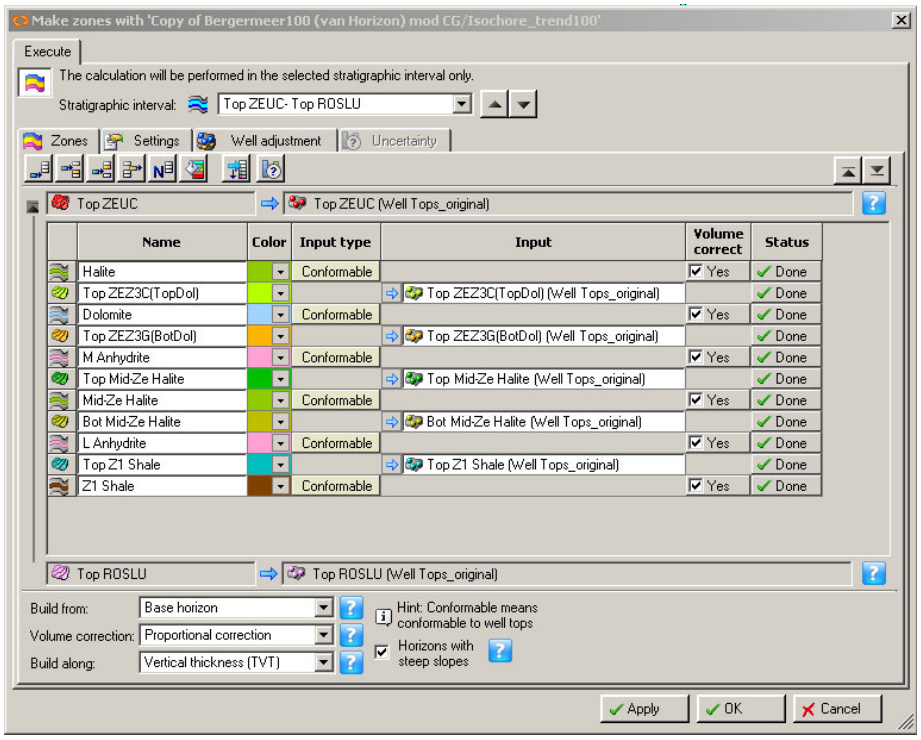

Figure 3.5: Parameters used in the zone building process of the separate Zechstein Petrel model.

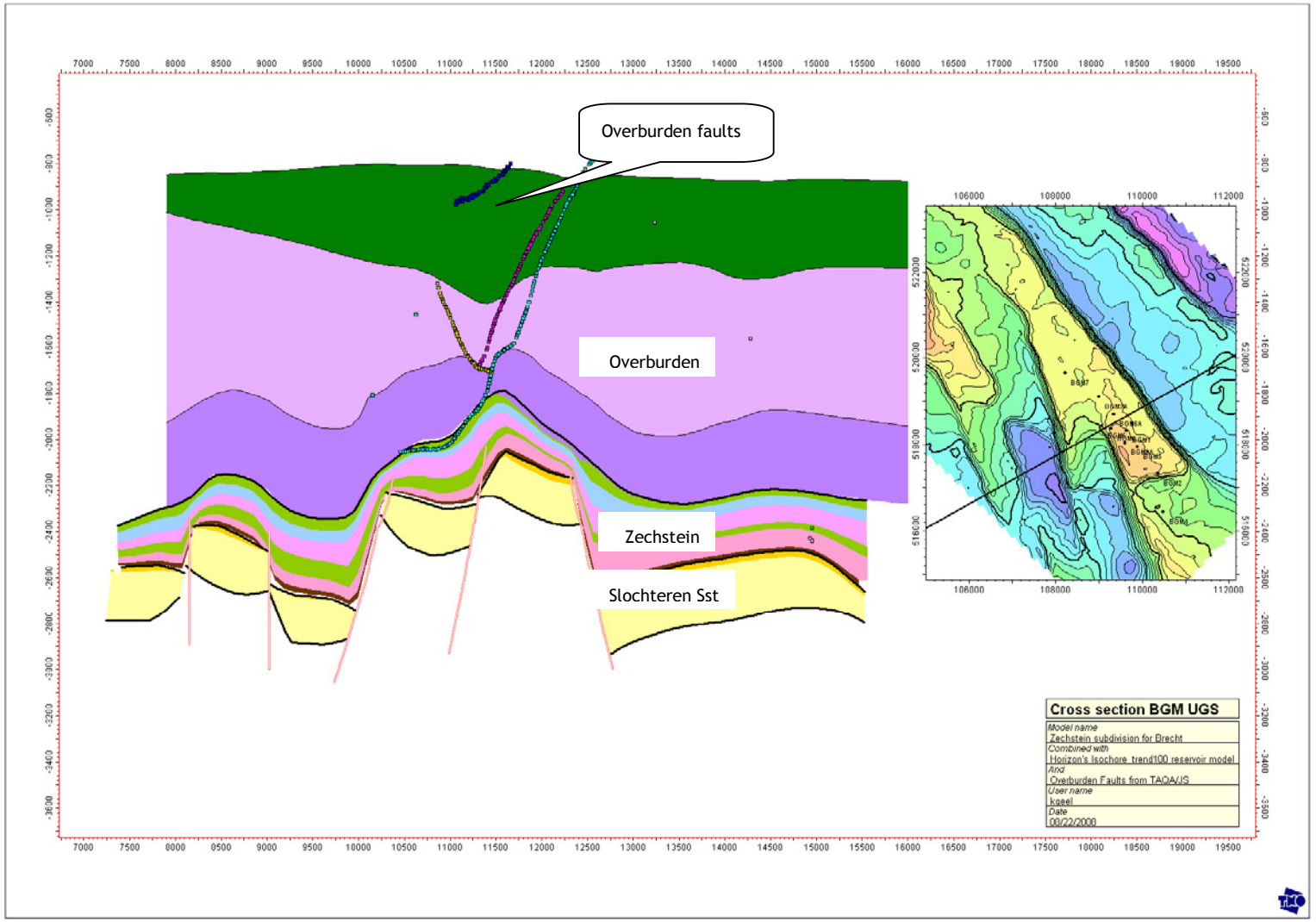

Figure 3.6: Cross-section through BGM field, composed of Horizon's Petrel model of the Slochteren Sst, a separate Petrel model for the Zechstein, and TAQA's overburden surfaces and faults.

3.4 Determination of formation thicknesses for subsidence modelling

The surfaces provided by TAQA were imported in Petrel as 'general point' files, and gridded.
The following surfaces were used:
01UCNS-CORDEP.XYZ
04UCKN-CORDEP.XYZ
07RMBH-CORDEP.XYZ
08RB01-CORDEP.XYZ
10ROSLU-DEPCOR_09DCOR010203DIV3_FAULTCUTOUT.XYZ
11DCCR-DEPCOR-FAULTCUTOUT.XYZ

For both seismicity and subsidence studies we needed a somewhat larger grid than the original data emcompassed. So each of the surfaces was extended (extrapolated) to fill up an approximate rectangle (See e.g. Figure 3.7).
For the subsidence modelling some overburden formations were grouped together (seeTable 3-1). These were formations that are believed to have similar geomechanical properties. Table 3-1 summarizes the results, Figure 3.7 to Figure 3.12 show individual isochore maps.

Table 3-1: Minimum, maximum, and average thicknesses for BGM reservoir and overburden.

Interval	**Min Thickness [m]**	**Max Thickness [m]**	**Avg Thickness [m]**
Tertiair (Noordzee Gp)	791	877	838
Holland + Vlieland	191	675	424
Keuper+Bunter	75	815	525
Main Claystone	38	441	309
Zechstein	0	596	293
Slochteren Sst	164*	415	271*

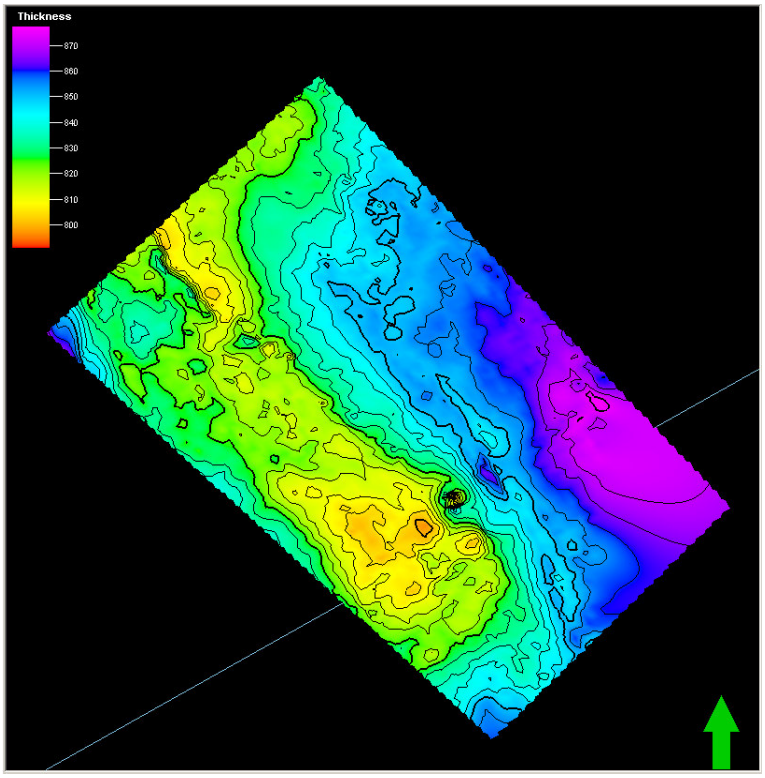

Figure 3.7: Isochore map of the Tertiary

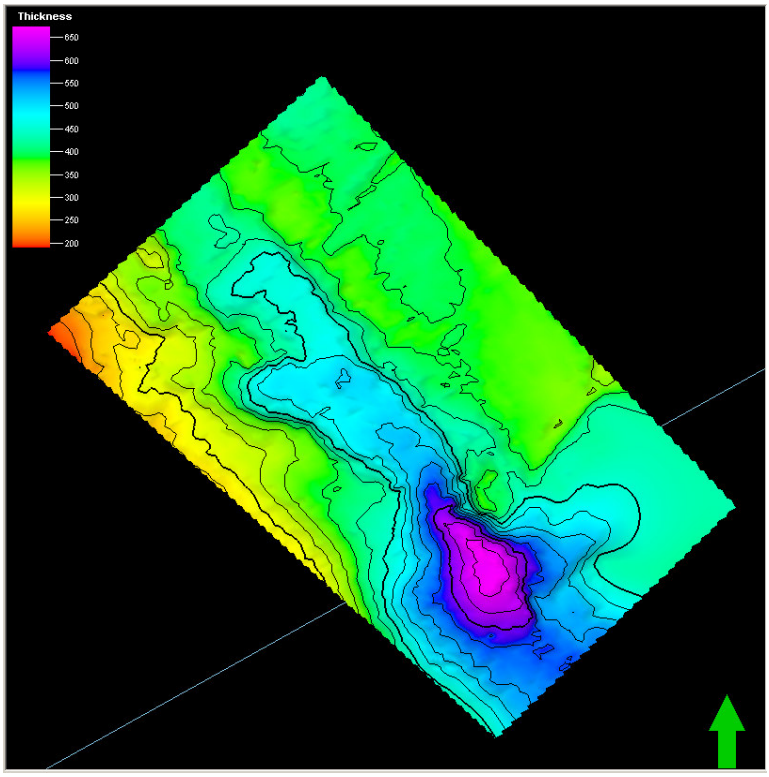

Figure 3.8: Isochore map of Holland + Vlieland Formations

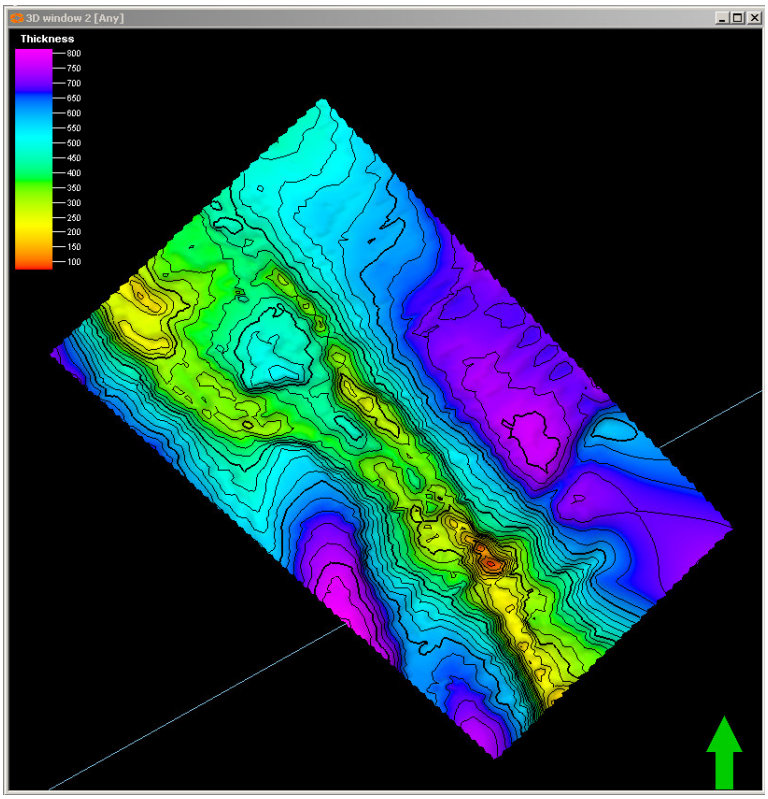

Figure 3.9: Isochore map of Keuper + Bunter Formations

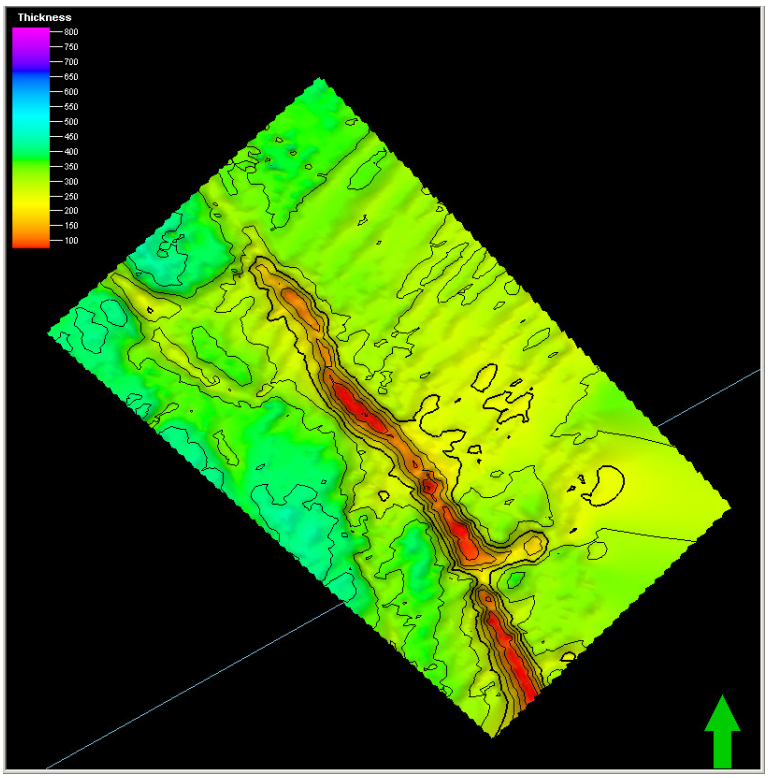

Figure 3.10: Isochore map of Main Claystone Formation

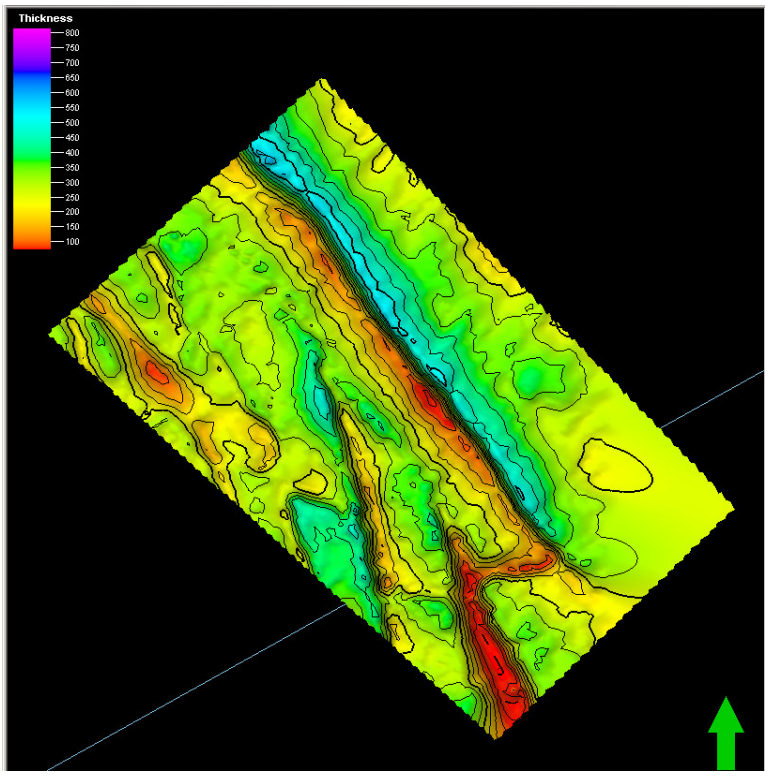

Figure 3.11: Isochore map of the Zechstein

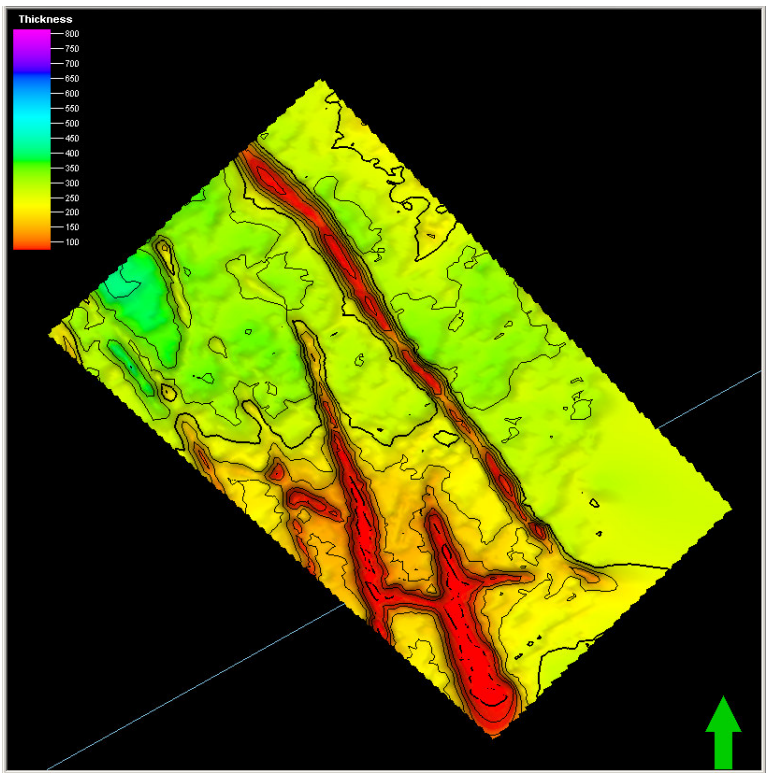

Figure 3.12: Isochore map of the Slochteren Sst

4 Subsidence Modelling

Rock elasticity properties are important for the geomechanical behaviour of the subsurface and therefore implicitly for the occurrence of motion on the faults present in and around the Bergermeer field. At the same time, these properties determine the response of the subsurface to reservoir compaction and induce surface subsidence.

The subsidence due to the depletion of the Bergermeer has been monitored frequently since the onset of production. In the subsidence modelling described in the underlying chapter these observations have been used to attempt to constrain the rock elastic properties.

We commence with a description of the subsidence data and the relation between subsidence and reservoir compaction. Subsequently, ranges for the elasticity parameters are derived from well log data. In the final section the subsidence information is used in an inverse procedure in order to attempt to constrain the uncertainty related to the parameters.

4.1 Subsidence Data

4.1.1 Levelling data Bergen concession

We have extracted all historic levelling data gathered on behalf of Amoco for the Bergen concession from the DID[13] database. The DID database has been subdivided in 765 map sections covering the whole of The Netherlands. The data of the Bergen concession are located in 6 different map sections: 14C, 14D, 19A, 19B, 19C, and 19D. In total we obtained 431 sites which were included at least once in an Amoco levelling campaign of the Bergen concession. These campaigns were held in 1980, 1981, 1984, 1988, 1992, 1997, 2001, and 2006. Additionally, we have extracted all additional primary and secondary NAP levelling measurements made for these sites (the fifth primary levelling campaign of the NAP network was conducted in 1997; secondary levelling campaigns were made in 1972, 1984, 1991, 1997, and 1999). A table containing the information gathered from the DID database has been made electronically available to TAQA. The locations of the levelling points are shown in Figure 4.1.

The levelling campaigns of 1980 and 1981 were combined to represent a single epoch in our inversion exercise. By combining the two campaigns the amount of epochs in the inversion exercise can be reduced without rejecting any information. The combination was warranted by the fact that for sites included in both campaigns little to no difference was found between the two measurements. Similarly, the Amoco campaign in 1992 was combined with the 1991 secondary levelling campaign of the NAP network. For this epoch, as well as for the 1984 and 1997 campaigns, the Amoco data was considered the main data set and the primary and secondary levelling campaigns were only considered for stations without an Amoco measurement in the epoch under consideration. In only three cases, the difference between the Amoco and NAP

[13] DID: Data-ICT-Dienst. This service of the ministry of Transport, Public Works and Water management manages all the leveling information which has been gathered for the monitoring of subsidence.

measurements was such that the Amoco measurements were declined and the NAP measurements retained.

All data has been referenced to the old NAP reference level. For the 2001 and 2006 campaigns this elicits the implementation of a correction factor (see Table 4-1). This correction factor is map section specific, where each map section has been subdivided in 4 subsections.

4.1.2 Levelling data Bergermeer

Generally, it is assumed that the subsidence bowl due to a compacting reservoir extends roughly as far laterally as the depth at which the reservoir is located. The Bergermeer field is located at a depth of 2100 m. Therefore, the levelling dataset of the Bergen concession must extend at least to some 2 km from the Bergermeer field boundaries. We reduce the levelling dataset to an area extending 5 km from the Bergermeer field boundaries (hence the rectangle given by the coordinates 101.5 km $\leq x \leq$ 116.5 km and 512 km $\leq y \leq$ 527.5 km).

From the remaining dataset, stations which were not included in at least two campaigns were excluded since no subsidence over any given time frame can be computed.

An overview of the data utilized in the inversion procedure is given in Table A-1.

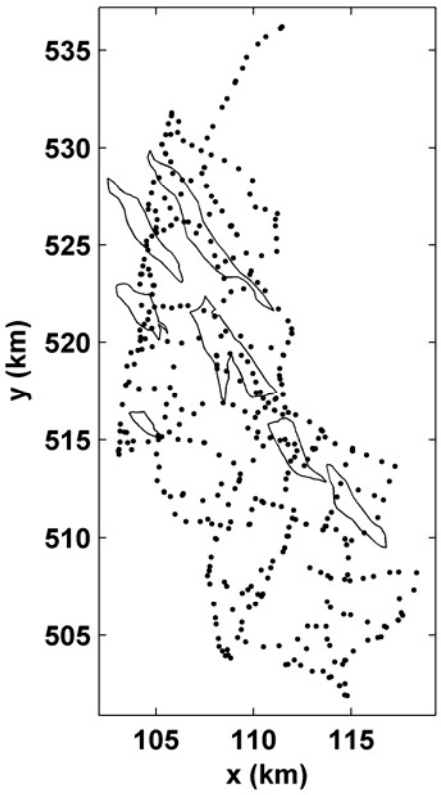

Figure 4.1: All levelling data locations of the Amoco campaigns of the Bergen Concession (1980, 1981, 1984, 1988, 1992, 1997, 2001, and 2006).

Table 4-1: Correction factors of new NAP reference level with respect to old NAP reference level (correction factor = NNAP – ONAP).

Map section	RD coordinates grid corners				Correction factor (m)
	xmin	Xmax	ymin	ymax	
14CN1	100000	105000	531250	537500	-0.0267
14CN2	105000	110000	531250	537500	-0.0268
14CZ1	100000	105000	525000	531250	-0.0261
14CZ2	105000	110000	525000	531250	-0.0257
14DN1	110000	115000	531250	537500	-0.0262
14DN2	115000	120000	531250	537500	-0.0257
14DZ1	110000	115000	525000	531250	-0.0260
14DZ2	115000	120000	525000	531250	-0.0255
19AN1	100000	105000	518750	525000	-0.0247
19AN2	105000	110000	518750	525000	-0.0247
19AZ1	100000	105000	512500	518750	-0.0228
19AZ2	105000	110000	512500	518750	-0.0232
19BN1	110000	115000	518750	525000	-0.0245
19BN2	115000	120000	518750	525000	-0.0239
19BZ1	110000	115000	512500	518750	-0.0229
19BZ2	115000	120000	512500	518750	-0.0225
19CN1	100000	105000	506250	512500	-0.0214
19CN2	105000	110000	506250	512500	-0.0218
19CZ1	100000	105000	500000	506250	-0.0206
19CZ2	105000	110000	500000	506250	-0.0207
19DN1	110000	115000	506250	512500	-0.0216
19DN2	115000	120000	506250	512500	-0.0214
19DZ1	110000	115000	500000	506250	-0.0207
19DZ2	115000	120000	500000	506250	-0.0202

Since production of the Bergermeer field commenced in 1972, the 1972 secondary levelling campaign was retained in order to provide a reference level. Additionally, in the inversion exercise the following epochs will be identified and utilized to constrain the temporal evolution of the subsidence: 1980/1981, 1984, 1988, 1991/1992, 1997, 2001, and 2006.

The total subsidence observed between 1972 and 2006 within the given dataset estimates at ~10.5 cm (Figure 4.2). This maximum is located roughly northwest of the Bergermeer field and is the result of the interaction between the depletions of the Bergen, Groet and Bergermeer fields. This interaction needs to be addressed in the inversion procedure. The implementation of the contributions of Bergen and Groet will be discussed in section 4.4.1.

4.1.3 Levelling data precision

The standard deviations for the NAP network points result from the levelling. At the location of the Bergermeer concession the standard deviations of the initial campaigns (1972, 1980, 1984, and 1988) amount to approximately 5 mm. For the more recent campaigns (1991, 1997, 2001, and 2006) the standard deviation amounts to 2-2.5 mm.

Regular benchmarks are less stable compared to the benchmarks of the primary NAP levelling network. Therefore, stochastic errors should be taken into account in addition

to the standard deviations. Generally for the Netherlands, these stochastic errors amount to 2 mm over a 10-year period (repetition frequency of the NAP; Brand et al, 2005). Here, in accordance with the general regulations of the DID for the NAP benchmark uncertainties, we have related the stochastic error to the temporal difference between each secondary campaign and the primary campaign of 1997:

$$\sigma_{st} = |t_s - 1997| \cdot (2 \text{ mm} / 10)$$

The resulting stochastic errors utilized for each campaign are given in Table 4-2.

Since the inversion procedure is based on the subsidence over a specific time frame, the relative precision between the height measurements bounding this time frame needs to be computed. Here we utilize the standard error propagation equation based on both the standard deviations of the benchmark in each campaign and the stochastic errors of the two campaigns:

$$\sigma_{rel} = \sqrt{(\sigma(t1)^2 + \sigma(t2)^2 + \sigma_{st}(t_1)^2 + \sigma_{st}(t_2)^2)}$$

Since both the standard deviations and the stochastic errors are only campaign dependent, the total errors of each benchmark in a particular campaign are identical. These errors are given in Table 4-3.

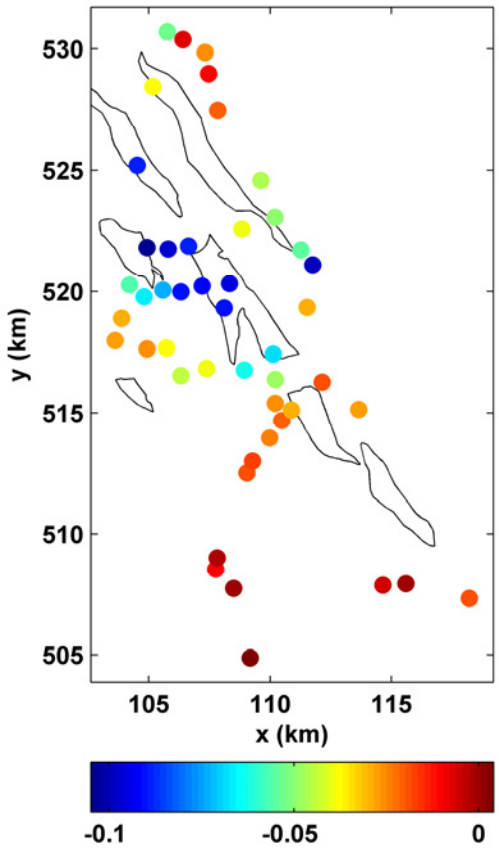

Figure 4.2: Total subsidence observed between points measured both in 1972 and 2006. The maximum subsidence estimates at ~10.5 cm and is roughly located northwest of the Bergermeer field.

Table 4-2: Stochastic error (in mm) for each campaign as utilized in this study.

year	1972	1980	1984	1988	1991	1997	2001	2006
σ_{st}	5.0	3.4	2.6	1.8	1.0	0	0.8	1.8

Table 4-3: Total error (in m) for the benchmarks contained in each campaign.

year	1972	1980	1984	1988	1991	1997	2001	2006
σ	0.224	0.191	0.178	0.168	0.085	0.079	0.068	0.085

4.2 Subsidence prediction from reservoir compaction

When reservoir pressure falls during gas production, the reservoir compacts. Prior to its exploitation, the reservoir will normally have reached equilibrium with the given effective stress state. However, the pressure drop associated with exploitation causes the effective stress to increase, which induces the rock to compact until equilibrium is re-established with the new effective state of stress. Due to the assumed elastic coupling between the reservoir and the surrounding rock, the compaction in the reservoir is transferred to the surface almost instantaneously, resulting in surface subsidence. However, because the subsurface is elastic, the subsidence extends over a wider area than the reservoir compaction. The area affected is roughly as extensive as the reservoir is deep. The precise form of the subsidence bowl resulting from the reservoir compaction depends on the elastic properties of the subsurface.

We use the linear, semi-analytic approach designed to account for layering (Fokker and Orlic, 2006) to relate reservoir compaction to subsidence. The method combines a number of analytic functions that satisfy the elasticity equations in such a way that the boundary conditions at layer interfaces and the ground surface are approximately correct (see Fokker and Orlic [2006] for details). The solution obtained by this method yields a subsidence bowl originating from a centre of compression, which is the mathematical representation of a finite amount of compaction concentrated at a single point. This solution is subsequently used as an influence function (Green function) in conjunction with the reservoir data to arrive at a subsidence bowl for the whole reservoir that is compacting. This method is applicable to linear theories since it relies on the superposition principle for solutions of the elasticity equations.

Considering that the reservoir pressures available from reservoir simulations are on discretized models, the total predicted subsidence resulting from reservoir compaction at a surface location is obtained by summation over all grid blocks in the reservoir:

$$u_3(x,y) = c_m \sum_i \partial V_i \cdot \partial P_i \cdot g(\sqrt{[(x-x_i)^2+(y-y_i)^2]}) \qquad (1)$$

In this equation g(r) indicates the influence function for vertical displacement at the surface, ∂V_i is the volume of the i-th grid block, ∂P_i is the pressure depletion in this grid block and c_m is the compaction coefficient.

The approximation of the influence function of a grid cell by the influence function of a centre of compression in its centre is appropriate as long as the ground surface is far enough away, i.e. the depth is more than 10 times the typical dimension of the grid block.

4.3 Elasticity parameters

The theory of elasticity holds that no significant damage or alteration of the rock results from an applied stress and the assumption that stress and strain are linearly proportional and fully reversible. The material properties known as Young's modulus and Poisson's ratio (E and ν, respectively) determine the elastic behaviour of the subsurface. The Young's modulus is the stiffness of a rock in unconfined uniaxial compression, while the Poisson's ratio is the ratio of lateral expansion to axial shortening.

4.3.1 Derivation of elasticity parameters

Young's moduli for Zechstein and overburden rocks are obtained from literature (Roest & Kuilman, 1994) and the sonic (V_p) and density logs in the Bergermeer wells. Dynamic and static stiffness values are obtained from the well logs, using the following equation:

$$V_P = 10^6 / (\Delta t \cdot 3.280839) \qquad V_P \text{ in m/s; } \Delta t \text{ in } \mu\text{s/ft}$$

For calculation of dynamic stiffnesses either the value of V_s (velocity shear wave) or the Poisson's ratio should be known. No sonic logs of V_s are available for the Bergermeer field, nor measured values of the Poisson's ratio for all units. Empirical relations for the ratio of V_p/V_s are used for various lithologies (Domenico, 1984, Castagna, 1985).

Density, V_s and V_p are used to calculate dynamic stiffness, which can be further transformed into static Young's moduli (Eissa and Kazi, 1988).

$$E_{dyn} = \rho V_s^2 .(3V_p^2 - 4V_s^2) / (V_p^2 - V_s^2) \quad E_{dyn} \text{ in kPa; density } (\rho) \text{ in g/cm}^3$$
$$E_{stat} = 0.64 \cdot E_{dyn} - 3.2 \cdot 10^5 \qquad E_{stat} \text{ in kPa}$$

Poisson ratio's for all units are obtained from literature (Logan, 1997, Roest & Kuilman, 1994).

Table 4-4 summarizes the elasticity parameter ranges obtained for the various geological units.

4.3.2 Sensitivity of subsidence to subsurface elasticity parameters

The amount of subsidence observed, as well as the lateral extent of the subsidence bowl is directly related to the elastic parameters of the reservoir and overburden layers. Weaker layers in the subsurface induce more vertical displacement compared to more rigid layers. At the same time, due to the lateral distribution of the displacement in the weaker layer, the extent of the subsidence bowl decreases.

For the Bergermeer field the total effect of the ranges for the parameters as derived in the previous paragraph, yield a 2.6 cm difference in depth and a 1.325 · 10-6 m3 difference in the volume of the subsidence bowl.

A preliminary sensitivity analysis of the ranges provided for the elasticity parameters of the Bergermeer field shows that ***the uncertainty in Poisson's ratio mainly affects the depth of the subsidence bowl and has very limited influence on the lateral extent.*** Particularly, the influence on the extent is for 99% due to the uncertainty in the ratio of

the Zechstein formation. The depth of the subsidence bowl is mainly related to the Poisson's ratio of the Tertiary and Keuper/Bunter formations (93,4%).

The uncertainty in Young's moduli has a comparable influence on both the depth and lateral extent of the subsidence bowl. Again the lateral extent of the subsidence bowl is mainly influenced by the modulus of the Zechstein formation. However, the influences of the moduli of the other layers are not negligible. The depth of the subsidence bowl is equally influenced by the moduli of all layers with the exception of the range of Young's modulus for the Tertiary which has a slightly smaller influence

4.4 Subsidence inversion

For the Bergermeer field and overburden we have determined quite large ranges of uncertainty for the elasticity parameters. The linear inversion procedure developed by TNO (as described below) incorporates the elastic behaviour of the reservoir and overburden layers in the semi-analytic forward method (see section 4.2). Therefore, it is impossible to constrain these parameters directly by a linear inversion of the observed subsidence data. However, we have explored the feasibility of inferring the uncertain compaction coefficient from the subsidence information. Additionally, we attempt through multiple inversion constrain the uncertainty in the elastic parameters. The discrimination between the inferred models is based on the normalized χ^2 and the root mean square error.

Table 4-4: Ranges for the elasticity parameters for the different geological units.

Geological Unit	Youngs modulus (GPa)	Poisson ratio (-)
Tertiary rocks	0.1-1	0.29-0.38
Vlieland Shales & Holland Marls	1-15	0.23-0.24
Musschelkalk, Bunter & Keuper	5-35	0.24-0.3
Main Claystone	15-35	0.25-0.3
Zechstein Formation	20-50	0.25-0.3
Rotliegend Slochteren sandstone	10-26	0.1-0.25
Carboniferous	30	0.25

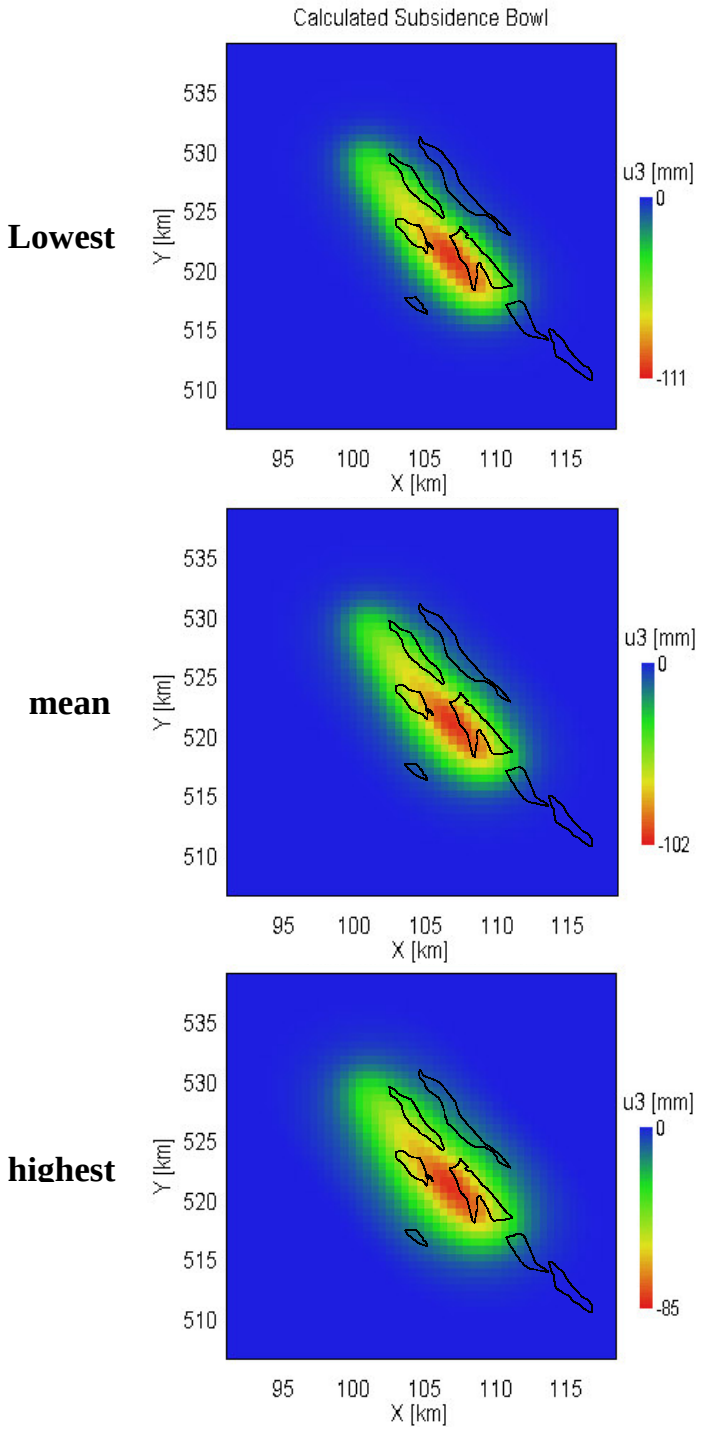

Figure 4.3: Subsidence bowl computed for the Bergermeer-Groet reservoir model based on a compaction coefficient of 3.5 10-5 bar-1 and elasticity profiles using the least values for the parameters (left), the minimum values (middle), and the highest values in the ranges for the elasticity parameters (right). Clearly the implementation of weaker overburden layers (the lowest values) induces a smaller but deeper subsidence bowl, whereas stronger overburden layers (the highest values) induce a wider shallower subsidence bowl compared to the subsidence bowl compute for the mean values of the elasticity parameters (middle figure).

4.4.1 Procedure

4.4.1.1 Methodology

For a set of subsidence observations, equation (1) yields a linear, coupled system of equations represented by $\mathbf{Gm} = \mathbf{d}$, where $\mathbf{G}$ is the coefficient matrix relating the subsidence observations u_3, gathered in the data vector $\mathbf{d}$ to the model parameters (reservoir pressure drop, or compaction) gathered in the vector $\mathbf{m}$. Some of the uncertain properties of the forward model, like the compaction coefficient or an unknown global bias in the subsidence measurements (unstable reference level), can also be incorporated in the model vector $\mathbf{m}$ (Schroot et al, 2005).

The formal least squares solution of our system is (Muntendam-Bos et al, 2008):

$$\mathbf{m} = \mathbf{m}_0 + \mathbf{C}_m\mathbf{G}^T (\mathbf{G}\mathbf{C}_m\mathbf{G}^T + \mathbf{C}_d)^{-1} (\mathbf{d}-\mathbf{G}\mathbf{m}_0) \qquad (2)$$

where $\mathbf{m}_0$ is the prior model, and $\mathbf{C}_d$ and $\mathbf{C}_m$ denote the data and prior model covariance matrices, respectively. The diagonal elements of the matrices comprise the squared errors on the data and model parameters. In case relations (cross correlations) in both space and time are absent, the off-diagonal elements of the covariance matrices will be zero. The superscript ^{T} denotes the transposed. The corresponding posterior covariance is given by

$$\mathbf{C} = \mathbf{C}_m - \mathbf{C}_m\mathbf{G}^T (\mathbf{G}\mathbf{C}_m\mathbf{G}^T + \mathbf{C}_d)^{-1} \mathbf{G}\mathbf{C}_m$$

and the model resolution kernel is

$$\mathbf{R} = \mathbf{C}_m\mathbf{G}^T (\mathbf{G}\mathbf{C}_m\mathbf{G}^T + \mathbf{C}_d)^{-1} \mathbf{G}.$$

Inversion is now dependent on the prior model ($\mathbf{m}_0$) and the prior model covariance matrix ($\mathbf{C}_m$). The non-zero covariance in $\mathbf{C}_m$ quantifies expected relations between grid points in space and time (Kroon et al, 2008; Muntendam-Bos et al, 2008). Such knowledge is often available, even when the absolute values of the initial compaction models are quite uncertain.

For the case at hand, the primary uncertainty is the range of feasible compaction coefficients: $0.1 \cdot 10^{-5}$ – $3.3 \cdot 10^{-5}$ bar^{-1}. We adopt a Monte Carlo approach of simulating the compaction volume for 5 pseudo-random compaction coefficients within this range with a log-normal distribution centred at $1.7 \cdot 10^{-5}$ bar^{-1}.

The temporal aspect of the problem is implicit in equation (2). In order to ensure that all available measured data is used optimally, the method was extended to deal with stations that are not included in every campaign (see Muntendam-Bos et al, 2008 for details). Basically, for each site omitted from one or more observation campaigns, the difference between the measurements in the campaign following the omission and the campaign preceding the omission is related to all the intermediate models.

4.4.1.2 Incorporation of neighbouring fields

The Bergermeer field is not a solitary reservoir in the Bergen Concession; it is surrounded by neighbouring fields Alkmaar, Bergen, and Groet. Therefore, the subsidence pattern observed in the levelling data of the Bergen Concession represents the superposition of the subsidence bowls due to each of the four fields. This

superposition needs to be addressed prior to utilizing the subsidence observations of the Bergen concession to constrain parameters of the Bergermeer field.

We have adopted the approach of approximating the influence of the additional fields by incorporating additional model parameters. Since the depletion of the Groet field was included in the history match model of Horizon Energy Partners BV., we have a good control on the reservoir compaction of this field. Therefore, the compaction of this field has been approximated by 6 additional model parameters, which contain an identical total compaction volume as the complete history match model, as well as result in a comparable subsidence bowl at the earth's surface. The Bergen and Alkmaar fields have been approximated by including a single additional model parameter for each field with a significantly uncertain compaction volume. This uncertainty was incorporated in the model covariance matrix in conjunction with the uncertainty in the compaction coefficient.

4.4.2 Results

In order to test the sensitivity of the inversion to the elasticity parameters, we commence with the inversion for the mean, minimum and maximum values available for all elasticity parameters. In the inversion the mean thicknesses for the model layers were used (see Table 3-1). As a measure for the goodness of fit of the inversion results to the data, we utilize the normalized χ^2 and the root mean square error. Table 4-5 shows the values obtained for these parameters, as well as the inferred compaction coefficient and its uncertainty. Based on the goodness of fit criteria it is impossible to discriminate between the different models. Clearly, the variations in the elasticity parameters do influence the obtained compaction coefficient, but can equally well fit the data within its uncertainty. It is therefore, given the prior uncertainty in cm not feasible to narrow the uncertainty in the elasticity parameters based on the inversion of subsidence data. The uncertainty in the compaction coefficient has been narrowed. Based on the subsidence data the range is between $0.3 \cdot 10^{-5}$ – $1.1 \cdot 10^{-5}$ bar^{-1}. This decrease of the uncertainty range may be important for the geomechanical modelling described in Chapter 6 and future subsidence prediction calculations.

Table 4-5: Values obtained for the χ^2, rms error, inferred c_m and $\sigma(c_m)$.

Model	χ^2	rms error	c_m	$\sigma(c_m)$
Mean E & ν	0.70	0.096	$0.65 \cdot 10^{-5}$	$0.35 \cdot 10^{-5}$
Min E & ν	0.70	0.096	$0.60 \cdot 10^{-5}$	$0.33 \cdot 10^{-5}$
Max E & ν	0.70	0.096	$0.75 \cdot 10^{-5}$	$0.36 \cdot 10^{-5}$

.

5 Reservoir Engineering

The scope of this study is to assess the risks of seismic activity induced by pressure and temperature changes resulting from cold gas injection and gas production. The objective of the dynamic reservoir modeling study, presented in this chapter, is to model these pressure and temperature changes. The results will be used in the geomechanical analysis presented in Chapters 6 and 7.

The first section presents the dynamic reservoir model. In the second section the injection/production schedule for UGS as designed by TAQA is explained. Section three discusses the results. To quantify the effect of numerical dispersion, particularly on the temperature distribution, a single well was modeled with different grid block sizes. This sensitivity analysis is discussed in the fourth section. Finally, conclusions and recommendations are presented.

5.1 Dynamic reservoir model

Horizon[14] has conducted a dynamic modeling study of the production phase (from 1972 to 2007) of the Bergermeer field using the Eclipse 100 isothermal/blackoil simulator. This study is reported in Horizon's "Bergermeer UGS Modeling study, phase 2" report. The best history match case[15] from this study (named BaseModel hereafter) is used as a starting point for the underlying study.

Since temperature effects are important, the compositional/thermal simulator Eclipse 300 has been used. Apart from PVT data, temperature data and thermal properties of gas and rock, the input for the compositional/thermal model is the same as for the BaseModel.

5.1.1 Basic model data and Gas Initially in Place

The main data of the model are presented in Table 5-1 below.

The distribution of the gas initially in place is given in Table 5-2. The total volume of gas initially in place is 17.61 Bsm^3,[16] with 13.61 Bsm^3 in block-1 and 4.0 Bsm^3 in block-2.

Table 5-1: Main reservoir model data.

Average permeability	Horizontal 600 mD; Vertical 300 mD
Average porosity	19.7%
Grid dimensions	Nx=58; Ny=182; Nz=25; Total active blocks = 92000
Average grid block size	Length 100 m; Width 100 m; Height 10 m
Initial pressure	238 bar
Pressure at end of production	Block 1 15 bar; Block 2 25 bar

[14] Horizon Energy partners BV
[15] "BAG25_ALT2_DISMIDHIGHKV_BELL_050_ECLIPSE100"
[16] sm^3: standard m^3 @ 15 ^oC and 1 atm.

Table 5-2: Gas Initially In Place

Block	**GIIP** (Bsm^3)
Block-1 (reservoir compartment containing well BGM1)	13.61
Block-2 (reservoir compartment containing well BGM7)	4.00
Total	17.61

5.1.2 Thermodynamical data

Thermodynamic processes take place in the well and in the reservoir.

The processes in the well are modeled by TAQA and not further discussed here. Resulting Bottom Hole Temperatures (BHT) are used as input for the underlying model.

In the reservoir, two important thermodynamical processes take place: heat convection and heat conduction. For the Bergermeer field, heat convection takes place by the flowing gas. Heat conduction takes place between the gas and the rock and connate water, within the rock/connate water, and within the gas. In Eclipse 300 heat conduction is assumed to take place instantaneously with a grid block. Heat conduction between grid blocks and between the reservoir and cap and base rock has a minor impact compared to the heat convection because of the relatively small temperature gradients, the large dimensions of the reservoir, the low heat conductivity of rock/connate water, and the high gas flow rate. Still, heat conduction within the reservoir and from reservoir to cap and base rock has been modeled.

Key parameters for the thermodynamic processes are the initial temperature, heat capacity, and thermal conductivity of reservoir, cap and base rock, and gas, and the temperature at the bottom hole of the injected gas.

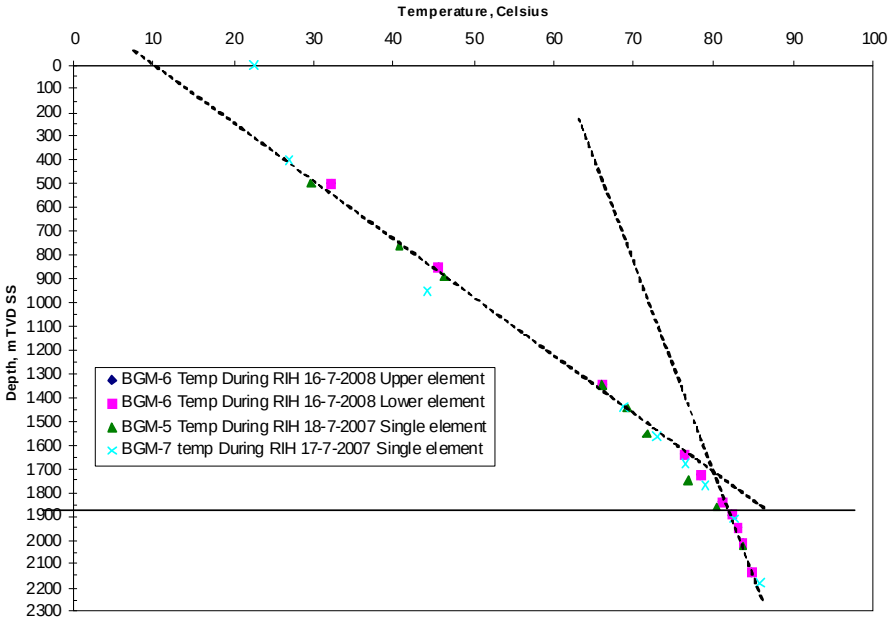

Figure 5.1: Temperature at some well locations of the Bergermeer field.

Table 5-3: Initial temperatures and rock thermal properties.

	Initial temperature (^oC)	**Thermal conductivity (kJ/m/day/K)**	**Heat Capacity (kJ/m3/K)**
Cap rock (Zechstein)	82	600	3200
Reservoir rock - Sandstone	89	250	2200
Reservoir rock - Shale	89	150	3000
Base rock (Carboniferous)	90	350	2200

Table 5-4: Composition of initial reservoir gas and injected gas (% mole fraction).

	Methane	**Ethane**	**Propane**	**Butane**	**Pentane**	**Hexane**	**Heptane**	**CO_2**	**N_2**
Initial	94.530	3.048	0.444	0.165	0.048	0.019	0.077	0.699	0.970
Injected*	85.100	3.300	0.700	0.080	0.030	0.004	0.000	0.740	3.900

*) Excludes 6% H_2O

Initial temperature data from TAQA are used (see Figure 5.1). Measurements in the cap Zechstein formation show a temperature gradient of 0.042 °C.m^{-1}. The reservoir and base Carboniferous formation have a gradient of 0.052 °C.m^{-1}. The average reservoir temperature is 89 ^{o}C. In the model the initial reservoir temperature is linearly depth dependent with 82 ^{o}C at 1900 m and 90 ^{o}C at 2800 m depth.

Heat capacity and thermal conductivity of rocks were taken from the *Handbook of physical constants. Clark, S.P, Jr 1966. Geol.soc.Am. Mem.,97,587*. Table 5-3 shows initial temperatures and the properties used for each formation.

Thermal conduction between cap and base rock and the reservoir is modeled using the Eclipse numerical method.

5.1.3 Matching the compositional/thermal model to the blackoil BaseModel

In this study, a nine component compositional model is used. Table 5-4 gives the composition of initial reservoir gas and injected gas

The compositional/thermal model, used for this study, results in slightly different gas properties, such as gas expansion factor, as compared to the blackoil BaseModel. These differences have a small effect mainly on the GIIP and on the average pressure of the reservoir during production and injection. To mitigate these differences, in the compositional/thermal model pore-volumes were slightly adjusted in the gas zones. This resulted in a very accurate match between BaseModel and compositional/thermal model.

5.2 Underground Gas Storage

The target underground gas storage and production schedule was specified by TAQA as summarized in Table 5-5 below.

First a gas cushion is build-up followed by yearly injection/production cycles. A gas cushion of 5.8 Bsm^3 is build up over a period of 20 months, during which the field repressurizes from 11-26 to 88 bar. Subsequently, over a period of 3 months, 3.7 Bsm^3 working gas is injected and average pressure increases to 133 bar. During the following

4 months production phase, the field depressurizes to 90 bar. The cushion gas injection phase and injection/production cycle are explained in detail below.

5.2.1 Well injection bottom hole temperature (BHT)

Well injection BHT was calculated by TAQA (see Figure 5.2). The BHT is decreasing as a function of injection rate. BGM-6 has a tubing of 5½" and BGM-8 of 7". Hence, BHT is also decreasing as a function of tubing size.

5.2.2 Cushion gas injection phase

The schedule for the injection of cushion gas depends on the deliver capacity of the grid. Based on the information the TAQA received from the company that manages the grid, a cushion gas injection schematic was made and provided to TNO.

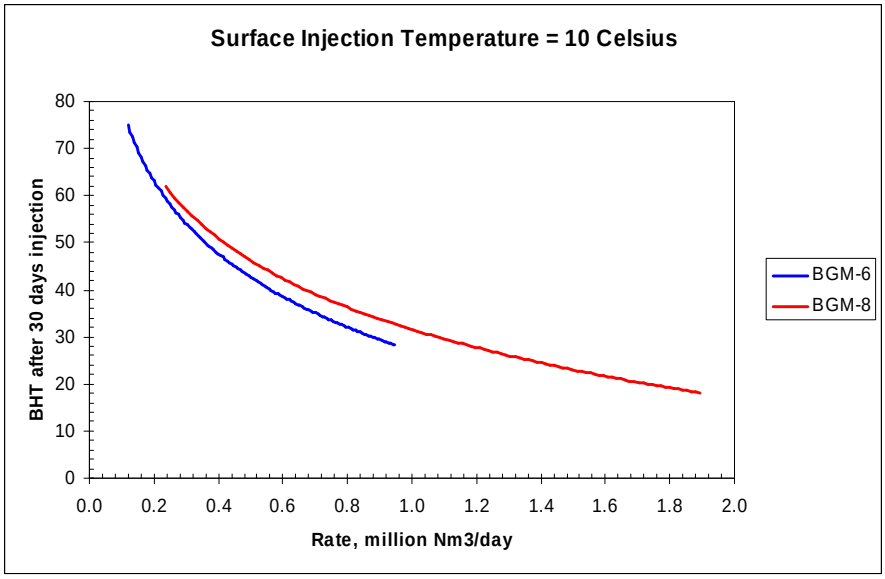

Figure 5.2: Bottom hole temperature as function of injection rate.

Table 5-5: Gas storage and production specifications.

Reservoir pressure at the beginning of injection	Block-I: 11 bar Block-II: 26 bar
Reservoir pressure after cushion gas injection	88 bar
Reservoir pressure after working gas injection	133 bar
Volume of injected cushion gas	5.5 Bsm^3
Volume of injected working gas	3.5 Bsm^3
Field injection rate	20- 40 Msm^3/day
Field production rate	30- 59 Msm^3/day
Number of wells	6 existing wells 14 new wells

Table 5-6: Injection rate schedule for cushion gas injection.

Year	Injection Period (days)	Field Injection (Bsm^3)	Field Injection Rate (Msm^3/day)	BHT (^oC)
2010	183	1.88	10.4	20 – 30
2011	183	2.09	11.5	20 – 30
2012	183	1.54	8.3	60 - 66

Table 5-7: Injection well schedule for cushion gas injection.

Block-1					
Well	**H/V***	**E/N†**	**2010**	**2011**	**2012**
BGM1	V	E	x	x	x
BGM2	V	E	x	x	x
BGM5	V	E	x	x	x
BGM6	V	E	x	x	x
BGM8	V	E	x	x	x
VPROP3	V	N		x	x
VPROP4	V	N	x	x	x
VPROP5	V	N		x	
Block-2					
Well	**H/V***	**E/N†**	**2010**	**2011**	**2012**
BGM7	V	E	x	x	x
HPROP01	H	N		x	x
HPROP02	H	N		x	x
HPROP11	H	N		x	x
HPROP12	H	N			x
HPROP13	H	N		x	x
HPROP14	V+H	N	x		
HPROP15	V+H	N	x		
HPROP16	V+H	N	x		

*) Horizontal or vertical well

†) E = Existing well, N = new well

The average injection BHT rises to 60 - 66 ^oC in 2012 due to the use of compressors.

Table 5-7 shows the scheduling of wells used for injection of cushion gas. To meet the grid delivery capacity, additional wells are drilled. Horizontal wells are completed with a tubing diameter of 7 5/8", vertical wells with 9 5/8" tubing.

At the beginning of the cushion gas injection the pressure in block-1 is 15 bar and in block-2 25 bar. The injection scheme results in an equal average pressure of 88 bar in both Block-I and Block-II at the end of the cushion gas injection phase.

5.2.3 Injection/production cycle

A single injection/production cycle takes about 6 months. The first injection/production cycle schedule designed by TAQA is shown in Table 5-8 and Table 5-9 below.

Table 5-8: Well schedule for injection/production cycle for 2013.

Injection Phase		**Production Phase**	
Month	**Field Injection Rate (Msm^3/day)**	**Month**	**Field Production Rate (Msm^3/day)**
April	41.84	End June	59.00
May	39.72	July	53.00
June	37.58	August	45.00
		September	41.00

Table 5-9: Injection/production cycle schedule for 2013.

Block-I	VPROP1, VPROP3, VPROP4, VPROP5, VPROP6, VPROP7, VPROP8, VPROP9, VPROP10, BGM1, BGM2, BGM5, BGM6, BGM8
Block-II	HPROP01, HPROP02, HPROP11, HPROP12, HPROP13, BGM7

Note: The names correspond to the Eclipse simulator and are not the final well names.

5.3 Results

The temperature distribution in the field after injection of the cushion gas and one injection/production cycle is shown in Figure 5.3.

The initial average reservoir temperature is 89 °C. After injection, the largest temperature gradients are located around the wells. Temperature falls down to 50 °C in a radius of 50 m around the injection wells. In a radius of 100 m around the injection wells, the temperature falls to 72 °C.

The first two years of injection are most important as after two years, injection gas needs to be compressed and BHT increases to 60-66 °C. Hence, the difference between BHT and initial reservoir temperature of some 89 °C becomes smaller.

5.4 Sensitivity analysis

Numerical modeling involves errors, amongst others due to numerical dispersion. To quantify the effect of numerical dispersion on the temperature distribution, the temperature distribution around a single well was modeled with different grid block sizes.

The grid block dimensions of the course grid are the same as those in the full model. In the fine grid, the grid block size in the lateral direction is 1/10 of that in the course grid. Block length in the z-direction is the same for both grids. In the single well model the pressure boundaries are open, porosity and permeability are homogeneous, the injection schedule for well BGM8 is used, and all other properties, like for instance temperature gradients and fluid composition, are the same as in the full model.

The results (Figure 5.4 and Figure 5.5) show that at a scale of 100 m or more the average temperature distribution for the course and the fine grid are comparable. The fine grid model does show a much steeper temperature gradient within a radius of 50 m around the well. The average temperature within this radius is comparable for both grids.

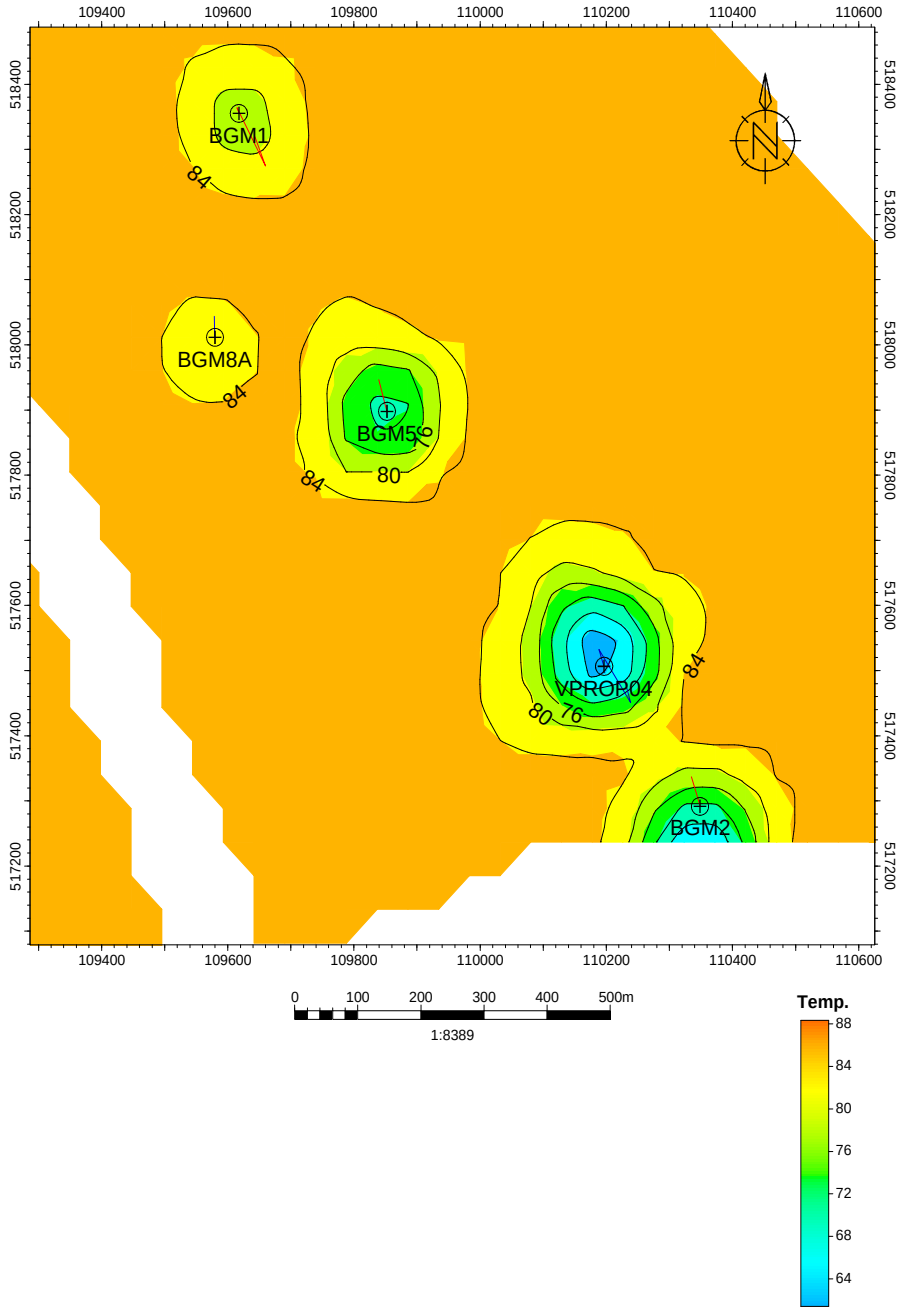

Figure 5.3: Temperature distribution at 24th of October for layer 13. Although this is just after the fisrt cushion gas injection period, the lowest temperatures are reached at this date as 1) injection gas temperature is lowest at 20-30°C, as compared to 60-66°C in later phases, and 2) injection rates per well are high as only 6 wells are injecting, while in later phases up to 17 wells are injecting.

The driver for induced seismic activity is compaction of the rock due to temperature and pressure decline. For this, only the average compaction volume at a scale >100m is important. Hence, the results of the course grid are generally sufficiently detailed as input for the geomechanical modeling. However, for wells close to faults (say <150m) the course grid used in the full model may not provide sufficient detail to accurate calculate the effect of temperature changes on rock cohesion failure.

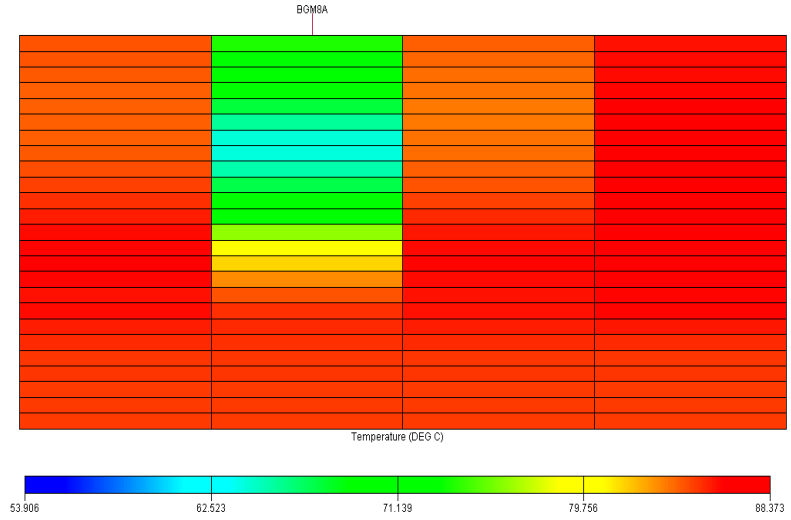

Figure 5.4: Cross section of the single well model with grid block sizes equal to the full model: length=width=100 m and height=10 m.

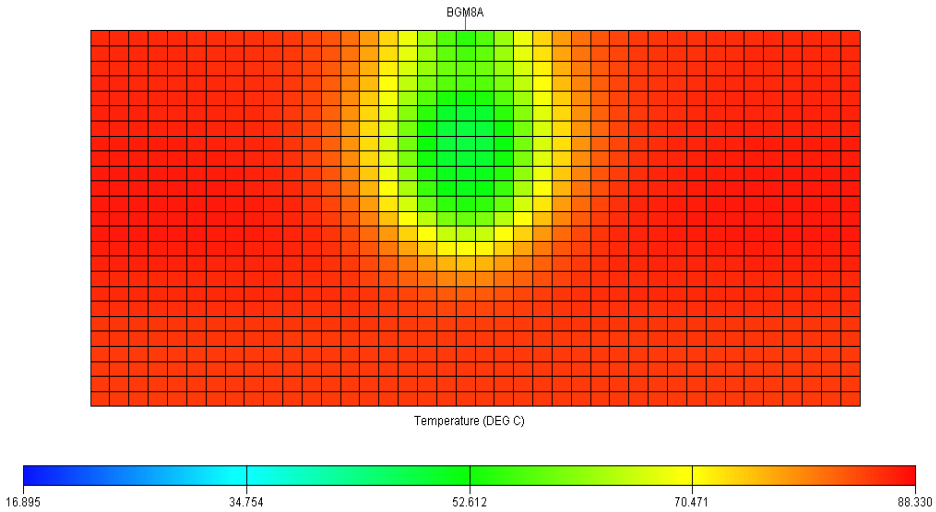

Figure 5.5: Cross section of the single well model with a small grid block size: length=width=10m and height=10 m.

5.5 Data transfer to the geomechanical study

Data from Petrel and results from the Eclipse 300 simulation are transferred to the geomechanical modeling software. Grid geometry is transferred using a GRDECL formatted file generated by Petrel. Grid block properties and time dependent grid block pressures and temperatures are transferred using simple ASCII files generated by Petrel after being read by Petrel from Eclipse generated files.

5.6 Conclusions and recommendations

5.6.1 Conclusions

1. The temperature distribution in the field after injection of 9 Bsm^3 cold cushion and working gas and one production phase shows a temperature decline localized around the wells: some 40 ^oC within 50 m and less than 20 ^oC at 100 m. The temperature of the rest of the field remains largely unaffected.
2. The first two years of injection are most important. After two years injection gas needs to be compressed and BHT rises to 60-66 ^oC. Hence, the difference between initial reservoir temperature of 89 ^oC and the injection gas temperature becomes smaller and hence the effect of colder gas injection is much less. In addition, gas production results in gas with initial reservoir temperature flowing to cool down areas, heating them again.
3. Use of a grid block size of 100 m laterally is sufficiently detailed, except possibly for wells close (<150m) to faults.

5.6.2 Recommendations

1. For the thermodynamic properties of the rock standard data are used. Actual data may deviate. The temperature distribution is mainly sensitive to rock heat capacity of the reservoir. A reduction of the reservoir rock heat capacity by 20% will increase the radius of the temperature drop by some 12%. Hence, if well locations are changed and come closer than 150 m from faults, it is advised to investigate the sensitivity of the temperature distribution to rock heat capacity.
2. As the major effect of gas injection and production is during cushion gas injection and the first injection/production cycle, only these periods have been modeled. During these phases, temperature effects remain limited to some 100 m around wells. If wells are located closer than 150 m to faults, it is advised to model at least five full injection/production cycles to access the longer term temperature distribution.
3. In the full model, the grid block dimension may be too large to accurate model the temperature distribution for wells close to faults. It is advised to further investigate this if wells are located closer to faults.
4. It is advised to monitor field performance, particularly well temperatures and pressures, and compare the measurements to the simulated model results.

6 Geomechanical analysis

6.1 Introduction

In the geomechanical analysis the impact of gas storage on seismic hazard in the Bergermeer gas field is investigated. The Bergermeer gas field has been seismically active since 1994. Four seismic events in total were recorded in the Bergermeer field since 1994, ranging in magnitude from 3.0 to 3.5 on the Richter scale. According to studies of KNMI, the hypocenters of the events are located at the tip of a normal fault intersecting the Bergermeer field, at depths corresponding to reservoir level (2.0-2.5 km depth). However, due to uncertainties in the determination of the hypocentre location, it remains feasible that the events occurred on one of the bounding faults or even on one of the many listric overburden faults. Considering tectonic earthquakes, this part of the Netherlands is considered as a low seismicity area (De Crook et al, 1996). The earthquakes are generally assumed to be the result of reactivation of faults in the subsurface due to gas extraction (Begeleidingscommissie Onderzoek Aardbevingen, 1993). Faults can generally be considered as weak planes or weak zones in the reservoir rocks, and deformations caused by the extraction (or injection) of gas in the reservoir will be largely accommodated on fault planes or within fault zones.

This study explores the effect of gas storage (injection and production of gas) on the stress state and deformations in and around the Bergermeer field. The study largely aims at demonstrating the effects of injection, production and temperature changes on the stability of existing faults and the related possibility of seismic hazards.

6.2 Methodology

A geomechanical finite element model has been developed in order to study the effect of past depletion of the reservoir and future injection and production of gas on reactivation and slip of existing nearby faults.

A cross section for geomechanical modeling was selected from the geological model in Petrel, which formed the basis for the construction of a two dimensional geomechanical finite element model in DIANA. This finite element geomechanical model is used to compute the stress and deformation fields, given the pressure and temperature distribution from the reservoir modelling in Eclipse for the phase of reservoir depletion and the defined injection and production scenario.

The flow model (Eclipse) and geomechanical model (DIANA) are one-way coupled. The Eclipse model is used to calculate the pressures and temperatures for the complete depletion history (1971-2006), the in-between period of no activity (2006-2010), the period of cushion gas injection (2010-2012) and for one injection/production cycle (2013). The time history for both pressures and temperatures is then used in DIANA to model stress changes and the associated deformations. In order to achieve compatibility between the Eclipse model and DIANA model, the three dimensional gridblock volume structure of the Eclipse model is ‘mapped’ on the two dimensional finite element mesh of DIANA.

Input parameters are largely uncertain and the geomechanical model is run with a number of scenarios in which the initial stress conditions and the key geomechanical parameters are varied. Based on history matching of the modelled response of these scenarios during depletion against recorded seismic events and the results of a minifrac test used for estimating the minimum in situ stress, a number of scenarios is selected for further calculations.

6.3 Stress and deformation modelling of reservoir depletion and injection/production

6.3.1 Background

The initial state of stress in the subsurface is determined by a stress tensor, defined by three principal components (principal stresses) and its three direction cosines. In geological applications one of the principal stresses is assumed to be vertical. In an extensional stress regime (i.e. a normal-faulting regime), as it is the case in the Netherlands, the vertical stress represents the major principal stress. The total vertical stress at depth can be calculated from the weight of the overlying sediments. For saturated sediments, the total vertical stress can be calculated from:

$$\sigma_v = \int_z^0 \rho(z) g dz$$

In which σ_v is the total vertical stress [$ML^{-1}T^2$, i.e. MPa], g is the gravity acceleration [LT^{-2}, ie m/s^2], z is the depth (L, i.e. m) and $\rho(z)$ [ML^{-3}, i.e. kg/m^3] is the rock density as a function of depth.

The other two principal stresses, which are assumed to be horizontal, are more difficult to determine. By means of minifrac tests or extended leak off tests (XLOT), the minimum horizontal stress can be determined (σ_{hmin}). Maximum horizontal stress determination is difficult, as there are no reliable techniques to determine the maximum horizontal stress in the field. In case field tests are not available, regional stress maps can give useful information on the stress field. In this project, the analysis is performed in 2D on a vertical cross-section oriented perpendicular to the maximum horizontal stresss (see Section 6.4 for detailed explanation of the modelling plane orientation).

Using density logs from the Bergermeer field, a lithostatic total vertical stress gradient of 22.6 MPa/km is derived for total vertical stress σ_v. It is assumed that the Bergermeer field is situated in a regional extensional stress regime, which implies that both horizontal stresses are lower than the vertical stresses. The initial direction of the minimum horizontal stress is assumed to be oriented NE-SW, perpendicular to the strike of the main faults in the area. This assumption is consistent with the directions given on the World Stress Map (http//:world-stress-map.org) and break out analysis of core samples in the north of The Netherlands (Rondeel, 1993). No XLOT or microfrac tests are available from the period before the start of depletion. For modelling, the estimate of the total minimum horizontal stress σ_{hmin} of both overburden and reservoir rocks is based on the values reported in the technical note of SENERGY (March, 2008). Reported values are based on field tests, such as Leak Off Tests (LOT), Formation Integrity tests (FIT) and a water injection tests in BGM #4, and values reported for the North Sea area in general. A total stress ratio $K_0 = 0.65$ is reported, with:

$$K_0 = \frac{\sigma_{h\min}}{\sigma_v}$$

Stresses considered above are total stresses. According to the theory of stress separation, based on the Terzaghi's principle of effective stress, the total stress can be separated into the effective stress (intergranular stress) and the pore pressure:

$$\sigma' = \sigma - Ip$$

In which σ' is effective stress ($ML^{-1}T^2$, i.e. MPa), σ is total stress, p is pore pressure ($ML^{-1}T^{2,}$ i.e. MPa) and I is unit tensor.

The above relation can be extended by Biot's theory of poro-elasticity, including the compressibility of the rock mass:

$$\sigma' = \sigma - \alpha Ip$$

In which :

$$\alpha = 1 - \frac{K_D}{K_s}$$

In which: α is the Biot factor (-) and K_D ($ML^{-1}T^2$, i.e. MPa) and K_s ($ML^{-1}T^2$, i.e. MPa) are the compression modulus of the drained porous soil/rock matrix, resp. the non-porous solid.

The basic principle of the stress separation theory is that a change in effective stress causes all deformation of the rock (i.e. distortion, compaction) and effective stress rather than the total stress determines whether a rock deforms and fails.

Taking into account the pore pressures in the overburden rock and pore pressures at reservoir level, an effective horizontal to vertical stress ratio of approximately K'_0=0.36 is obtained for both the overburden and reservoir rocks. In which:

$$K_0' = \frac{\sigma'_{h\min}}{\sigma'_v}$$

Pore pressure changes induced by the depletion of the reservoir and the injection/production of gas from the reservoir alter the effective stresses in the subsurface. Also, cold gas injected into the reservoir locally reduces the temperature of the reservoir. Temperature changes have an impact on effective stresses in the reservoir. In the next paragraph the possible effects of changes in pore pressure and temperature on the stability of a faulted reservoir are described, using basic thermo-poro-elastic solutions for a homogeneous reservoir and frictional fault theory.

6.3.2 Basic analysis thermo-poro-elasticity and frictional fault theory

The change in horizontal and vertical effective stress in the reservoir during depletion and injection is related to the pore pressure change Δp and the change in total stress Δσ (first isothermal conditions are assumed):

$$\Delta\sigma'_v = \Delta\sigma_v - \alpha\Delta p$$

$$\Delta\sigma'_h = \Delta\sigma_h - \alpha\Delta p$$

The relation between the change in total stress and pore pressure change can be expressed by the ratio γ_v (vertical arching constant) and γ_h (horizontal arching constant):

$$\gamma_v = \Delta\sigma_v / \Delta p$$

$$\gamma_h = \Delta\sigma_h / \Delta p$$

In a horizontal reservoir with infinite lateral extension during depletion and injection the total vertical stress is constant, which means $\Delta\sigma_v=0$, $\Delta\sigma'_v=-\alpha\Delta p$ and $\gamma_v=0$. The ratio γ_h for horizontal stress equals:

$$\gamma_h = \alpha(\frac{1-2\nu}{1-\nu})$$

The change in horizontal stress then equals:

$$\Delta\sigma_h = \alpha(\frac{1-2\nu}{1-\nu})\Delta p$$

In which ν is the Poisson's ratio (-),

and

$$\Delta\sigma'_h = -(\alpha - \gamma_h)\Delta p \qquad (3)$$

For values of the Poisson's ratio of $\nu < 0.5$ the increase in the vertical effective stress (during depletion) is generally higher than that in the horizontal effective stress, so a differential stress development takes place, which can cause the reactivation of faults.

In case of both changes in pressure and temperature, the change in total horizontal stress in the infinite reservoir equals:

$$\Delta\sigma_h = \frac{1-2\nu}{1-\nu}\{(\alpha\Delta p) + (K\alpha_s\Delta T)\} \qquad (4)$$

In which K is the bulk modulus of rock, α_s is the volumetric thermal expansion coefficient (-) and ΔT is the change in temperature (°C).

The initial state of stress in a reservoir can be represented (in 2D) by a Mohr circle, defined by the smallest and largest principle effective stresses in the subsurface (σ'_{hmin} and σ'_v), see Figure 6.1. The initial state of stress on a fault plane in a reservoir can be determined by the normal effective stress σ'_n and shear stress τ (Figure 6.2), which can also be found using the same Mohr circle. In the plot also the Mohr Coulomb failure line is given:

$$\tau = c + \sigma'_n \tan\varphi$$

With c: cohesion of the fault (MPa) and φ friction angle of the fault (°).

Depending on both parameters of the faults and the reservoir rock, the differential stress development, which takes place due to changes in pore pressure and temperature, may be critical or non-critical, as the stress path approaches the critical Mohr Coulomb failure line (Figure 6.3) or diverges from the critical Mohr Coulomb failure line. Isothermal injection into a depleted reservoir will result in a stress path with a reversed sense, parallel with the stress path for depletion. In case of only elastic deformation and constant temperatures, the stress path for depletion and injection will overlap. In case of non-isothermal injection however, the stress path will often differ from the isothermal stress path.

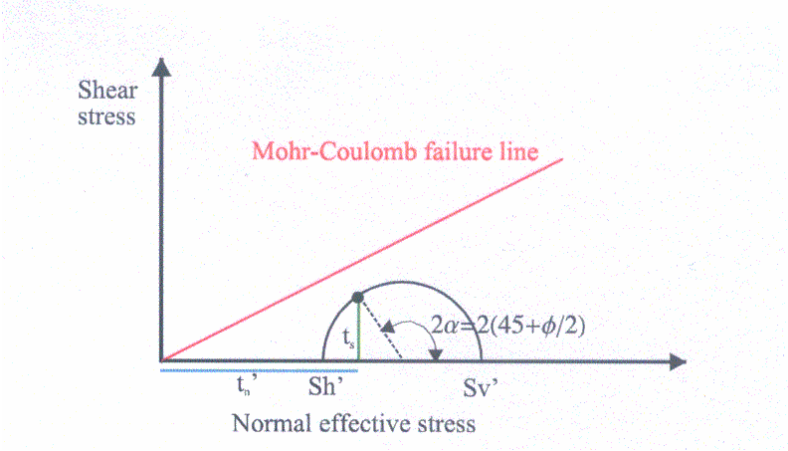

Figure 6.1: Initial state of stress in the subsurface and on the fault plane, resolved by the Mohr circles.

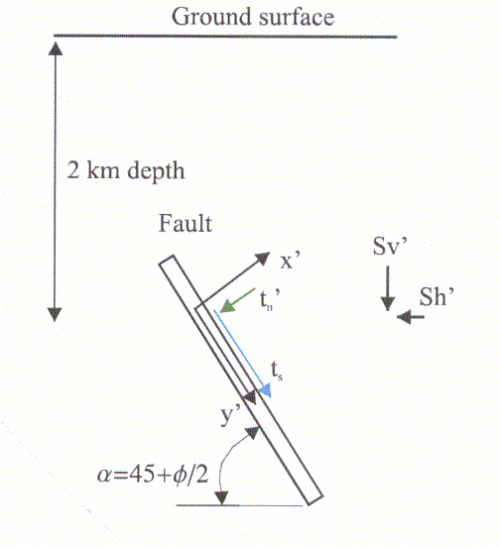

Figure 6.2: Stresses in the subsurface and tractions on the fault plane.

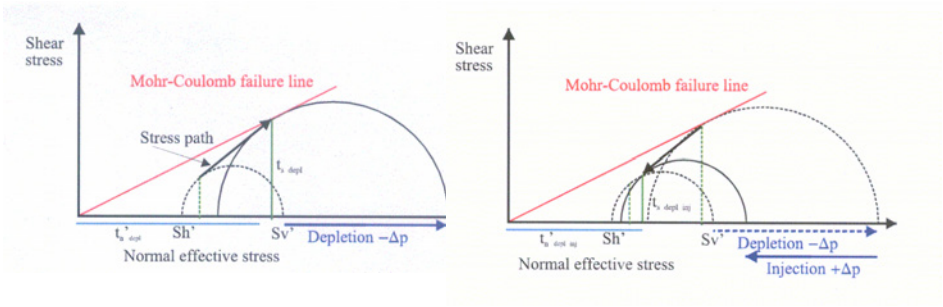

Figure 6.3: Left: Critical development of the stress path for depletion. Right: Non-critical development of the stress path for injection in a depleted reservoir.

A stress path which during depletion converges on the Mohr Coulomb failure line leads to a less stable stress state during depletion; the stress state will stabilize during injection (see Figure 6.3). A diverging stress path during depletion means conditions are stabilizing during depletion, but will be less stable during injection. Several critical geomechanical parameters of both reservoir rock and the faults determine whether depletion or injection lead to a more or less stable stress state (Biot factor α, Poisson 's ratio ν, Young's modulus E, thermal expansion coefficient α_s, and cohesion c and friction angle φ).

Whether reactivation of the faults and fault slip will occur also depends on the position of the initial stress state relative to the failure line and the actual pressure and temperature change. Changes in pore pressure, temperature and stress that are destabilizing will not cause fault reactivation if the initial stresses are sufficiently far from the failure line.

For the Bergermeer Field calculations based on the poro-elastic equations can give insight in the effects of depletion and injection on stress changes and potential for fault reactivation. For the calculation stress results of the minifrac test in BGM#8 are used. From the minifrac test, performed at a depth of about 2125m, a value of σ_{hmin} = 15MPa was obtained for the total minimum horizontal stress in the top of the reservoir after depletion of the reservoir.

At a depth of 2125m (depth of minifrac test BGM#8) a stress gradient of 22.6 MPa/km gives a total vertical stress of 48MPa. Pore pressures at the start of depletion in 1971 are approximately 23 MPa. During depletion pore pressures are decreased to a minimum of 1 MPa. During injection pore pressures are increased to a maximum of 13MPa. Using the effective stress ratio K'_0=0.36 stress values are obtained for the reservoir before depletion (Table 6-1).

Suppose the Bergermeer field is a laterally extended infinite reservoir. The change in total vertical stress is then $\Delta\sigma_v$=0. Using equation (3) the change in total horizontal stress can be calculated. Using average values for Poisson's ratio (ν=0.18) and Biot factor (α=0.76) given in Logan (1997) for the reservoir rocks, a γ_h=0.6 is calculated and total and effective stresses after depletion can be determined. Results from the minifrac test and the above calculations however suggest that γ_h should be higher than 0.6, i.e. γ_h =0.77.

Table 6-1: Stress values and pore pressures before and after depletion.

	Before depletion In-situ stress (MPa)	After depletion (MPa) γ_h=0.6	After depletion (MPa) γ_h=0.77	After injection (MPa) γ_h=0.77
Total vertical stress (σ_v)	48	48	48	48
Effective vertical stress (σ'_v)	25	47	47	35
Total horizontal stress (σ_{hmin})	32	18.8	15	24.3
Effective horizontal stress (σ'_{hmin})	9	17.8	14	11.3
Pressures	23	1	1	13

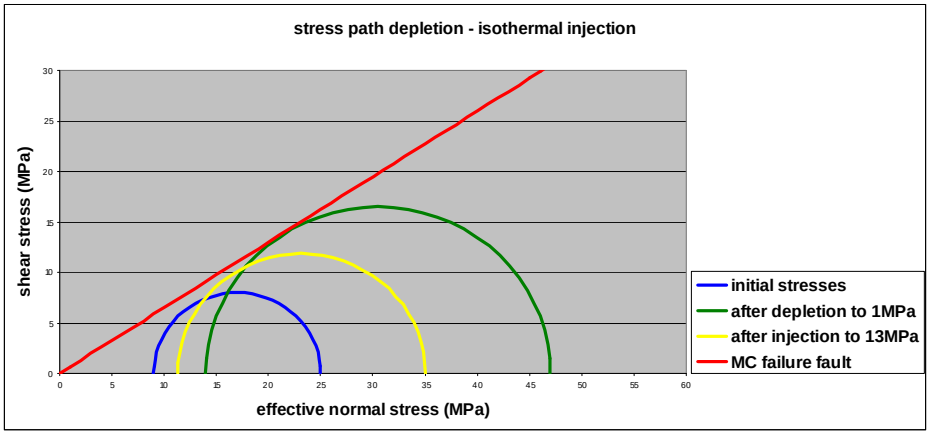

Figure 6.4: Stress changes in the reservoir during depletion and *isothermal* injection (friction angle of fault 33°).

Stresses after depletion and injection are plotted in a Mohr Coulomb plot in Figure 6.4. Also a Mohr Coulomb failure line for a fault with friction angle of φ=33° is plotted. The plot shows that the Mohr circle of initial stresses lies close to the Mohr Coulomb failure envelope. During depletion the Mohr circle grows and reaches the failure envelope, which means that a slip occurs on a fault with a critical orientation. During injection the Mohr circle decreases and stresses diverge from failure conditions, which means (under the assumptions of a laterally extended reservoir) *isothermal* injection leads to more stable conditions in the reservoir.

The above calculations show the effect of depletion and *isothermal* injection on stress changes and fault stability in a laterally extended infinite and homogeneous reservoir. In theory, equation 4 can be used to determine the effect of non-isothermal injection on stress changes and fault stability, in case temperature changes are distributed uniformly in the reservoir. Reservoir modelling results indicate that the spatial distribution of temperatures during injection is non-uniform, with a high temperature gradient near the injection wells. Furthermore, in a laterally extended infinite reservoir no lateral strains occur during pressure changes and total vertical stresses are constant. In reality, the dimensions of the reservoir are limited and the reservoir is intersected by several faults. Differential movements during depletion and injection in reservoir compartments on

both sides of the faults may cause relative shear displacement along the faults. In order to take both the effect of (finite) reservoir geometry and the localised temperature decrease during injection and production into account, a geomechanical finite element model is constructed. This finite element geomechanical model is used to compute the stress and deformation fields, given the pressure and temperature changes from the reservoir modelling in Eclipse for the defined gas injection and production scenarios. The finite element model is described in the next paragraph.

6.3.3 Direct injection into faultzones

The effect of pore pressure increase on fault stability and stress paths differs from the poro-elastic response described above if direct injection into an (impermeable) fault(zone) takes place. In case of direct injection into a fault the normal stress on the fault plane decreases by the same amount as the change in pore pressure. This means the Mohr circle shifts horizontally towards the Mohr Coulomb failure line (see Figure 6.5). In order to prevent direct injection of gas into the fault(zones) no injection wells should be planned within a distance of 150m of the known faults[17].

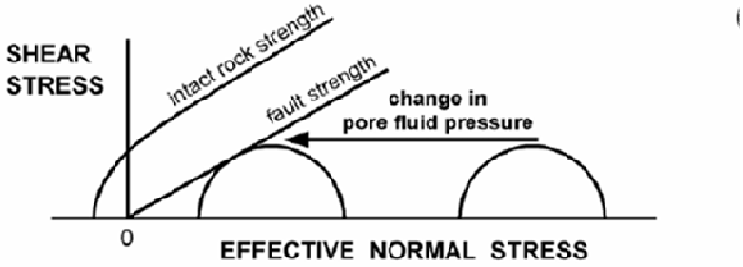

Figure 6.5: Direct injection into a fault zone: Effect of pore pressure increase on stress state and fault stability.

6.4 Finite Element Model

Finite element modeling is performed in DIANA. For the construction of the geomechanical model, a 2D cross section was selected from the geological model in Petrel (see chapter 3).

The Bergermeer Field is characterized by the presence of a reservoir rock cut by a number of NW-SE and NE-SW striking normal faults. The throw of the NW-SE striking faults varies along the strike of the faults. Several normal and listric faults exist within the overburden above the Zechstein salts. From the 3D Petrel model a critical 2D cross section was chosen to model the stresses and deformations during depletion, injection and production. The chosen DIANA cross section is oriented perpendicular to the NW-SE trending fault planes, which means the two principal stresses σ_v and σ_{hmin} are oriented parallel to the cross section and one principal stress σ_{hmax} is oriented perpendicular to the cross section. The 2D cross section is located near the tip of the central NW-SE trending normal fault , and crosses the area of the epicentres of former earthquakes. Reasons for choosing this specific location of the cross sections are:

[17] Taking into account a maximum width of a fault zone (100m on both sides) and the uncertainty of the location of the faults due to the limited resolution of the seismics (50m)

- The cross section intersects the area of the four former earthquakes which occurred during depletion of the reservoir. In this area seismic slip occurred on one of the fault planes, which means stress conditions after depletion on (one of the) faults are at or near Mohr Coulomb failure conditions. Small changes in stresses may possibly lead to fault slip.
- In the cross section the throw on the central normal fault of the reservoir is about half the height of the reservoir. Here on both sides of the fault reservoir rocks are present (overlap). At this specific structural geological setting large relative shear displacements can occur on the central fault during depletion of the reservoir (Roest & Mulders, 2000, Mulders, 2003). Again, it is a likely configuration for the occurrence of fault slip during depletion, which means stress conditions after depletion on the central normal fault may be at or near the Mohr Coulomb failure conditions.
- The location of the cross section is chosen close to an injection well. Here close to the fault (about 200m) a decrease in temperature from 84°C at the start of injection to 68°C during the injection cycle is predicted. A decrease in temperature during injection may lead to fault slip (paragraph 6.3.2 and Logan, 1997).
- Seismic slip on faults with contacts of Zechstein (rocksalts) and reservoir rocks on the opposite sides of the fault plane seems less likely. A cross section on which reservoir rocks on both sides of the central fault overlap is chosen.

Figure 6.6 gives the geology and the location of the cross section. The geometry of the model has been simplified and the deposits were grouped into a limited number of geomechanical units (Table 6-2).

Figure 6.7 shows the DIANA model.

Eight faults were incorporated in the model. Three normal faults run partially through the reservoir (faults nr. 3, 4 and 5) and base rocks, two normal faults cut both Rotliegend and base rock but are located further from the Bergermeer field (faults nr. 1 and 2). Three normal faults cut the overburden rocks (faults nr. 6, 7 and 8). Fault nr. 7 is a listric fault which ends in the Zechstein unit.

The dimensions of the DIANA model are 8.5 x 4 km. The total number of elements in the model is about 15000. Quadratic triangular and quadrilateral plane strain elements were used to model the geomechanical units (CT12E and CQ16E element type). Faults are modelled by 1-m thick interface elements (Cl12I element type).

6.4.1 Material models and geomechanical parameters

An overview of the geomechanical parameters used to characterize the geomechanical units is presented in Table 6-3. Material properties for the geomechanical units are obtained from the Bergermeer well logs, general literature and Logan's (1997) report.

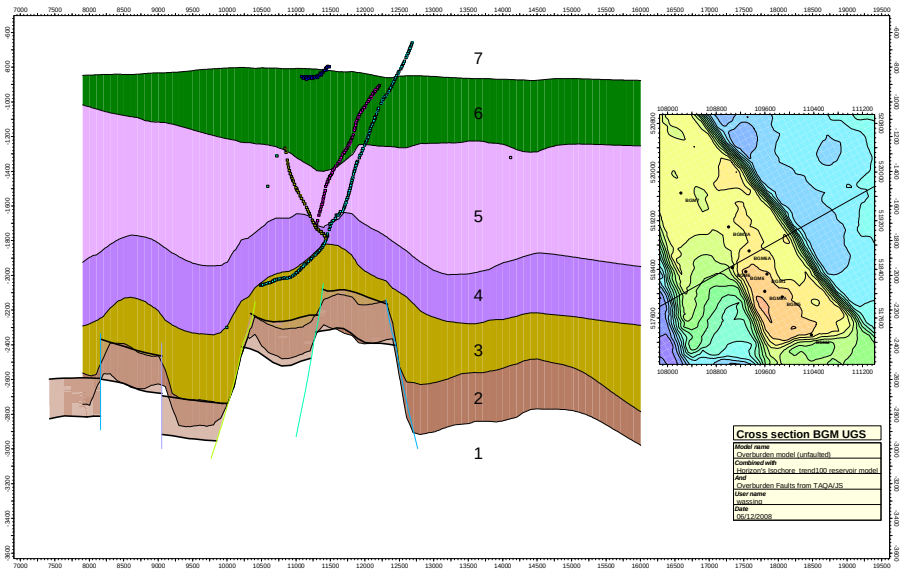

Figure 6.6 Geology and location of cross-section for DIANA model.

Table 6-2: Defined geomechanical units.

Geomechanical unit	Geological units
1 Base rocks	Carboniferous
2 Reservoir rocks	Rotliegend Slochteren sandstone
3 Zechstein	Zechstein Formation
4 Overburden 1	Main Claystone
5 Overburden 2	Musschelkalk, Bunter & Keuper
6 Overburden 3	Vlieland Shales & Holland Marls
7 Overburden 4	Tertiairy rocks

6.4.1.1 Geomechanical units

The Young's modulus and Poisson's ratio for the Rotliegend reservoir sandstone are based on the average values given by Logan (Logan, 1997). Comparison of the stress path and stresses in the model and the stress path and horizontal stresses obtained from the minifrac test (BGM8) indicates that an average Poisson's ratio of ν=0.18 results in too high horizontal stresses (γ_h=0.77 is obtained from the minifrac test). A lower Poisson's ratio of ν=0.11 results in γ_h=0.77, therefore calculations are also performed for ν=0.11. This value is still within the range mentioned by Logan (1997) and Zoback, (2007).

Young's moduli for Zechstein and overburden rocks are obtained from literature (Roest & Kuilman, 1994) and the sonic (V_p) and density logs in the Bergermeer wells (see paragraph 4.3.1).

Poisson ratio's for Carboniferous, Zechstein and overburden are obtained from literature (Logan, 1997, Roest & Kuilman, 1994; Evaluation of geomechanical parameters obtained from licensing plans).

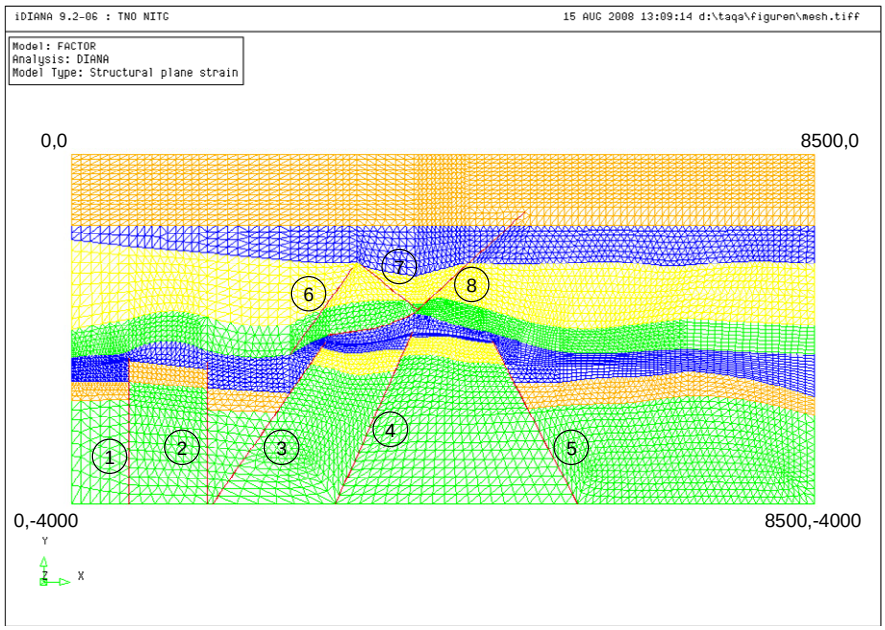

Figure 6.7: DIANA mesh. Faults are indicated in red and numbered for reference.

Table 6-3: Geomechanical parameters for the geomechanical units.

Unit	Density (g/cm^3)	Youngs modulus (GPa)	Poisson ratio (-)	φ (°)	c (MPa)	K'_0 (-)	α_s (-)
1	2.6	30	0.25	35	5	0.4	
2	2.6	18	*Min: 0.11* Max: 0.18	35	5	0.36	3.0e-*5*
3	2.1	Min: 20 *Average: 35* Max: 50 creep law	0.3	35	5	1.0	
4	2.6	25	0.25	25	5	0.36	
5	2.6	20	0.25	25	5	0.36	
6	2.3	10	0.25	25	3	0.36	
7	2.3	.5	0.3	25	.5	0.36	

The thermal expansion coefficient α_s for the Rotliegend sandstone is based on literature values (Zoback, 2007).

The elasto-plastic Mohr-Coulomb material model was used to model the mechanical behaviour of the geomechanical units, except the Zechstein unit. For the Zechstein unit two types of constitutive models are used: an elasto-plastic Mohr-Coulomb (no time dependent deformation) and a creep law to model the time dependent creep component in the Zechstein rocksalt. The two models represent two end-members for the Zechstein

unit: a Zechstein which mainly consisting of anhydrite and dolomites (elasto-plastic) and a Zechstein unit mainly consisting of rocksalts (creep model). From literature it is known that high horizontal stresses and K_0 ratios (equal or very close to one) in the rocksalt, which exist due to creep, can 'wedge' open faults at reservoir level (Roest & Kuilman, 1994).

6.4.1.2 Faults

Plastic slip on the faults is modelled using a Coulomb friction criterion (see paragraph 6.3.2), defined by a cohesion and friction angle φ. The fault planes are assumed to be cohesionless. Friction angles of the faults are varied in different calculation scenarios. Friction angles of the faults in the Rotliegend and Carboniferous units are assumed to vary between φ=28°, 32° and 35°. Friction angles of φ=25° are chosen for the faults in the overburden, with the exception of fault 6 for which φ=28° is used. Constant friction angles are used for each fault).

Both φ=28° for faults in the Rotliegend and fault 6 are lower bounds for the friction angles. In-situ stresses before depletion are constrained by the frictional strength of pre-existing faults; in-situ stresses cannot exceed the frictional strength of pre-existing, critically oriented faults (Zoback, 2007). Both faults in the Rotliegend and fault 6 in the overburden are critically oriented (fault dip close to 45°+φ/2). Hence, in situ stress conditions in both overburden and reservoir rocks can be used to determine the lower bound for the friction angle on these faults.

For normal faulting:

$$\frac{\sigma_1'}{\sigma_3'} = \frac{\sigma'_v}{\sigma'_{h\min}} \leq [(\mu^2+1)^{0.5}+\mu]^2 \qquad (5)$$

with μ=tanφ

Equation (5) gives a lower bound of φ=28° for faults in the Rotliegend and fault 6 in the overburden.

Before plastic slip occurs on the faults, elastic deformation will occur. The amount of elastic deformation is controlled by the normal stiffness D_n (GPa/m) and the shear stiffness D_s (GPa/m).
For calculation of the fault normal and shear stiffnesses the following expression has been used (Mulders, 2003):

$$D_n = \frac{(1-\nu)E}{(1+\nu)(1-2\nu)h}$$

and

$$D_s = \frac{E}{2(1+\nu)h}$$

In which ν and E are the Poisson's ratio and Young's modulus of the geomechanical unit surrounding the fault and h is the fault thickness (in meters – 1m is used for all faults, i.e. fault zones).

Fault normal stiffnesses vary between 1 and 36 GPa/m and fault shear stiffnesses vary between 0.1 and 12 GPa/m.

6.4.2 Calculation scenarios

As input parameters are uncertain, the geomechanical model is run with a number of scenarios in which key geomechanical parameters are varied. Table 6-4 summarizes the calculation scenarios that were used for modelling the response during depletion, injection and production.

Key parameters that are varied in the seven scenarios are the Poisson's ratio, (effects the arching constants of the reservoir and hence the gradients of the stress path during pore pressure and temperature changes), the stiffness ratio between top seal (Zechstein) and reservoir rock, time dependent material behaviour of the Zechstein and the friction angle of the reservoir faults. Scenario 1 is defined as reference scenario. In this scenario a minimum Poisson's ratio of 0.11 is used, an average stiffness ratio of ≈2 between top seal and reservoir rock, no time dependent creep for the Zechstein and a minimum fault friction angle of 28° for the reservoir rocks. In scenario 2 a Poisson's ratio of 0.18 for the reservoir rocks is used. In scenario 3 and 4 a minimum resp. maximum stiffness ratio between top seal and reservoir rocks is used. Scenario 5 takes into account time dependent creep in the rocksalt, and in scenario 6 and 7 fault friction angles are larger (32° and 35°).

Table 6-4: Calculation scenarios

Scenario	Overburden parameters	Faults Reservoir	E Res.	ν Reservoir	E Zechstein	α_s Reservoir	ΔT
1 – ref.	average	28°	18	0.11	35	3.0e-5	84°C →68°C
2	average	28°	18	***0.18***	35	3.0e-5	84°C →68°C
3	average	28°	18	0.11	***20***	3.0e-5	84°C →68°C
4	average	28°	18	0.11	***50***	3.0e-5	84°C →68°C
5	average	28°	18	0.11	***Creep***	3.0e-5	84°C →68°C
6	average	***32°***	18	0.11	35	3.0e-5	84°C →68°C
7	average	***35°***	18	0.11	35	3.0e-5	84°C →68°C

6.4.3 Boundary and initial conditions

Structural boundary conditions consist of imposing displacement constraints along the model boundaries. Along the lateral model boundaries displacements are allowed in vertical directions only. No vertical displacements are allowed along the bottom model boundary, while the top boundary is free to move in any direction.

The initial conditions determine the stress field at the start of the analysis, before the depletion of the Bergermeer Field commences. The initial in-situ stresses are obtained by combining:

1. Weight of the sediments.
2. A hydrostatic pore pressure in all geomechanical units except in the Zechstein and reservoir.
3. An overpressure in the reservoir. Pore pressures at the start of depletion, obtained from the Eclipse model are used.
4. The initial pore pressures on the faults are assumed to be in equilibrium with the pore pressures in the surrounding rocks. If the fault is bounded on both sides by non-reservoir rocks a hydrostatic pore pressure is assumed. If the fault is bounded on one or both sides by reservoir rocks, the fault is overpressured at the same rate as the reservoir.

The initial horizontal stress is initialized by applying the effective stress ratio K'_0. K'_0 is given in Table 6-3.

6.4.4 Modelling reservoir depletion and injection/production

The pore pressure changes in the reservoir during depletion are modelled by 1 year time steps, from 1971 (start depletion) till 2006 (end depletion). The period in between the end of depletion and start of injection is also modelled by 1 year time steps. Injection/production is modelled in smaller time steps. The injection of cushion gas and one complete injection-production cycle are modelled. Three phases of cushion gas injection are defined for pore pressures, followed by one cycle of injection of working gas and production. Time steps during injection/depletion vary between about 6 months (cushion gas) and 3 months (working gas). Pore pressures during depletion and pore pressures and temperatures during injection/production are obtained from the reservoir model. For every time step, the pore pressures and temperatures from the Eclipse reservoir grid are mapped onto the DIANA mesh. During simulation the pore pressures and temperatures in the non-reservoir units remained constant. In Figure 6.8 a graph of pore pressure and temperature versus time for the reservoir rocks near an injection well is presented.

6.5 Modelling results

The following conventions are used when presenting the results of the analyses. The global Cartesian coordinate system is used where y-axis denotes the vertical direction, x-axis horizontal direction and z-axis the out-of-plane horizontal direction.

Tensile stresses are shown as positive, compressive stresses are negative.

6.5.1 Initial stresses

The initial state of stress is presented by using colour-coded contour maps of the effective stresses and the effective stress ratio K'_0.

Figure 6.9, Figure 6.10, and Figure 6.11 show vertical effective stresses, horizontal effective stresses and K'_0 ratio in the reference case 1. The horizontal/vertical effective stress ratio for the reservoir units and overburden materials is about K'_0=0.36. Lower horizontal effective stresses exist in the overburden above the Zechstein, near the intersection of fault 7 and 8. K'_0 values in the Zechstein unit are around K'_0=1, but lower values exist close to the faults. Horizontal and vertical effective stresses and K'_0 ratios for the different scenarios are quite similar, except for scenario 5 in which a creep law for the Zechstein rocksalt is used (see Figure 6.12).

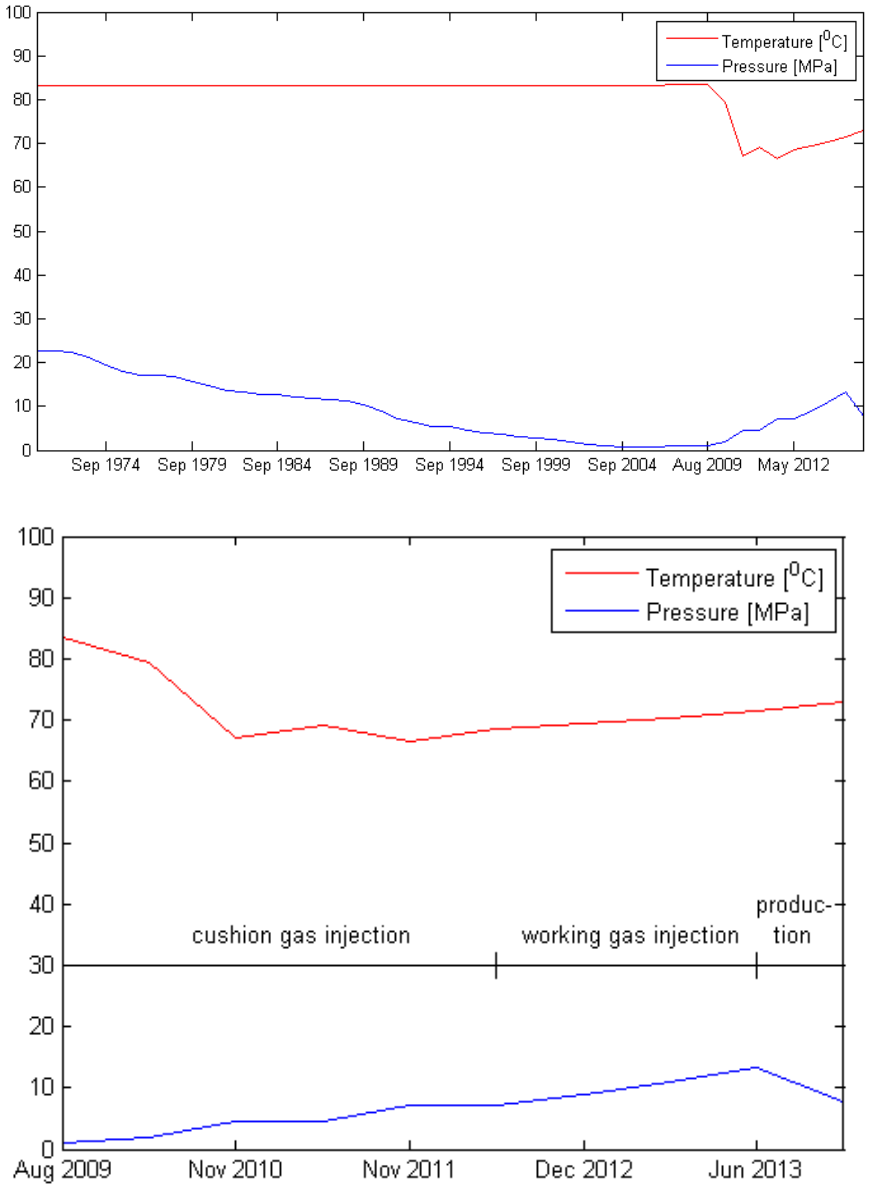

Figure 6.8: Temperature and pore pressure against time (for element close to injection well). Top figure: complete period of reservoir depletion, cushion gas injection and one cycle of working gas injection and production. Bottom: detailed profile for injection of cushion gas and working gas and production of working gas.

In scenario 5 horizontal effective stresses and K'_0 ratios in the Zechstein are generally higher than in the other scenarios. High stresses in the Zechstein result in higher horizontal effective stresses in the reservoir (higher K'_0 ratio) and underlying Carboniferous, except at those locations where faults are 'wedged open' by the high stresses in the salt (see blue colours in encircled areas in Figure 6.12).

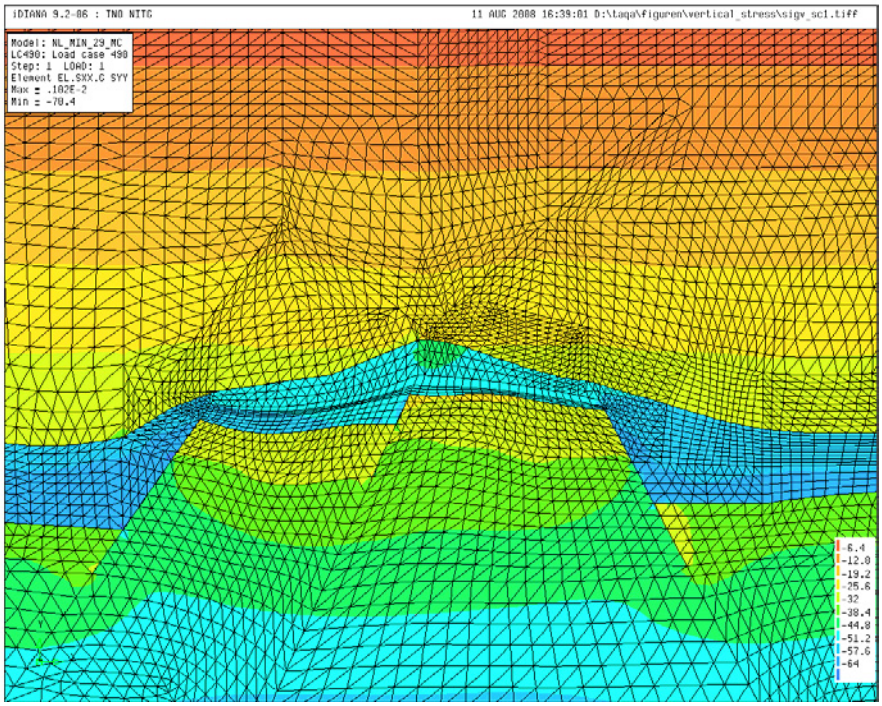

Figure 6.9: In-situ vertical effective stresses [MPa] in and around the reservoir – *reference* scenario 1.

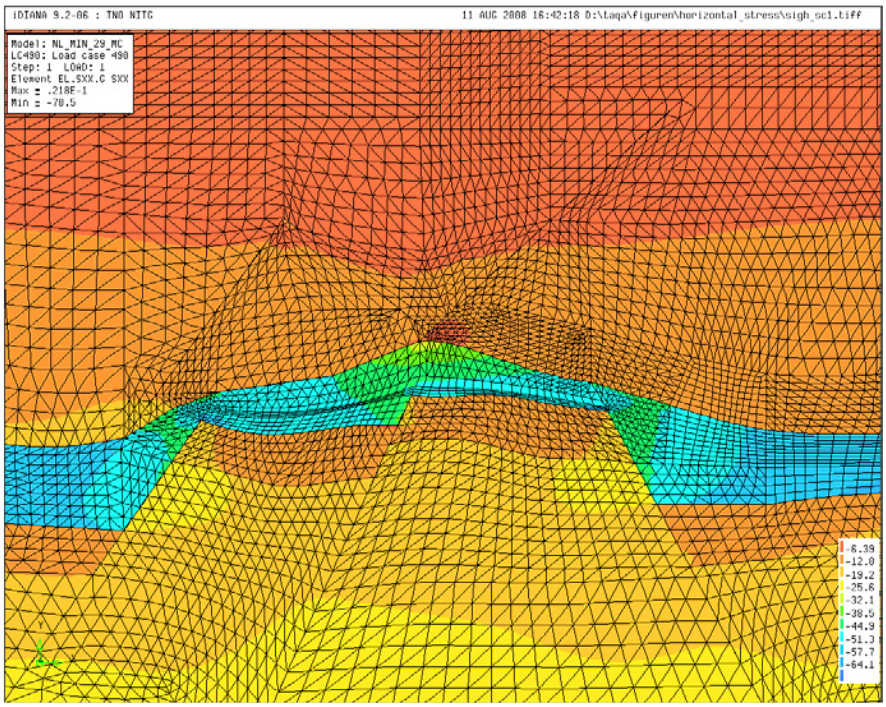

Figure 6.10: In-situ horizontal effective stresses [MPa] in and around the reservoir – *reference* scenario 1.

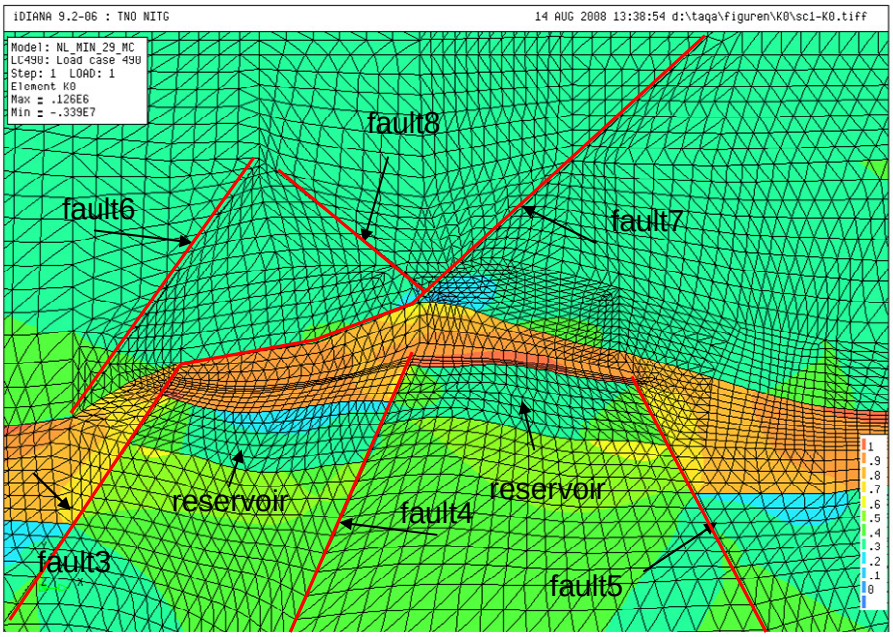

Figure 6.11: Effective stress ratio K'$_0$ [-] in and around the reservoir – *reference* scenario 1.

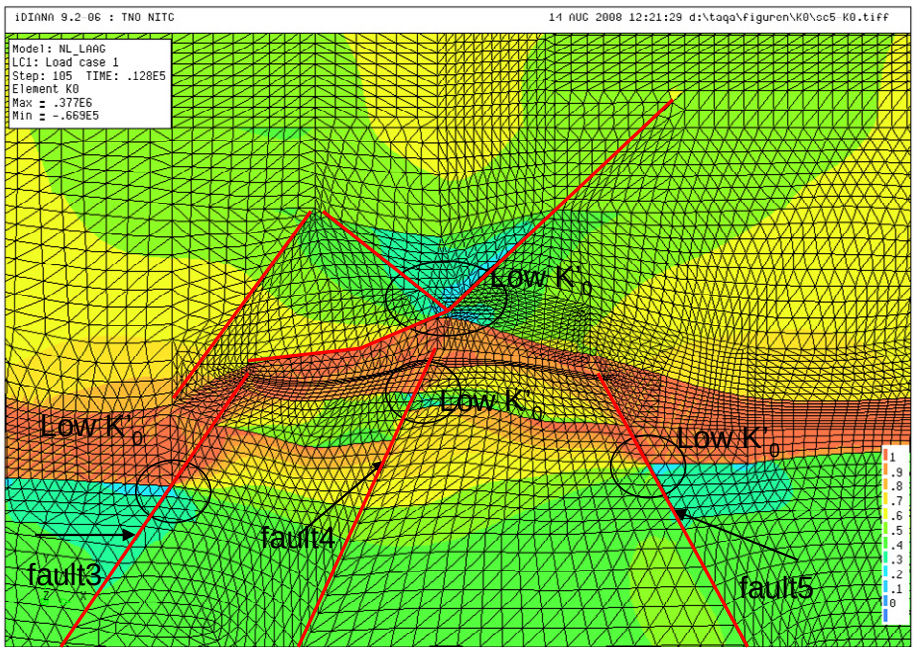

Figure 6.12: Effective stress ratio K'$_0$ [-] in and around the reservoir –scenario 5.

6.5.2 Calibration stress-path BGM#8.

For all calculation scenario's, the stress field at the start and the end of depletion is compared to the initial stresses obtained from the Synergy report and those obtained

from the minifrac test in BGM#8 at the end of reservoir depletion. For comparison, mesh-element nr. 1980 is chosen at a similar depth and distance to the central fault (4) as well BGM#8 (see Figure 6.13). For all scenarios in Figure 6.14 the modelled stress path for element 1980 is compared to the stress path in BGM#8.

In Figure 6.14 the mean and the differential effective stresses (s' and t, respectively) in 2D are used, with:

$$s' = \frac{\sigma'_1 + \sigma'_3}{2}$$

$$t = \frac{\sigma'_1 - \sigma'_3}{2}$$

For the stress path during depletion, reference scenario 1 gives the best match with the measured stress path obtained from the Synergy data and the minifrac test. Also scenarios 4 (high stiffness ratio seal and reservoir rocks), 6 and 7 (high friction angles) give good results. The stress paths for scenario 2 and 3 are not steep enough and result in too high horizontal effective stresses at the end of depletion. The stresses and stress path in scenario 5, in which a creep law for the Zechstein salt is used, differ from the results of the minifrac test. One of the reasons is the high horizontal stress and high K'_0 ratio which exist in the upper part of the reservoir at the start of depletion (see Figure 6.12*)*.

From the comparison of stress paths during depletion, it is concluded that a Poisson's ratio of ν=0.18 gives too high horizontal effective stresses at the end of depletion. A Poisson's ratio of ν=0.11 (reference scenario 1) gives results similar to the stresses obtained from the minifrac test (see Figure 6.14).

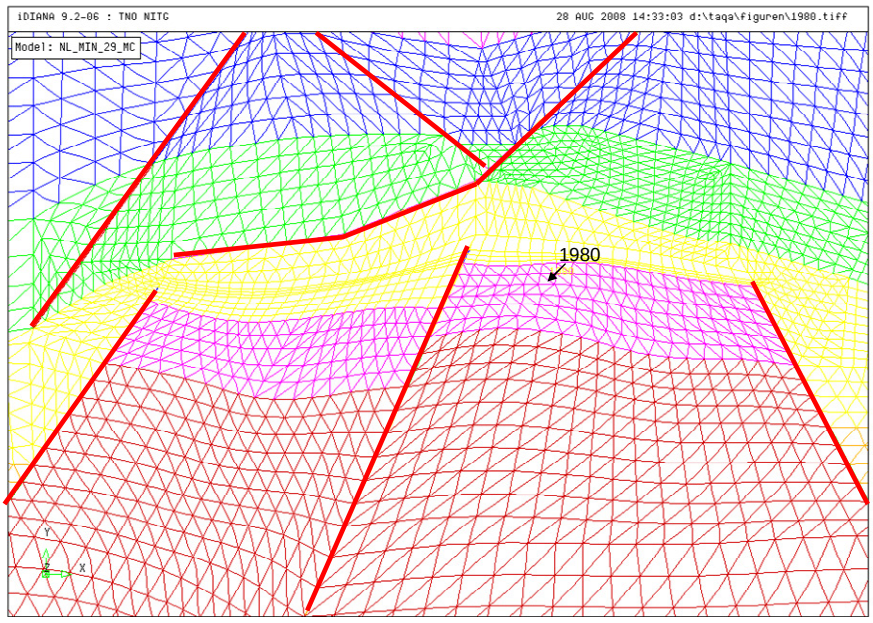

Figure 6.13: Location of element 1980 used for comparison of stress data with minifrac test in BGM#8. Faults are presented in red, reservoir rocks in pink.

6.5.3 Stress paths for faults

Changes in the stress field due to depletion and injection (taking into account both pressure and temperature loads), are analyzed by plotting normal and shear tractions on the fault planes in stress path diagrams for the faults (see paragraph 6.3.2).

By plotting the Mohr Coulomb failure line for a fault on the same diagram, it is easy to visualize whether the stress path converges to the failure line, which means the stress development becomes critical with respect to reactivation of the fault. If the stress path touches and follows the failure line, critical stress conditions have been reached and the fault is slipping. If the stress path diverges from the critical line, the stress development is non-critical.

Four seismic events took place during depletion of the Bergermeer reservoir. The first seismic event took place in 1994. This means the stress path of at least one of the faults should touch the Mohr Coulomb failure line before or in 1994. Fault slip should be enough to create a M=3.2 magnitude event. Fault slip in 2001 should be enough to create 4 seismic events of magnitudes M=3.0 to M=3.5 (see also Chapter 7). For all calculation scenario's it is checked whether the stress path intersects the Mohr Coulomb failure line before or in 1994 and what amount of relative shear displacement occurs.

6.5.3.1 Central reservoir fault 4: Stress paths and relative shear displacements

In all scenario's maximum plastic fault slip takes place during depletion of the reservoir, at the overlap of reservoir rock on both sides of fault nr. 4 (Figure 6.15). The stress path for a fault element 160 on this overlap of reservoir rock is presented in Figure 6.16. The stress path coincides with the Mohr Coulomb failure line from the start of depletion until the end of depletion, which means at present stress conditions are at or close to Mohr Coulomb failure. *During injection, the stress path moves away from the Mohr Coulomb failure line, which means this part of the fault stabilizes during injection.*

In Table 6-5 for all scenarios an overview of fault movements on fault 4 during depletion is given. A maximum normal faulting movement with a maximum displacement of 15.8 cm occurs on this part during depletion (scenario 5). Maximum displacement in the reference scenario is 13.3 cm. As expected, lower relative shear displacements are obtained when the fault shear strength is increased (scenario 6 and 7) or when the stiffness contrast between reservoir rock and overburden is decreased (scenario 3). A higher stiffness contrast (scenario 4) results in larger relative shear displacements. During injection, at the overlap a very small reverse (elastic) fault movement occurs. The stress path during production overlaps and converges to the Mohr Coulomb line, but does not reach the failure line.

For fault elements just above and below the overlap of reservoir rocks (Figure 6.17), a different stress path is found (Figure 6.18). Here, during injection the stress path moves towards and locally intersects the Mohr Coulomb failure line. However, the maximum amount of plastic slip is very small compared to the slip during depletion (4mm during injection as opposed to 13.3cm during depletion in reference scenario 1, see also Figure 6.19, Figure 6.20 and Table 6-5). A maximum fault movement during injection of 7mm is obtained in scenario 4. Fault movement during production is negligible.

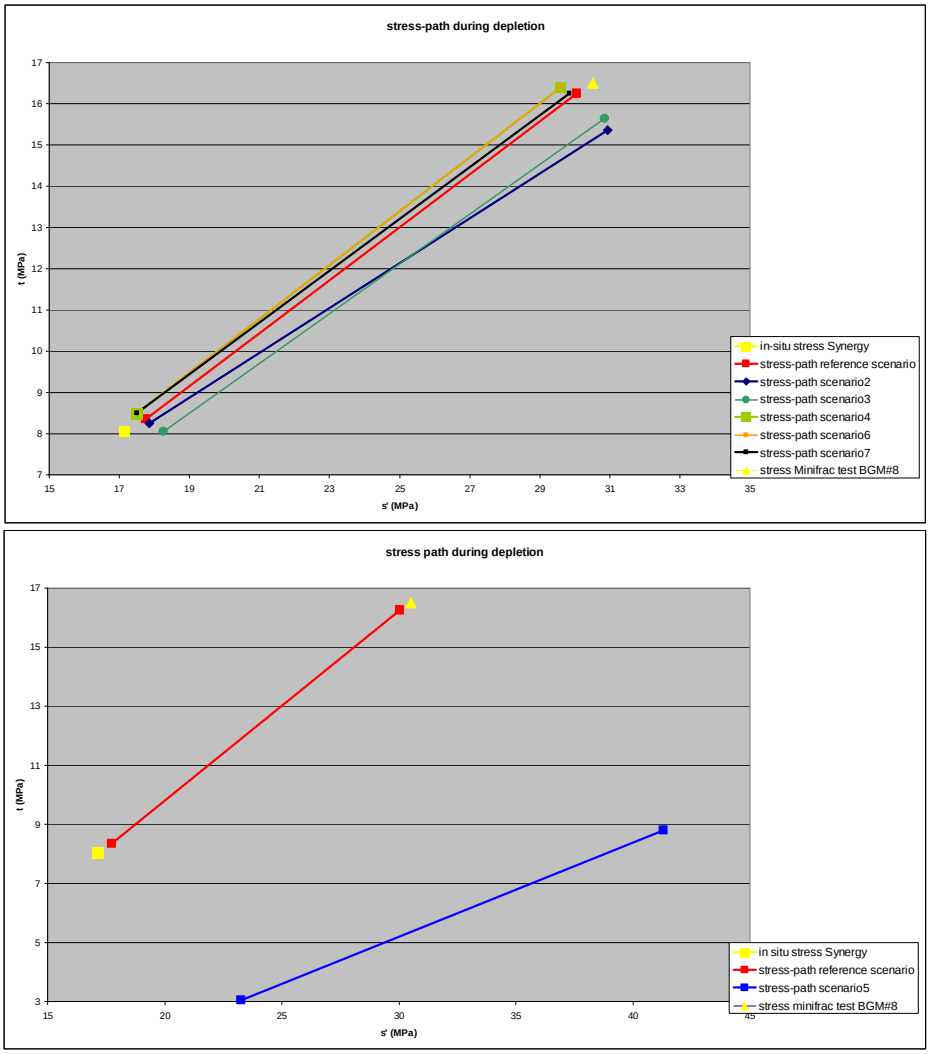

Figure 6.14: Stress-paths during depletion. Stresses at the start and end of depletion are plotted. In the top figure the stress paths for the reference scenario and scenario's 2, 3, 4, 6 and 7 are plotted (no creep). The bottom figure gives the stress path for scenario 5 (creep Zechstein).

6.5.3.2 *Bounding reservoir faults 3 and 5: Stress paths and relative shear displacements*

In all scenario's, except scenario 5, plastic slip on faults 3 and 5 during depletion is significantly smaller than on fault 4. An amount of 1.3 cm plastic slip is observed on fault 3 and fault 5 during depletion in reference scenario 1. As expected fault movements are smaller when either the shear strength of the fault is increased, or the stiffness contrast between reservoir and overburden is increased. During depletion the direction of movement on faults 3 and 5 is a normal fault movement. In scenario 5, a much larger slip of 6.7 cm and 12.1cm (normal fault movement) is observed on fault 3, resp. fault 5. This scenario gives higher fault slips along faults 3 and 5 as faults are wedged open by the high horizontal stresses in the rocksalt. During injection and production no plastic slip is observed in any of the scenarios on these faults and relative shear displacements are limited to 1 mm. Figure 6.21 and Figure 6.22 give relative shear displacements along fault 3 and 5 during depletion, injection and production.

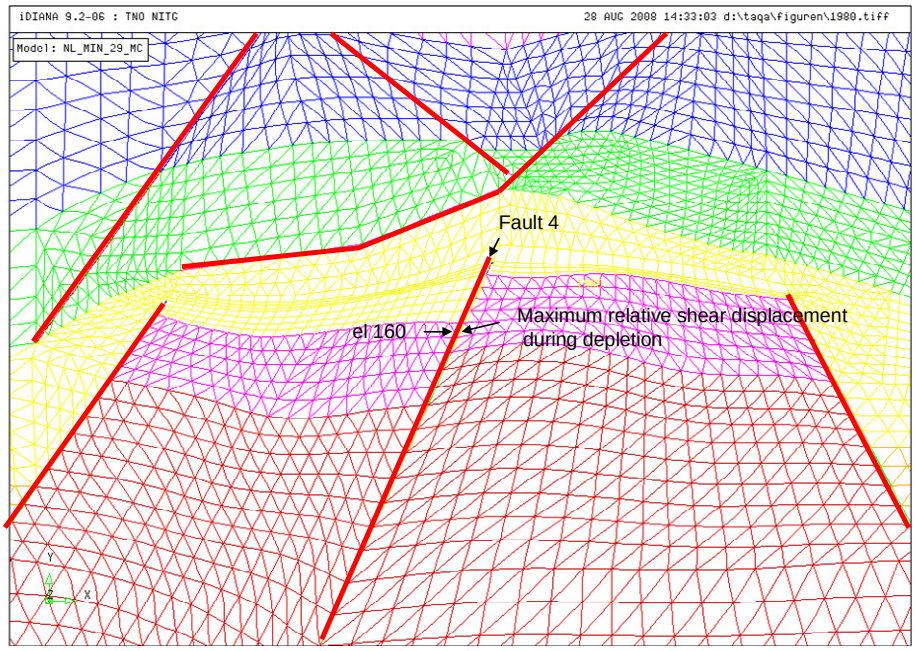

Figure 6.15: Location of maximum fault slip during depletion on central fault intersecting the reservoir. Stress path of element 160 is presented in figure. Reservoir rocks are indicated in pink colours.

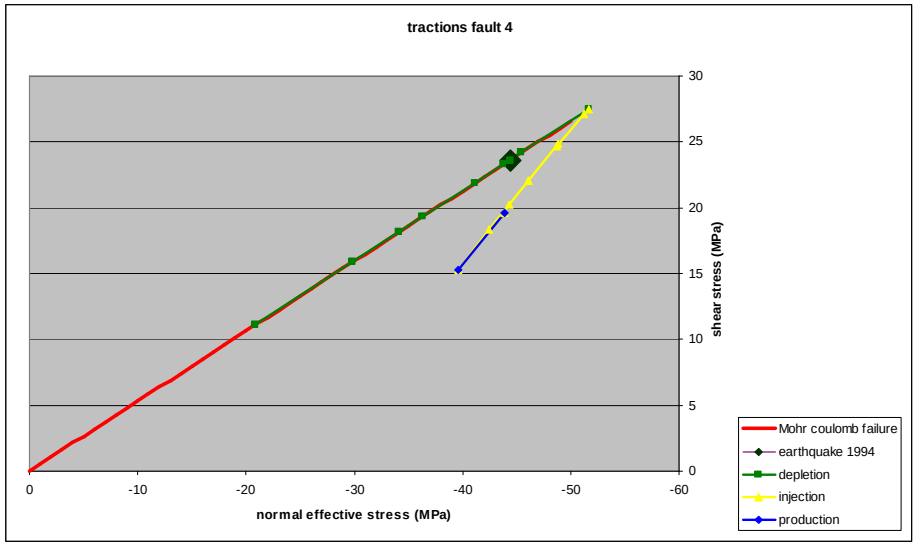

Figure 6.16: Stress path on fault4, in fault element 160 halfway the overlap of reservoir rocks. Reference scenario 1.

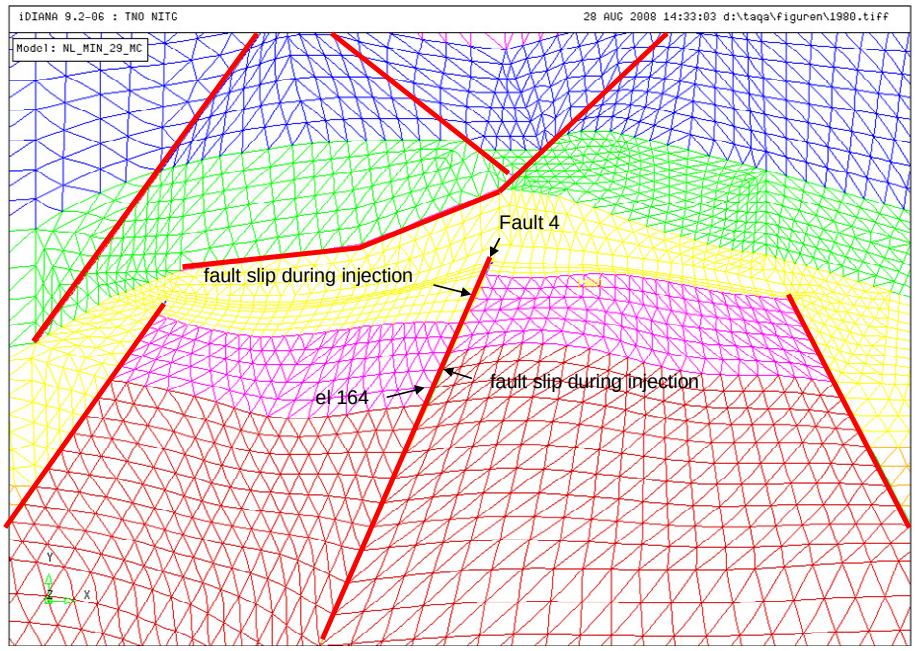

Figure 6.17: Location of maximum fault slip during injection, on central fault intersecting the reservoir. Stress path of element 164 is presented in figure. Reservoir rocks are indicated in pink colours.

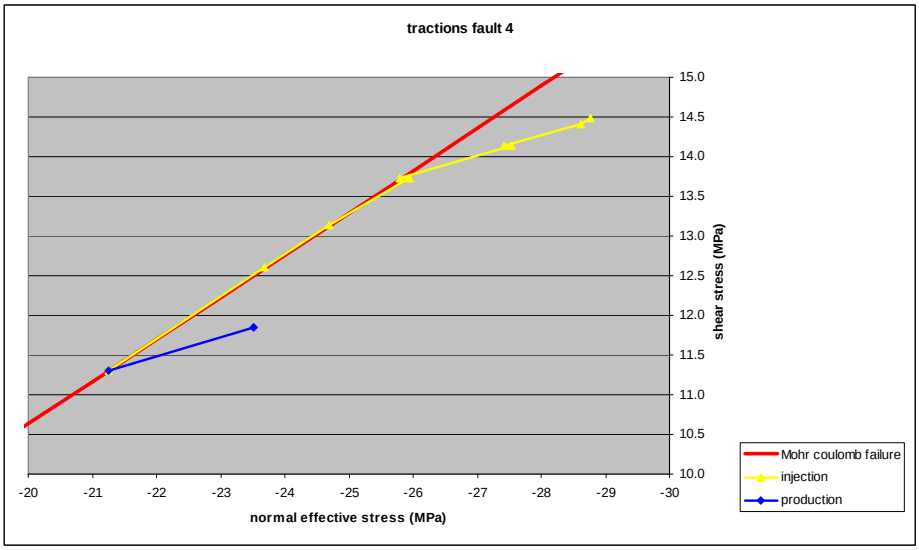

Figure 6.18: Stress path during injection and production in fault element 164 below the overlap of reservoir rock. Reference scenario 1.

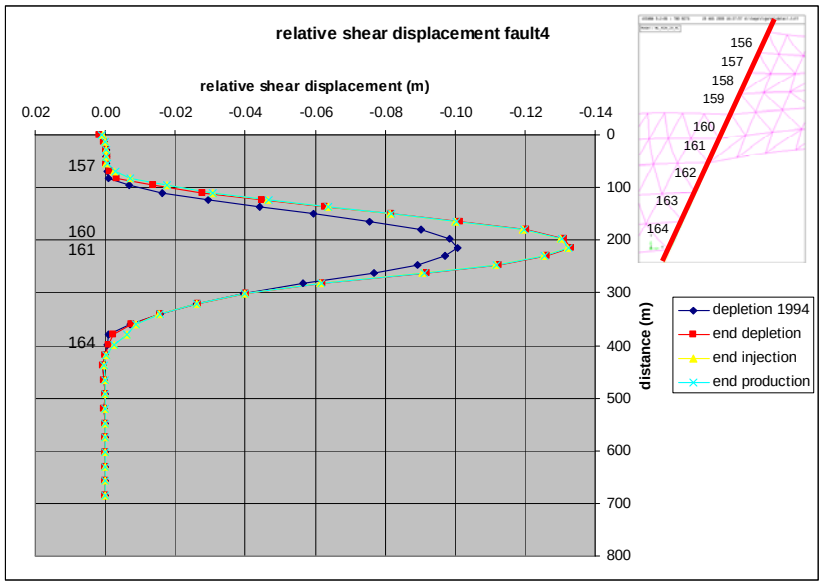

Figure 6.19: Relative shear displacement on fault4, reference scenario 1. Distance indicated on vertical axis is measured from the top of the fault. Upper right figure gives location of elements. Reservoir rocks presented in pink colours.

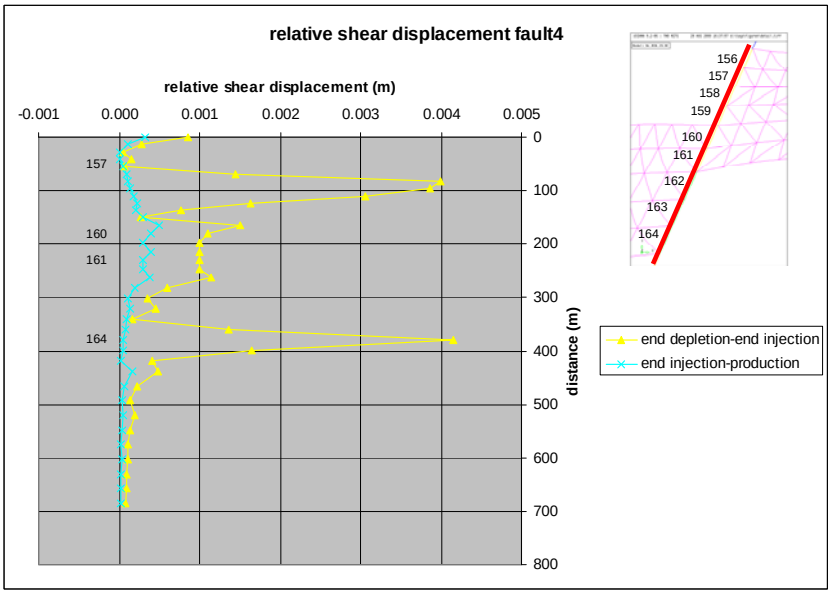

Figure 6.20: Relative shear displacement on fault 4 between a) end depletion and end injection and b) end injection and end production. Reference scenario 1. Distance indicated on vertical axis is measured from the top of the fault.

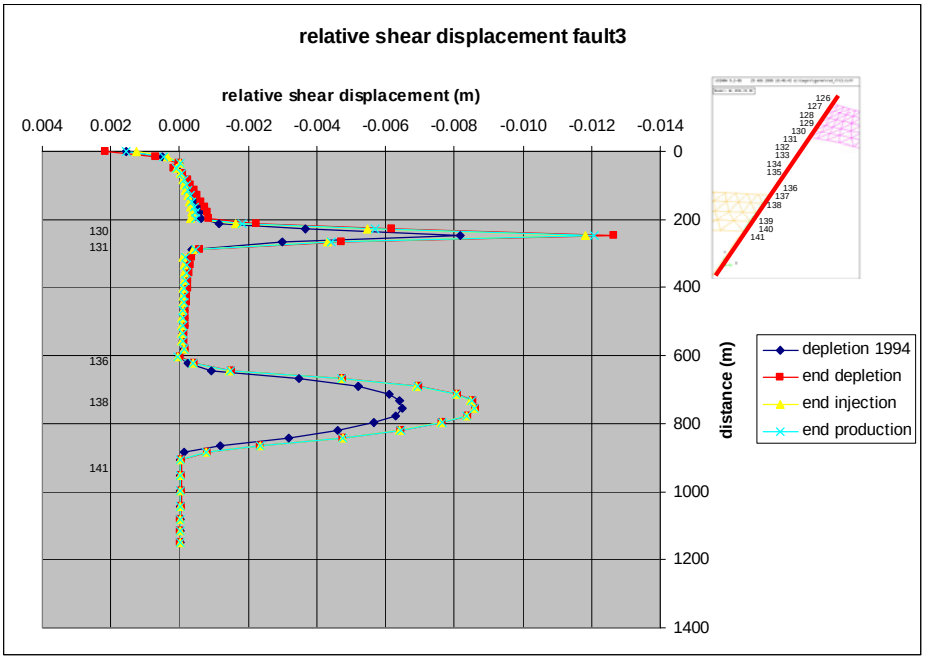

Figure 6.21: Relative shear displacement on fault3, reference scenario 1. Upper right figure gives location of elements. Reservoir rocks presented in pink colours.

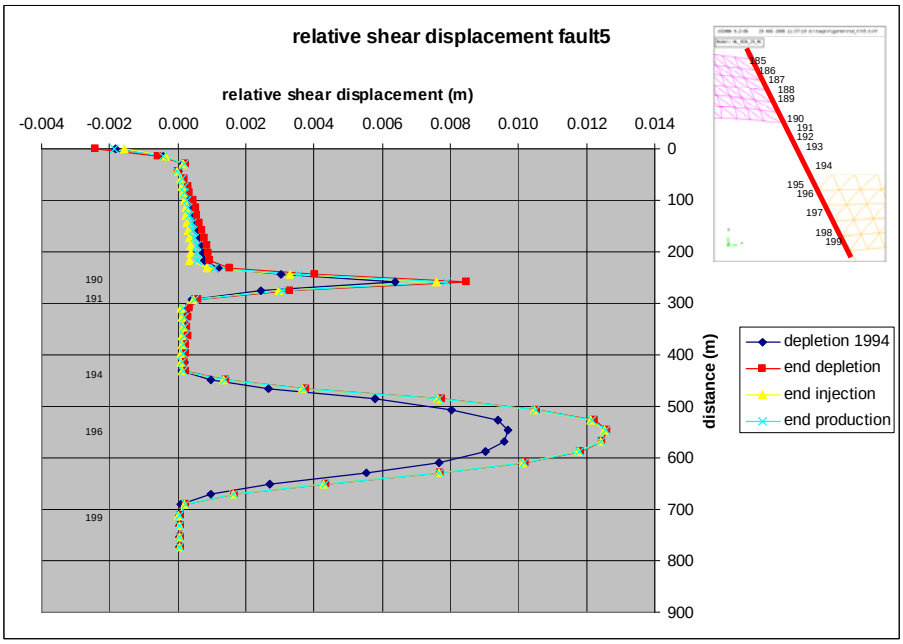

Figure 6.22: Relative shear displacement on fault 5, reference scenario 1. Upper right figure gives location of elements. Reservoir rocks presented in pink colours.

6.5.3.3 Overburden faults: Stress paths and relative shear displacements

Stress changes in the overburden rocks due to pore pressure changes in the reservoir rocks are much smaller than stress changes in the reservoir rocks itself. However, at the extensional setting of the Bergermeer Field with low K'_0 values of 0.36 (and even lower values directly above the Zechstein unit) critically oriented faults in the overburden may be close to Mohr Coulomb failure. In that case relatively small stress changes may lead to reactivation of faults in the overburden. During depletion of the reservoir horizontal stresses in the overburden increase and faults are expected to stabilize. During injection, as the reservoir expands, the overburden rocks are lifted, horizontal stresses decrease and normal fault movement on the overburden faults may occur. Figure 6.24 shows the stress path for element number 5096 (see also Figure 6.23) on fault 8 in the overburden for reference scenario 1. As expected, the stress path moves away from the Mohr Coulomb failure line and the fault stabilizes during depletion. During injection, the stress path moves towards the Mohr Coulomb failure line and the faults becomes less stable, however the stress path does not reach the failure envelope. Only in scenario 5 the stress path during injection leads to plastic failure on faults 7 and 8 (resp. 1.3 cm and 0.7 cm of fault slip during injection). In scenario 5 however, during depletion and injection relatively large movements of the top of the reservoir rocks and top of the Zechstein unit are observed. These large movements of the reservoir rocks result in large subsidence values of 23.2 cm (compared to 12-13 cm for the other scenarios). These large subsidence values do not match the actual maximum measured subsidence (10cm). Therefore it is concluded that in this scenario movements on the overburden faults are overestimated. Fault slip during production is negligible in all scenarios.

Table 6-5, Table 6-6, and Table 6-7 summarize relative shear displacements on the various faults for all scenarios.

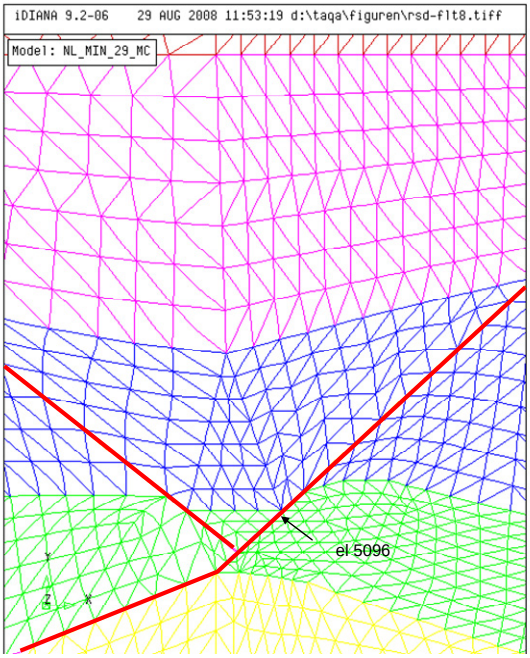

Figure 6.23: Location of element 5096 on overburden fault 8. Stress path for element is shown in Figure 6.24.

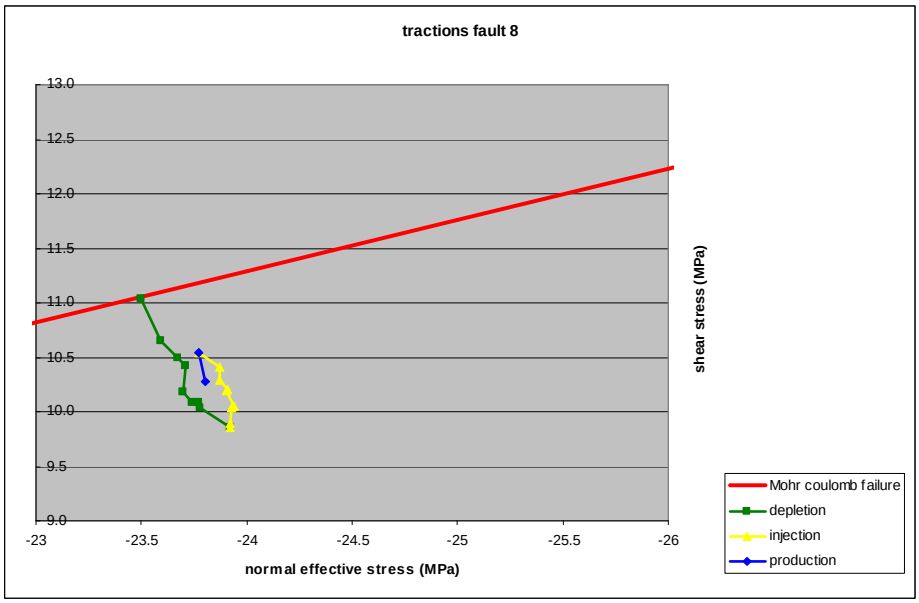

Figure 6.24: Stress path on overburden fault 8. Reference scenario 1.

6.5.3.4 *Faults 1 and 2*

Fault slip during depletion, injection and production on faults 1 and 2 is negligible.

Table 6-5: Maximum relative shear displacement at end depletion (cm)

Scenario	Fault3	Fault4	Fault5	Fault6	Fault7	Fault8
1-reference	1.3	13.3	1.3	<0.1	<0.1	<0.1
2	0.9	13.6	1.0	<0.1	<0.1	<0.1
3	0.7	12.5	0.3	<0.1	<0.1	<0.1
4	1.8	13.8	1.8	0.9	<0.1	<0.1
5	6.7	15.8	12.1	<0.1	0.9	0.6
6	0.3	9.6	0.3	<0.1	<0.1	<0.1
7	0.2	6.3	0.2	<0.1	<0.1	<0.1

Table 6-6: Maximum relative shear displacement (cm) between end depletion and end injection

Scenario	Fault3	Fault4	Fault5	Fault6	Fault7	Fault8
1-reference	<0.1	0.4	<0.1	<0.1	<0.1	<0.1
2	<0.1	0.3	<0.1	<0.1	<0.1	<0.1
3	<0.1	0.5	<0.1	<0.1	<0.1	<0.1
4	0.1	0.7	0.1	<0.1	<0.1	<0.1
5	<0.1	0.5	<0.1	<0.1	1.3	0.7
6	<0.1	0.2	<0.1	<0.1	<0.1	<0.1
7	<0.1	0.1	<0.1	<0.1	<0.1	<0.1

Table 6-7: Maximum relative shear displacement (cm) between end injection and end production (for first production cycle)

Scenario	Fault3	Fault4	Fault5	Fault6	Fault7	Fault8
1-reference	<0.1	<0.1	<0.1	<0.1	<0.1	<0.1
2	<0.1	<0.1	<0.1	<0.1	<0.1	<0.1
3	<0.1	<0.1	<0.1	<0.1	<0.1	<0.1
4	<0.1	<0.1	<0.1	<0.1	<0.1	<0.1
5	<0.1	<0.1	<0.1	<0.1	<0.1	<0.1
6	<0.1	<0.1	<0.1	<0.1	<0.1	<0.1
7	<0.1	<0.1	<0.1	<0.1	<0.1	<0.1

6.5.3.5 *Temperature effects*

In the scenarios described in the former paragraph both pressure changes and temperature changes are taken into account. In Figure 6.25 & Figure 6.26 the temperature change and thermal strains at the end of injection are presented (scenario 1). As shown, the effects of temperature decrease on thermal strains are limited to the area in the direct vicinity of the injection well. For the injection scheme modelled in the 2D DIANA cross section the effect of the local temperature changes on fault tractions and stability is negligible.

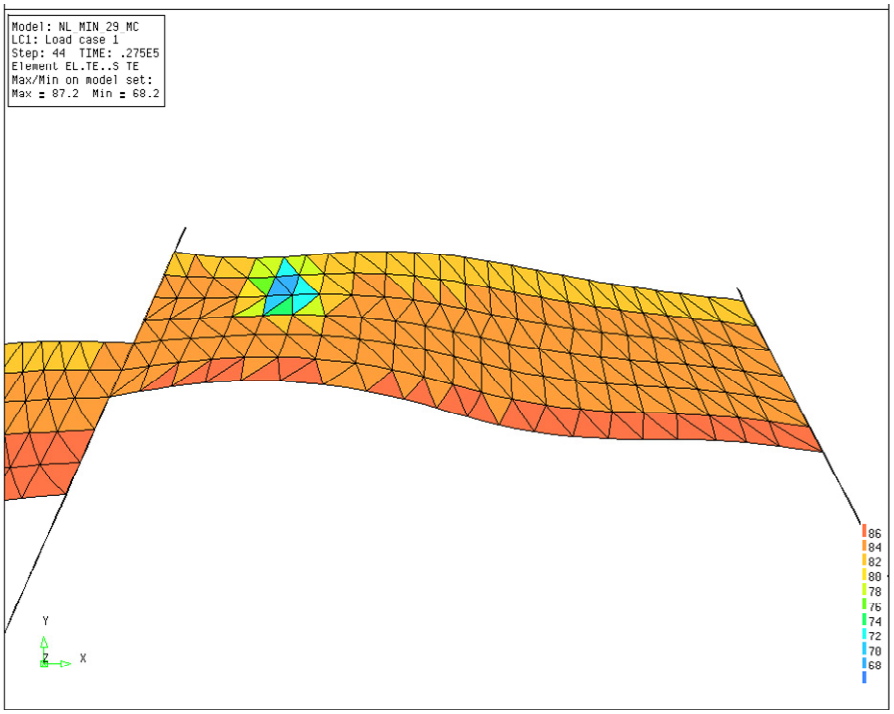

Figure 6.25: Minimum temperatures around injection well during injection (reference scenario 1).

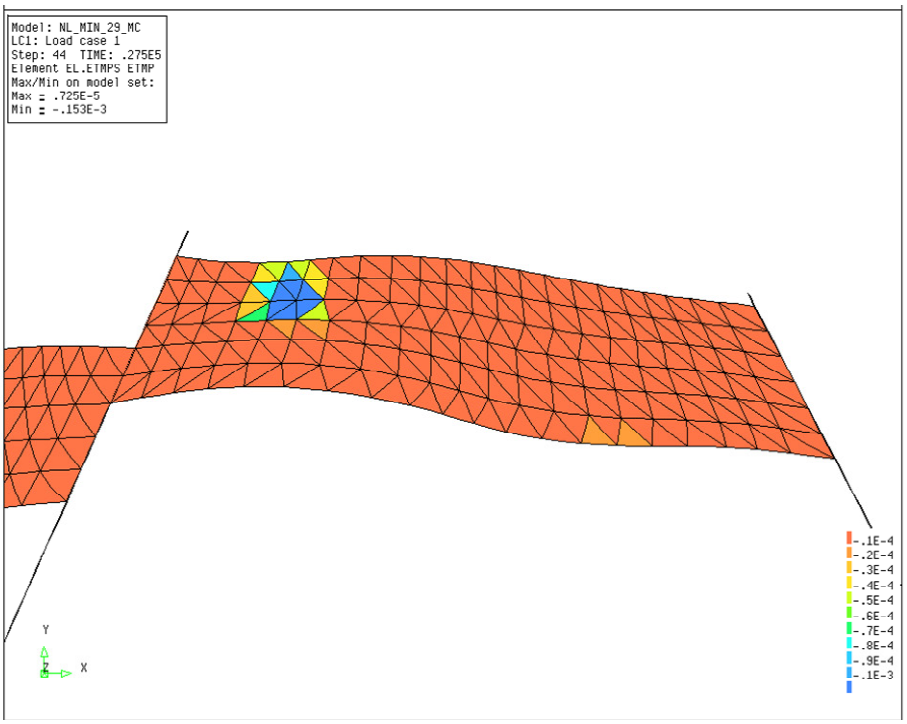

Figure 6.26: Maximum thermal strains around injection well during injection (reference scenario 1).

In the DIANA cross section a temperature decrease of about 16°C (84°C→68°C) is modelled at a distance of approximately 200m from the central fault intersecting the reservoir. The largest temperature decrease obtained from the Eclipse simulations is 52°C (85°C→33°C). In order to get some insight in the effect of this larger temperature drop on stresses and potential fault reactivation a simple axially symmetric model is developed, in which the effect of temperature change and pressure increase around a well on stresses is simulated. The temperature gradient around the well is based on the largest gradient obtained from Eclipse simulations – i.e. a maximum temperature decrease of 85°C→33°C . The temperature change during injection is limited to the area within a radius of approximately 120m around the injection wells (see Figure 6.27). The pore pressure in the reservoir at the time of the largest temperature decrease is 4.6MPa.

The axial symmetric model consists of three horizontal layers: overburden, reservoir rock and underburden. Table 6-8 gives geomechanical parameters for the model. For calculation of horizontal stresses K'_0=0.36 is used.

Three load steps are defined: In the first load step the in situ stresses are initialized. Next, reservoir depletion is simulated by lowering pore pressures from 23MPa to 1 MPa in the reservoir layer. This generates horizontal and vertical stresses in the model which are similar to the stresses obtained in minifrac test BGM#8 in the depleted reservoir. In the last load step the temperature in the reservoir is decreased from 85°C to 33 °C, and the pore pressure is increased to 4.6MPa.

Figure 6.27 gives the temperature and horizontal and vertical stress profiles around the well as a function of distance to the well. At a distance of more than 300m from the injection well only the effect of the pressure increase on stresses is seen. At a distance of more than 150m from the well the change in effective stress due to the temperature

decreases is still small (less than 0.5 MPa for the horizontal effective stress and less than 0.25 MPa for the vertical effective stress) compared to the pressure effect. At distances less than 150m from the well the effect of temperature on stresses becomes significant.

The temperature effect on the effective stresses is also shown in Figure 6.28. In this figure the effective stress state at the end of depletion is shown in the blue Mohr Coulomb circle. During isothermal injection up to a pore pressure of 4.6 MPa the diameter of the Mohr circle decreases and stresses move away from the failure line (green). During nonisothermal injection up to a pore pressure of 4.6MPa and a temperature decline to 33°C, at 100m from the injection well the effect of the temperature decrease is still significant (see red Mohr Coulomb circle, the size of the Mohr circle does not decrease and moves to the left towards the failure line). At a distance of 150m the effect of the temperature decrease is very small compared to the effect of the pressure increase. At 150m there's only a small difference between the stress states of isothermal and nonisothermal injection (small difference between yellow and green Mohr circle). Hence the effect of the temperature decrease on stresses and fault stability is negligible at distances of more than 150m from the injection well. Taking into account an uncertainty of 50m for the location of the faults, due to the limited resolution of the seismics, it is recommended to refrain from planning any injection wells within a distance of 200 m from the internal and bounding faults.

Table 6-8: Input parameters for axial symmetric model.

Layer	Thickness (m)	ρ (g/cm^3)	E (GPa)	ν (-)	C (MPa)	φ (°)	α'_s (-)
Overburden	2100	2.3	30	0.3	-	-	-
Reservoir	180	2.6	18	0.11/0.18	5	35	3.e-5
Underburden	720	2.3	30	0.3	-	-	-

Table 6-9: Subsidence and uplift predictions during depletion, injection of cushion gas (CG) and working gas (WG) and production of working gas

Scenario	**Subsidence depletion (cm)**	**Uplift injection (CG & WG) (cm)**	**Subsidence production (cm)**
1-reference	12.8	6.8	2.3
2	12.0	6.5	2.2
3	13.1	7.1	2.4
4	12.8	6.7	2.2
5	23.2	10.9	2.7
6	12.7	6.8	2.3
7	12.7	6.9	2.3

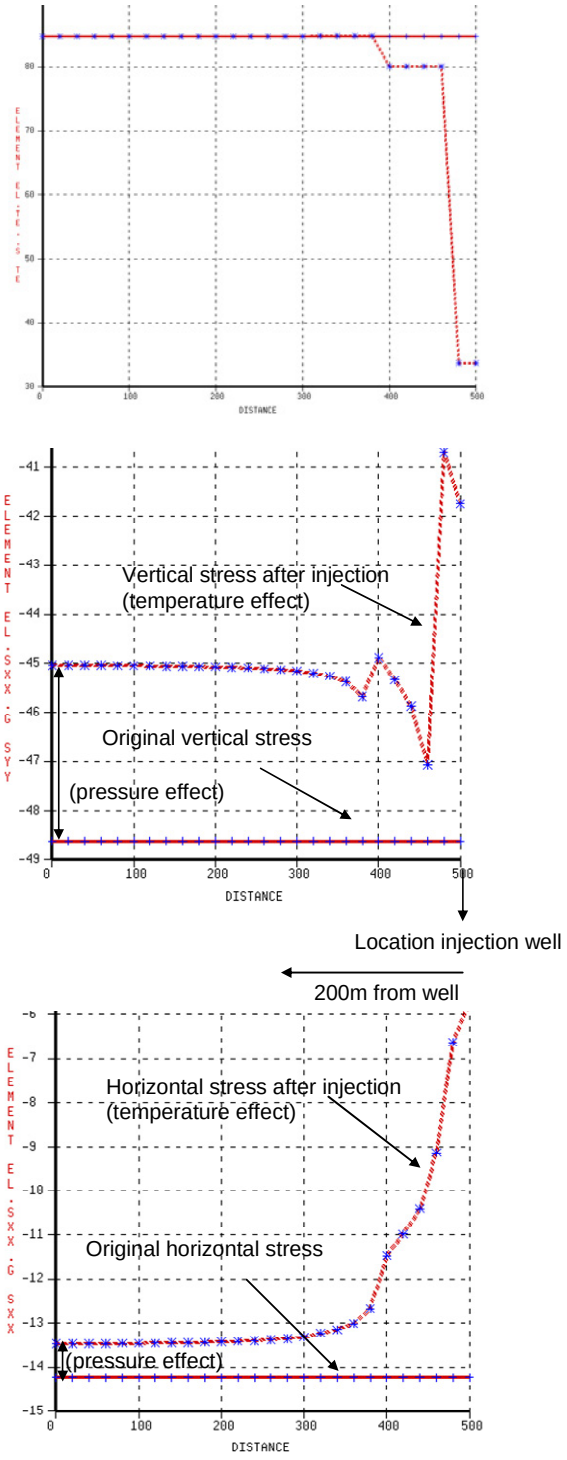

Figure 6.27: Applied temperature load (top) and the induced change in the vertical effective stress (middle) and horizontal effective stress (bottom) around injection well predicted by DIANA simulations. Position of injection well is at 500m. Note that the effect of the temperature decrease on horizontal and vertical effective stresses at a distance of more than 150m from the well is very small compared to the effect of the pressure increase due to injection .

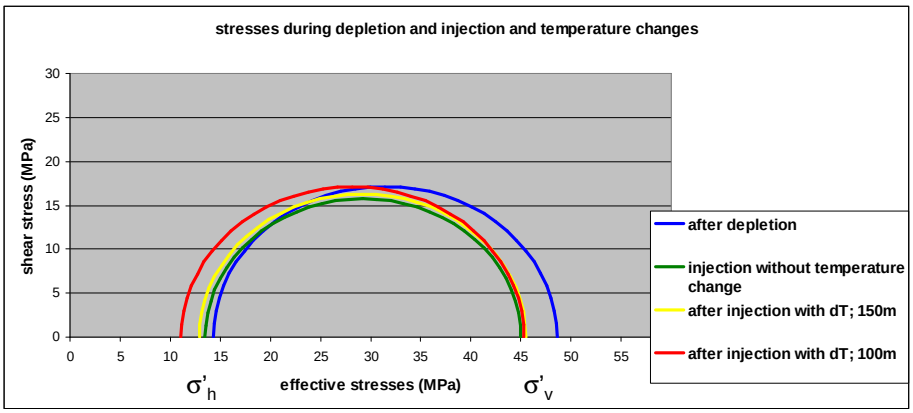

Figure 6.28: Stresses at the end of depletion (red), during insothermal injection up to a pore pressure of 4.6MPa, (green), during nonisothermal injection up to 4.6MPa at a distance of 150m (yellow) and 100m (red) from the injection well.

6.5.3.6 Subsidence and uplift

Predicted subsidence and uplift values at surface level are shown in Table 6-9. Subsidence values for all scenarios vary between 12.0 cm and 13.1 cm, with the exception of scenario 5 which gives a subsidence of 23.2 cm. The measured maximum subsidence at the end of depletion is about 10.5cm. All scenarios except scenario 5 overestimate subsidence with 1.5cm to 2.6cm.. This difference in predicted and measured subsidence values of approximately 15-25% can be explained by the fact that subsidence is modelled in 2D under plane strain conditions and the sensitivity of subsidence modelling to the choice of overburden parameters. However, a difference of 13.2 cm between the measured and predicted subsidence in scenario 5 cannot be explained by the restrictions of plane strain conditions and choice of overburden parameters. As concluded before, displacements calculated in scenario 5 appear to be much overestimated and very unlikely. Uplift of the ground surface during the injection of cushion gas and working gas varies between 6.5 cm and 7.1 cm for all scenarios except scenario 5. As with subsidence predictions, uplift predictions are likely overestimated; a correction of 15-25 % gives uplift values between 4.9 and 6.0 cm. Subsidence from the end of injection to the end of the first production stage varies between 2.2 cm and 2.4 cm for all scenarios, except scenario 5. A correction of 15-25% gives a subsidence range of 1.6 to 2.0 cm.

6.6 Conclusions and recommendations of geomechanical analysis

Seven scenarios are defined for modelling, in which Poisson's ratio, stiffness ratio between top seal and reservoir rock, fault shear strength and material behaviour of the Zechstein (rocksalts) are varied. Reference scenario 1 gives a best fit with the stress measurements of the minifrac test performed in BGM#8. Scenario's 4 (large stiffness ratio), 6 and 7 (high fault strength) also show a good match with the results of the minifrac test. The gradients of the stress paths in scenario 2 (average Poisson's ratio) and 3 (low stiffness contrast between reservoir rock/overburden) are too low, when compared to the gradient obtained from the minifrac tests. The stress field modelled in scenario 5, in which the rocksalt is modelled with a time dependent creep model, gives the worst fit with the results of the minfrac test. Also, displacements in scenario 5 seem to be much overestimated when compared to actual subsidence measurements.

Geomechanical conclusions are based on the results of the best fit scenarios 1, 4, 6 and 7.

6.6.1 Conclusions

During ***depletion,*** only fault segments intersecting or bounding the reservoir show a potential for reactivation. Large plastic fault movements occur on the central fault (4) in the reservoir, where reservoir rocks on both sides of the fault overlap. Maximum fault slip during depletion varies between 6.3 cm and 13.8 cm. Maximum fault slip observed on the faults bounding the reservoir (3 and 5) varies between 0.2 cm and 1.8 cm. At the end of depletion, stress conditions on the central and bounding faults are at or close to failure conditions.

During ***injection*** for the main parts of faults intersecting or bounding the reservoir (3, 4, 5) stress paths move away from failure conditions and these parts stabilize during injection. Locally some fault slip is observed on the central fault (4), directly below and above the overlap of reservoir rocks. *Fault movements during injection are much smaller than during depletion* and are limited to a maximum of 0.7 cm. During injection, stress paths on the overburden faults move towards failure conditions. However, stress changes in the overburden due to injection of gas in the reservoir are small compared to stress changes observed in the reservoir and large shear displacements on the overburden faults seem unlikely.

During ***production*** of working gas no fault slip is observed.

All plastic fault displacements observed during depletion and injection are normal faulting movements. This means a discrepancy exists between the interpretation of focal mechanisms reported by the KNMI (reverse faulting mechanism) and the displacement mechanisms from the geomechanical analysis (normal faulting mechanism). It is noted that in an extensional tectonic setting such as the setting for the Bergermeer Field, predominantly normal fault movements are expected.

For the injection scheme modelled in DIANA the effect of the local temperature changes on fault stability is negligible. Additional results from a simplified axial symmetric model, in which the maximum temperature decrease from reservoir modelling is used, indicate that effects of temperature on stresses are limited to a distance of 150m from the injection well. Taking into account an uncertainty of 50m for the location of the faults, due to the limited resolution of the seismics, it is recommended to refrain from planning any injection wells within a distance of 200 m from the internal and bounding faults (Figure 6.29). In case the injected gas is heated a distance of 150 m from the fault should be observed in order to avoid direct injection into the fault zone.

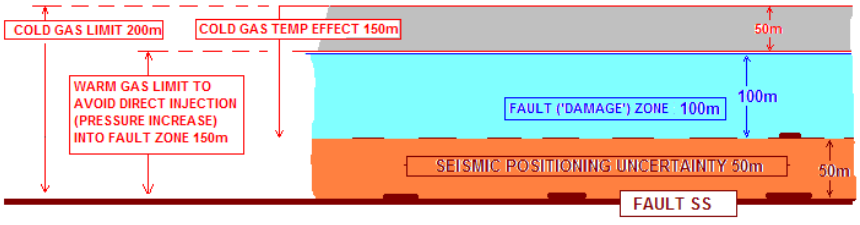

Figure 6.29: Schematic overview of the recommended distances within which the operator should refrain from planning injection wells. Distances depend on whether cold or warm gas is injected.

Predicted subsidence values during depletion are overestimated when compared to actual values by 15-25%. Taking into account a correction factor of 15-25%, the predicted uplift during injection is 4.9-6.0 cm.. The predicted subsidence during production is 1.6-2.0 cm.

6.6.2 Recommendations

1. As the major effect of gas injection and production is during cushion gas injection and the first injection/production cycle, only these periods have been modeled. Longer term temperature distributions after a few injection/production cycli and the effects on stresses are unknown. Faults subjected to repeated cycles of loading/unloading may exhibit fatigue and fail at lower stresses later, after a few cycles. It is recommended to extend the current analysis with subsequent injection/production cycles to investigate the rock response.
2. In order to prevent temperature effects on and direct injection in the fault zones, it is recommended to refrain from planning any injection wells within a distance of 200 m from the internal and bounding faults (uncertainty of the location of the faults due to limited resolution of the seismics taken into account).
3. In order to minimize temperature effects around wells near the faults during cushion gas injection it is recommended to use high injection rates in wells far from the faults and low injection rates in the wells close to the faults.
4. In this study it is concluded that injection of cold gas according to the well scheme supplied does not affect the stability of the known faults, when injection wells are located at a minimum distance of 200m from the faults. However, it is still feasible that unrecognized subseismic faults are present in the reservoir which may be activated by the injection of cold gas. Also the effect of potential thermal cracking on permeability and preferential flow has not been investigated.
5. Conducting repeated minifrac and extended leak-off tests during reservoir re-pressurization is recommended for determination of the reservoir stress path.
6. Field performances have to be monitored and coupled to the model to further decrease the level of uncertainties during operations.

7 Seismic hazard analysis

Table 7-1 shows the slip released during the earthquakes of 1994 and 2001 (calculated using equations 5 and 6) for the Bergermeer gas field and compares the slip to the modelled slip displacements in DIANA. We have assumed that the seismic slip occurred on the internal fault and only for the part of the fault width which displayed maximum slip in the DIANA modelling. Since the DIANA modelling is two-dimensional we have further assumed that the entire fault length of the internal fault (2.5 km) has slipped. For some scenario's (2, 6 and 7), the slip modelled in DIANA in 2001 is smaller than the total calculated slip released during the earthquakes. This makes these scenarios very unlikely.

The difference between the modelled slip and the released slip represents slip that either was released aseismically or is still present. The largest difference between total released slip and modelled slip is 6.7 cm (scenario 4). If we assume that the slip present in 2001 is released (seismically or aseismically) then the largest slip accumulated between 2001 and 2006 is obtained in scenario 5. The 2.0 cm of accumulated slip corresponds to a magnitude 3.15 earthquake, if we assume this slip would be released in one seismic event. However, the unacceptable fit to the subsidence data of scenario 5 (section 6.5) indicates that this scenario is unlikely. The second largest accumulated slip (scenario 3) of 1.5 cm would correspond to a magnitude 3.0 earthquake. The slip modelled with DIANA in 1994 is always larger than the slip released by the earthquakes in 1994. Therefore, part of the slip accumulated in 1994 was only released during the earthquakes of 2001 or has to be released aseismically.

The large uncertainty in epicentre location of the earthquakes in 1994 and 2001 could not unambiguously place these events on the internal fault. It remained feasible that the events occurred on one of the bounding faults or even on one of the many listric overburden faults. The overburden faults only displayed displacements for scenario 5 of the DIANA modelling. Therefore we show in Table 7-2 the slip released during the earthquakes of 1994 and 2001, assuming that they occurred on the overburden faults, and the slip modelled on the overburden faults (number 7 and 8) for scenario 5 of DIANA. The total modelled slip is much smaller than the slip released during the earthquakes which makes it improbable that the events occurred on one of the listric overburden faults.

Table 7-1: Slip displacement (in cm) due to the earthquakes in 1994 and 2001 and total slip displacement (in cm) due to earthquakes compared to the slip displacement modelled with DIANA at 1994, 2001 and 2006 for the different DIANA scenarios.

Scenario	fault width*	earthquakes			modelled with DIANA		
		1994	2001	total	1994	2001	2006
1	265	2.2	5.7	7.9	10.1	12.2	13.3
2	230	2.7	6.9	9.6	6.8	8.3	9.1
3	237	2.5	6.3	8.8	9.4	11.0	12.5
4	292	2.0	5.1	7.1	10.5	12.7	13.8
5	165	3.6	9.1	12.6	11.3	13.8	15.8
6	218	2.7	6.9	9.6	7.2	8.9	9.6
7	165	3.6	9.1	12.6	5.5	6.3	6.3

* fault width taken from the DIANA scenarios

Table 7-2: Slip displacement (in cm) due to the earthquakes in 1994 and 2001 and total slip displacement (in cm) due to earthquakes compared to the slip displacement modelled with DIANA at 1994, 2001 and 2006 for the overburden faults of scenario 5.

overburden fault	fault width*	earthquakes			modelled with DIANA		
		1994	2001	total	1994	2001	2006
7	300	1.8	4.5	6.3	0.5	0.7	0.9
8	200	2.7	6.7	9.4	0.1	0.3	0.7

* fault width taken from the DIANA scenarios

Table 7-3: Mean displacement (δ_{mean}) and maximum displacement (δ_{max}) over the fault width for the 7 scenarios from DIANA and their maximum seismic magnitude for the internal fault in the reservoir.

	δ_{mean} (cm)	M	δ_{max} (cm)	M	fault width (m)
Scenario 1	0.1	2.6	0.4	2.6	100
Scenario 2	<0.1	2.5	0.3	2.4	100
Scenario 3	0.1	2.6	0.5	2.6	100
Scenario 4	0.2	2.7	0.7	2.7	100
Scenario 5	<0.1	2.4	0.5	2.4	50
Scenario 6	<0.1	2.4	0.2	2.5	200
Scenario 7	<0.1	2.4	0.2	2.4	150

Table 7-3 shows the displacements found for the scenarios of the DIANA modelling on the internal fault and their corresponding maximum seismic magnitude for the injection stage. The mean displacement is taken over the entire fault width of the internal fault in the reservoir (448 m) and the maximum displacement is taken over the part of the fault which displayed the maximum displacement (indicated fault width in Table 7-3). Since the DIANA scenarios show displacements for a two-dimensional slice of the reservoir, we have further assumed that the entire length of the internal fault in the reservoir (2.5 km) has slipped over a portion of the fault width (maximum displacement, δ_{max}) or the entire fault width in the reservoir (mean displacement over the fault width, δ_{mean}). During injection, the largest slip for the different scenarios corresponds to seismic magnitudes between 2.4 and 2.7. The seismic magnitudes in Table 7-3 are much smaller than the calculated maximum seismic magnitude feasible on the internal fault of the Bergermeer field of 3.9. The difference can be explained by the smaller amounts of slip observed (at least one order of magnitude smaller; millimetres instead of centimetres).
We do not show the displacements and corresponding seismic magnitudes for the production stage since they are much smaller (see Table 6-7).

Scenario 5 of DIANA is the only scenario that displays slip on the overburden faults. Therefore, Table 7-4 shows the mean displacement and maximum displacement on the overburden faults and the corresponding seismic magnitudes. In this, we have assumed that the length of the overburden faults that slipped is 2.5 km (on top of the reservoir). During injection, the overburden faults show a maximum magnitude of 3.44 which is larger than the expected magnitudes in the reservoir. However, scenario 5 does not match the observed subsidence which makes it an unlikely scenario (see section 6.5).

Table 7-4: Mean displacement (δmean) and maximum displacement (δmax) over the fault width for the overburden faults of scenario 5 from the DIANA modelling and their maximum seismic magnitude.

overburden fault	δ_{mean} (cm)	M	δ_{max} (cm)	M	fault width (m)
7	0.9	3.23	1.3	3.44	600
8	0.5	3.07	0.7	3.02	280

For the range of seismic magnitudes expected during the injection stage (2.4 to 2.7) the corresponding earthquake intensity varies between III and IV. Earthquakes of intensity III and IV may be felt inside the house and some shaking may occur of glassware, hanging objects, doors and windows. However, earthquakes of intensity III and IV will cause no damage to buildings.

8 Conclusions & Recommendations

8.1 Conclusions

The results of this study are derived from data supplied by TAQA Energy BV. (e.g. well schemes, injection/production schedules, history matched reservoir model seismics/fault geometry, stress data, etc) and may not be valid in case of any alterations to these data prior and during operation of the proposed UGS facility.

The scope of this study is to assess the risks of seismic activity induced by pressure and temperature changes resulting from cold gas injection and gas production. In a reservoir modeling study, a schedule for gas injection and production was implemented and pore pressure and temperature changes were simulated for one injection/production cycle. Reservoir modelling results lead to the following conclusions:

1. The temperature distribution in the field after injection of cold cushion and working gas and one production phase shows a temperature decline localized around the wells. The temperature of the rest of the field remains largely unaffected.

2. The first two years of injection are most important. After this period gas needs to be compressed, this increases the injection temperature. Subsequent gas production results in warm gas flowing to cool down areas, heating them again.

The pressures and temperatures obtained from the reservoir model are used in a geomechanical model to determine the changes in stresses and deformations in the reservoir and surrounding rocks. This way, the effects of pore pressure and temperature changes on the stability of existing faults are investigated. Faults can be considered as weak planes or weak zones in the reservoir rocks, and deformations caused by the extraction and injection of gas in the reservoir will be largely accommodated on fault planes or within fault zones. Geomechanical modelling results lead to the following conclusions:

3. During the period of ***depletion*** (1971-2006)**,** only fault segments intersecting or bounding the reservoir show a potential for reactivation. Large fault movements occur on the central fault in the reservoir, where reservoir rocks on both sides of the fault overlap. At the end of depletion, stress conditions on the central and bounding faults are at or close to failure conditions.

4. During ***injection*** of cold gas, the main parts of the faults intersecting and bounding the reservoir stabilize. Locally some fault slip is observed on the central fault, intersecting the reservoir, directly below and above the overlap of reservoir rocks. *Fault movements during injection are an order of magnitude smaller than during depletion.*

5. During ***production*** of working gas no fault slip is observed.

6. The localized temperature decline around the injection wells does not affect the stability of the known faults, when injection wells are located at a minimum

distance of 200m from the faults (uncertainty in fault location due to limited resolution of the seismics taken into account)

Magnitudes of seismic events were estimated, based on shear moduli of the faults, fault area and slip displacements on the faults derived from the geomechanical models. Seismic hazard analysis leads to the following conclusions:

7. During injection, the largest slip observed in the geomechanical models corresponds to seismic magnitudes ranging between 2.4 and 2.7.

8. The maximum possible seismic magnitude is 3.9. Larger magnitude earthquakes are improbable due to the limited dimensions of the faults.

8.2 Recommendations

1. In order to prevent temperature effects on and direct injection in the fault zones, it is recommended to refrain from planning any injection wells within a distance of 200 m from the internal and bounding faults.

2. In order to minimize temperature effects around wells near the faults during cushion gas injection it is recommended to use high injection rates in wells far from the faults, low injection rates in the wells close to the faults.

3. As the major effect of gas injection and production is during cushion gas injection and the first injection/production cycle, only these periods have been modeled. Longer term temperature distributions after a few injection/production cycli and the effects on stresses are unknown. Faults subjected to repeat cycling of loading/unloading may exhibit fatigue and failure at lower stresses. It is recommended to extend the current analysis with subsequent injection/production cycles to investigate the temperature distribution and rock response.

4. Field performances have to be monitored and coupled to the model to further decrease the level of uncertainties during operations. Conducting repeated minifrac and extended leak-off tests during reservoir re-pressurization is recommended for determination of the reservoir stress path, as well as monitoring of well temperatures and pressures.

5. We emphasize that the modeled temperature effects only apply for gas injection. Due to the significantly higher heat capacity of water, the area of which the temperature is affected by the cold water injection will be more extensive. Hence, in case cold water injection is planned more research is necessary.

6. We note that the effect of cold gas injection on the well bore stability has not been investigated in this study.

9 References

Begeleidingscommissie Onderzoek Aardbevingen, 1993. Eindrapport multidisciplinair onderzoek naar de relatie tussen gaswinning en aardbevingen in Noord-Nederland.

Bergermeer UGS modelling study phase 2 Horizon Energy Partners BV, March 2008.

De Crook, et al., 1996. A seismic zoning map conforming to Eurocode 8 and practical earthquake parameter relations for the Netherlands. Geologie en Mijnbouw 75, 11-18.

Fokker, P.A. & Orlic, B., 2006. Semi-analytic modelling of subsidence. Math. Geol. 38, 565-589.

Grasso, J.-R. & Sornette, D., 1998. Testing Self-Organized Critically by induced seismicity, Journal of Geophysical Research, volume 103, Issue B12, p. 29,965-29,988.

Haak, H. W., Dost, B & Goutbeek, F. H., 2001. Seismische analyse van de aardbevingen bij Alkmaar op 9 en 10 september en Bergen aan Zee op 10 oktober 2001. Technical report; TR-239, KMNI.

Haak H., 1994. Seismic analysis of the earthquake near Alkmaar on 21 September, 1994, Unpublished report of Royal Netherlands Meteorological Institute, 29p.

Hanks, T.C. and Kanamori, H., 1979. A moment magnitude scale, J. Geophys. Res., v. 84, 2348-2350.

Kanamori, H. and Anderson, D. L., 1975. Theoretical basis of some empirical relations in seismology. Bull. Seismol. Soc. Am. Volume 65, 1073-1095.

KNMI, Seismische analyse van de aardbeving bij Alkmaar op 6 augustus 1994, 1994.

KNMI, Seismische analyse van de aardbeving bij Alkmaar op 21 september 1994, 1994.

Kroon, I.C., Nguyen, B-L., Fokker, P.A., Muntendam-Bos, A.G. & De Lange, G., 2008. Disentangling shallow and deep processes causing surface movement. Accepted for publication by Math. Geol.

Kutasov, I.M. et al, 1999, Applied geothermics for petroleum eengineers, Elsevier.

Logan, J.M. and Higgs, N. G. and Rudnicki, J. W.,1997. Seismic risk assessment of a possible gas storage project in the Bergermeer field, Bergen concession.

Mulders, F.M.M., 2003. Modelling of stress development and fault slip in and around a producing gas reservoir. PhD-thesis Technical University Delft.

Muntendam-Bos, A.G., Kroon, I.C. & Fokker, P.A., 2008. Time-dependent inversion of surface subsidence due to dynamic reservoir compaction. Math. Geosci. 40, 159-177.

Nagelhout, A.C.G., 1997. Investigating fault slip in a model of an underground gas storage facility. Int. J. Rock. Mech. & Min. Sci. 3-4, paper No.212.

Roest, J. P. A. & Mulders, F. M. M., 2000. Modelleren van bewegingen en het spanningssveld bij gasrservoirs. Workshop ‘Geinduceerde aardbevingen in Noord-Nederland’, de Bilt, 7 november 2000.

Roest, J.P.A., Kuilman, W., 1994. Geomechanical analysis of small earthquakes at the Eleveld gas reservoir. Eurock’94.

Rondeel, H.E., Everaars, J.S.L., 1993. Spanning in noordoost Nederland: een breakoutanalyse.

Segall, P., 1989. Earthquakes triggered by fluid extraction. Geology, v.17, p.942-946, October 1989.

Segall, P., Fitzgerald, S.D., 1998. A note on induced stress changes in hydrocarbon and geothermal reservoirs. Tectonophysics 289 (1998), p. 117-128.

SENERGY, March 2008. Technical note. High Level Geomechanics Review for Bergermeer Gas Storage Project. Reference: P\PROJECT\W07TBV01L.

Scholz, C. H., 1990. The mechanics of earthquakes and faulting, Cambridge University Press, Cambridge, 439p.

Schroot, B.M., Fokker, P.A., Lutgert, J.E., Van Der Meer, B.G.H., Orlic, B., Scheffers, B.C. & Barends, F.B.J., 2005. Subsidence induced by gas production: an integrated approach. In: Land Subsidence – special vol. Proceedings of the seventh international symposium on land subsidence, Shanghai, P.R. China, 23-28 October; pp 121-136.

Somertron, W.H., 1992, Thermal properties and temperature-related behavior of rock/fluid systems, Elsevier.

Van Eijs, R.M.H.E., Mulders, F.M.M., Nepveu, M., Kenter, C.J. & Scheffers, B.C., 2006. Correlation between hydrocarbon reservoir properties and induced seismicity in the Netherlands. Engineering Geology, 84, 99-111.

Weast, R.C., 1978, The Handbook of chemistry and Physics 59th edition, *CRC Press inc.*

Winningsrapport Alkmaar veld, december 2003.

Winningsrapport UGS Norg, december 2003.

Winningsrapport UGS Grijpskerk, december 2003.

Zoback, M.D., 2007. Reservoir geomechanics.

10 Signature

Utrecht, November 2008 TNO Built Environment and Geosciences

O.A. Abbink
Teamleader Oil and Gas

Mrs. Dr. A.G. Muntendam-Bos
Author

A Subsidence data

Table A-1: **Overview of the data utilized in the subsidence inversion procedure.**

X	Y	PUNT	1972	1980 / 1981	1984	1988	1991 / 1992	1997	2001 ONAP	2006 ONAP
113450	515520	0A2390			0.032	0.032	0.017	0.017	-0.008	-0.008
103080	514430	0A2699							16.281	16.218
107800	525180	14C001		3.428	3.427	3.421	3.414	3.41	3.403	3.402
108810	525980	14C005	0.783	0.778	0.782	0.778				
108880	526000	14C006	1.246	1.231		1.224				
107840	527500	14C007	3.356	3.352	3.355	3.352	3.347	3.347	3.335	3.336
108810	525980	14C066	0.038	0.036	0.04	0.036				
104990	525810	14C111	16.327	16.277	16.265	16.254	16.246	16.238		
104520	525200	14C112	8.392	8.362	8.35	8.338	8.331	8.323	8.311	8.304
104590	526820	14C114		4.406	4.394	4.383	4.377	4.369	4.358	4.354
109150	525520	14C115		0.428	0.422					
108380	526740	14C116		1.095	1.097	1.091	1.084	1.085	1.079	1.077
104620	527080	14C126		1.614	1.594	1.574	1.563	1.549	1.535	1.526
104970	526750	14C127		5.356	5.347	5.337	5.331	5.324	5.313	5.311
105060	526310	14C128		17.421	17.41	17.4	17.392	17.385	17.380	17.372
105000	525900	14C129		18.124	18.113	18.101	18.094	18.086	18.081	18.072
105020	525630	14C130		13.28	13.268	13.256	13.249	13.242	13.233	13.229
104790	525450	14C131		10.288	10.276	10.264	10.257	10.25	10.239	10.233
105400	525760	14C132		11.08	11.07	11.061				11.040
105780	526010	14C133		10.485	10.477	10.469	10.462			
106040	526340	14C134		5.34	5.334	5.324	5.311			5.299
106650	526180	14C135		4.034	4.031		4.018			4.002
107050	525600	14C136		6.401	6.399	6.39	6.383	6.377	6.369	6.368
107730	526570	14C137		-0.327	-0.326	-0.339	-0.351	-0.354	-0.378	-0.381
108050	527220	14C138		1.158	1.158					
106430	526180	14C158					9.078			9.069
108050	527220	14C161				1.295	1.279	1.274		
109120	525530	14C178						0.167	0.159	0.162
108860	526000	14C179						-0.239	-0.252	0.026
108850	525970	14C184							0.729	0.731
108800	525970	14C188							0.511	0.512
111120	526320	14D019			0.972		0.961			0.954
111220	526600	14D321			1.319		1.309			1.304
111160	525330	14D370					-1.593			-1.595
109040	512510	19A001	1.598	1.596	1.597	1.591	1.582	1.579	1.578	1.579
109250	512880	19A003					1.396	1.392	1.390	1.383
109280	512990	19A005	1.637	1.636	1.636	1.633	1.625	1.621	1.620	1.620
109320	513260	19A006			4.286		4.278	4.277	4.278	
109980	513950	19A008	1.593	1.59	1.592	1.586	1.576	1.572	1.568	1.569
105120	515000	19A009			3.842		3.828	3.82	3.810	3.813
105720	517680	19A013	4.051	4.048	4.043	4.035	4.03	4.025	4.015	4.014

108120	518860	19A014		-0.249	-0.257	-0.267	-0.289	-0.3	-0.315	
106320	519980	19A015	4.946	4.929	4.918	4.904	4.889	4.877	4.862	4.856
108330	520330	19A016	2.05	2.027	2.019	2.007	1.988	1.973	1.958	1.954
108840	522600	19A019	2.621	2.613	2.611	2.604	2.596		2.581	2.582
108160	523880	19A020		9.075	9.074	9.056				
105160	513610	19A039			3.986		3.978	3.976		3.977
106940	516320	19A055				0.56	0.555	0.551	0.543	0.546
108110	519310	19A071	-0.511	-0.531	-0.539	-0.55	-0.57			-0.602
109680	519020	19A073	0.051	0.03	0.024	0.015	-0.007			
109960	518410	19A083		0.226	0.224	0.209	0.186			
109370	519350	19A084	0.481	0.46	0.454	0.444	0.424			
104070	519600	19A085	7.957	7.951	7.946	7.937	7.918			
108230	514220	19A089						0.831		0.836
109620	524580	19A090	1.546	1.533	1.532	1.525		1.509	1.501	1.499
104240	523500	19A091	5.774	5.752	5.738	5.72	5.705			
104170	523000	19A092	3.764	3.75	3.737	3.721	3.713			
108840	522610	19A093	2.241	2.235	2.233	2.227	2.219	2.219		
104260	521900	19A094	2.629	2.617	2.604	2.587	2.574	2.556		
104920	521830	19A095	4.488	4.474	4.461	4.442	4.422	4.411	4.393	4.383
105800	521770	19A096	3.599	3.583	3.571	3.553	3.537		3.508	3.501
106630	521890	19A097	3.541	3.525	3.515	3.5	3.485	3.472	3.459	3.453
104390	520940	19A098	4.808	4.798	4.786	4.77	4.754			
104200	520280	19A099	6.636	6.63	6.623	6.611	6.601	6.593	6.581	6.579
104800	519780	19A100	13.466	13.456	13.447	13.435	13.424	13.414	13.408	13.399
105580	520060	19A101	8.261	8.251	8.241	8.229	8.216	8.205	8.194	8.188
107190	520230	19A102	3.161	3.142	3.132	3.119	3.103	3.088	3.073	3.069
103880	518890	19A103	5.187	5.183	5.181	5.175	5.17	5.165	5.156	5.157
103610	517980	19A104	5.163	5.159	5.161	5.153	5.147	5.146	5.135	5.135
104120	517610	19A105	8.811	8.809	8.809	8.801	8.796			
104920	517640	19A106	8.677	8.675	8.674	8.666	8.66	8.655	8.649	8.651
106320	516540	19A107	0.285	0.277	0.273	0.264	0.258	0.25	0.239	0.241
107380	516840	19A108	-0.78	-0.785	-0.79	-0.795	-0.804	-0.809	-0.818	-0.819
108940	516780	19A109	-0.674	-0.687	-0.692		-0.713	-0.723	-0.734	-0.737
109800	523480	19A110		-0.505	-0.506	-0.51		-0.516		
108100	519340	19A112		0.094	0.085	0.073	0.052	0.037	0.022	
109560	516450	19A115		0.152	0.146	0.139	0.125	0.117	0.106	0.103
109490	522750	19A116		-0.625	-0.627	-0.633	-0.641	-0.646	-0.655	-0.653
108460	522150	19A117		3.471	3.466	3.456	3.446	3.434	3.422	3.417
104390	524270	19A118		8.916	8.905	8.892				
107440	521640	19A119		5.229	5.222	5.208	5.193	5.182	5.170	5.164
108600	518540	19A120		-0.464	-0.471	-0.483	-0.503	-0.516	-0.533	-0.537
109300	518030	19A121		-0.526	-0.537	-0.549	-0.575	-0.591	-0.611	-0.615
109700	515600	19A122		1.182	1.179	1.171	1.157	1.152	1.145	1.144
104520	524970	19A123		9.272	9.254	9.243	9.235	9.227	9.213	9.207
104580	524740	19A124		8.942	8.929	8.914	8.906	8.898	8.885	8.879
104320	523930	19A125		9.213	9.2	9.184	9.175	9.165	9.149	9.144
104650	521570	19A126		6.102	6.088	6.07	6.051	6.039	6.021	6.012
104580	521180	19A127		4.845	4.831	4.811	4.792		4.760	4.753

104180	520640	19A128		4.868	4.859	4.845	4.831			
104190	520090	19A129		6.178	6.173	6.162	6.153	6.136		
104270	519650	19A130		9.886	9.88	9.871	9.863	9.856		
105360	521860	19A131		9.49	9.475	9.456	9.437	9.426	9.408	9.399
106240	521880	19A132		3.149	3.138	3.121	3.107	3.095	3.079	3.073
108000	524460	19A133		7.852	7.851	7.846	7.84	7.836	7.831	7.831
108550	524170	19A134		4.372	4.371	4.366				
108950	524330	19A135		2.489	2.489	2.485				
108480	523280	19A136		4.175	4.171	4.163	4.155	4.147	4.140	4.140
108570	520580	19A137		1.234	1.226	1.212	1.192	1.177	1.160	1.154
109330	520330	19A138		0.649	0.645	0.634	0.618			
109850	519780	19A139		0.948	0.942	0.93	0.911			
108790	519430	19A140		0.792	0.785	0.774	0.751			
108980	513820	19A141			1.201			1.19		1.191
106190	515780	19A145			0.728		1.719	0.715	0.705	0.709
105300	515160	19A146			2.83		2.82	2.816	2.808	2.815
105020	514280	19A147			3.654		3.646	3.642		3.641
105530	516820	19A149			3.673	3.662	3.653			
108000	521360	19A150			4.713	4.698	4.68			
108440	516890	19A151			-0.869	-0.872	-0.883	-0.89	-0.900	-0.902
103160	514880	19A155					13.098	13.096	13.094	13.096
103830	514930	19A156					9.609	9.606	9.602	9.605
109320	513260	19A157					4.303	4.304		4.305
109880	523680	19A161				0.638		0.62		
103370	515400	19A164						8.807	8.801	8.804
103540	514850	19A165					8.284	8.283	8.277	8.281
105680	515390	19A167					0.987	0.979	0.967	0.971
108160	523880	19A168					7.514	7.509	7.503	7.505
103710	519490	19A169					7.974	7.966	7.954	7.952
108000	521330	19A170					4.611	4.593	4.577	4.572
104600	514900	19A171					7.044	7.04	7.034	7.037
105950	517280	19A172						3.133	3.122	3.122
105530	516820	19A173						3.492	3.483	3.482
105460	516150	19A174						3.218	3.209	3.211
106740	514970	19A175						-0.036		-0.036
105910	518750	19A178						3.944	3.931	3.930
107480	514860	19A185						0.469		0.472
106120	515020	19A190						-0.058		-0.060
103490	515370	19A191							13.546	13.549
103110	514510	19A192						16.054	16.054	16.052
103110	514250	19A193						16.203	16.203	16.204
103750	514500	19A194						14.449	14.448	14.450
105110	515230	19A197						2.621		2.611
104280	523500	19A200							6.460	6.454
105060	512920	19A204						4.013		4.014
104900	522920	19A205							5.619	5.611
104800	522470	19A206							6.865	6.855
104780	520730	19A207							7.956	7.946

103150	515450	19A210							12.922	12.922
103180	515800	19A211							3.524	2.354
103280	516800	19A212							1.011	0.968
103450	517800	19A213							0.795	0.799
103520	518780	19A214							2.877	2.868
104270	519650	19A215							9.831	9.827
104190	520090	19A216							6.148	6.147
104200	523500	19A217							7.382	7.376
104620	523750	19A218							7.635	8.087
104850	522920	19A219							6.068	6.060
111760	513300	19B008		-1.157	-1.158	-1.163	-1.177	-1.179	-1.184	
112580	513680	19B009	0.648	0.648	0.651					
110480	514680	19B014	1.833	1.83	1.831	1.827	1.817	1.815	1.811	1.812
110880	515120	19B019	1.674	1.669	1.67	1.664	1.65	1.648	1.644	1.644
110840	515110	19B020						1.413	1.410	1.410
113520	515440	19B023			2.712		2.695	2.693	2.693	2.690
111770	516400	19B029		1.273	1.272	1.267	1.252	1.249	1.243	1.242
113650	515140	19B044	-3.742	-3.745	-3.745	-3.748	-3.764	-3.765	-3.768	-3.770
111530	519340	19B055	0.006	0.003	0.003	-0.002	-0.014	-0.018	-0.024	-0.024
111950	520470	19B068	2.016	2.012	2.01	2.008				
112580	513680	19B128	-1.015	-1.015	-1.011	-1.016	-1.029			
112580	513680	19B129	0.652	0.649	0.649	0.634	0.61			
113060	514520	19B133	5.451	5.444	5.445	5.443				
113160	514550	19B134			-1.049			-1.071	-1.075	-1.076
114160	514800	19B138		-2.888	-2.886	-2.888	-2.902	-2.903	-2.907	-2.906
115780	514230	19B140			-2.81		-2.822	-2.825	-2.829	-2.828
112140	516280	19B168	0.462	0.462	0.462	0.46	0.448	0.446	0.443	0.443
110120	517420	19B174	0.895	0.878	0.876	0.868	0.85	0.84	0.829	0.827
111140	517120	19B178						-0.615	-0.624	-0.625
111510	519360	19B194	0.418	0.414	0.415	0.411	0.399			
113460	515500	19B220	0.965	0.961	0.958	0.956	0.941	0.938	0.935	
110210	515400	19B226	1.187	1.182	1.183	1.177	1.167	1.165	1.160	1.162
110210	516390	19B230	0.388				0.356	0.35	0.341	0.340
110580	516650	19B231		0.968	0.966	0.959	0.945	0.938	0.929	0.927
111100	517080	19B234		0.618	0.614	0.606	0.588	0.578		
110200	523080	19B238	0.57	0.552	0.551	0.543	0.534	0.531	0.522	0.521
111270	521730	19B239	0.801	0.785	0.773		0.761	0.756	0.749	0.747
111750	521110	19B240	0.959	0.925	0.911	0.9	0.884	0.873	0.863	0.860
113040	514530	19B241	5.038	5.009	5.003	4.995	4.976	4.971		
113020	514560	19B253		0.963	0.963		0.945	0.942	0.940	0.938
110080	516140	19B275		1.005	1.001	0.992	0.977	0.97	0.960	0.957
111500	517320	19B276		0.854	0.849	0.841	0.823	0.816	0.808	0.804
111330	518670	19B277		-0.074	-0.075	-0.083	-0.098	-0.102	-0.112	-0.113
112860	515920	19B278		1.129	1.128	1.125	1.11	1.109	1.106	1.106
110480	517120	19B279		0.627	0.62	0.608	0.588	0.574	0.560	0.554
113460	515490	19B280		2.092	2.089	2.088	2.071	2.069	2.066	0.023
110580	522660	19B281		0.591	0.586	0.575	0.563	0.556	0.528	0.520
111960	520460	19B282		0.448	0.446	0.442				

110110	517970	19B283		-0.229	-0.235	-0.246	-0.268	-0.28	-0.295	-0.299
114460	512760	19B284		-1.785	-1.787	-1.792	-1.808	-1.815	-1.825	-1.828
114700	513730	19B285		-3.461	-3.461	-3.466	-3.484	-3.491		
112100	514120	19B323			-0.399	-0.406	-0.42	-0.425	-0.428	-0.427
110900	519740	19B324			0.743	0.737	0.722			
111180	524680	19B325			-0.657		-0.665			-0.667
112750	514000	19B332			0.932		0.914	0.907	0.907	0.906
111080	516500	19B344						1.826	1.821	
115070	514560	19B349					-2.711	-2.714	-2.720	-2.719
115070	514420	19B350					-2.225	-2.227	-2.232	-2.232
111610	515020	19B351				1.178	1.165	1.164	1.159	1.161
115040	514460	19B352				-1.872	-1.9	-1.908	-1.917	-1.919
111440	517850	19B353				1.194	1.168	1.154	1.138	1.131
112580	513680	19B354				0.646	0.633			
111750	520000	19B360					0.513	0.501	0.492	
113310	515070	19B363					-1.139	-1.141	-1.144	-1.144
112220	514450	19B383						0.772	0.764	0.766
111600	516650	19B396							1.358	1.359
105420	512320	19C072			4.496		4.481			4.485
106400	512260	19C073			0.395			0.384		0.382
108160	512170	19C243			1.926		1.917	1.917		1.914
105730	512100	19C271						1.474		1.474
106340	512170	19C284					0.709	0.708		0.707
105410	512360	19C297						3.553		3.552
111640	512470	19D084		-0.829	-0.83	-0.835	-0.848	-0.849	-0.856	-0.860
114260	512080	19D154		-3.002	-3.005	-3.011	-3.027	-3.036	-3.050	-3.056
115360	512440	19D268		-3.195	-3.195	-3.196		-3.215	-3.226	-3.229
110100	512000	19D307				0.626	0.617	0.615	0.611	0.614